SEARCH FOR EFFECTIVE SPIN INJECTION HETEROSTRUCTURES BASED ON HALF-METAL HEUSLER ALLOYS/GALLIUM ARSENIDE SEMICONDUCTORS: A THEORETICAL INVESTIGATION

by

CHOCKALINGAM SIVAKUMAR

WILLIAM H. BUTLER, COMMITTEE CHAIR
CHRIS PALMSTRØM
PAUL VOYLES
GREGORY THOMPSON
EUNSEOK LEE

A DISSERTATION

Submitted in partial fulfillment of the requirements
for the degree of Doctor of Philosophy
in the Interdisciplinary Studies: Materials Science Program
in the Graduate School of
The University of Alabama

TUSCALOOSA, ALABAMA

2016

Copyright Chockalingam Sivakumar 2016
ALL RIGHTS RESERVED

ABSTRACT

Efficient electrical spin injection from half-metal (HM) electrodes into semiconducting (SC) channel material is a desirable aspect in spintronics, but a challenging one. Half-metals based on the Heusler alloy family are promising candidates as spin sources due to their compatibility with compound SCs, and very high Curie temperatures. Numerous efforts were made in the past two decades to grow atomically abrupt interfaces between HM_Heusler and SC heterostructures. However, diffusion of magnetic impurities into the semiconductor, defects and disorder near the interface, and formation of reacted phases were great challenges. A number of theoretical efforts were undertaken to understand the role of such material defects in destroying the half-metallicity and also to propose promising half-metal/SC heterostructures based on first principles.

This dissertation summarizes the investigations undertaken to decode the complexity of, and to understand the various physical properties of, a number of real-world Heusler/SC heterostructure samples, based on the *ab initio* density functional theory (DFT) approach. In addition, it summarizes various results from the first principles-based search for promising half-metal/SC heterostructures.

First, I present results from DFT-based predictive models of actual Co_2MnSi (CMS)/-GaAs heterostructures grown in (001) texture. I investigate the physical, chemical, electronic, and magnetic properties to understand the complexity of these structures and to pinpoint the origin of interfacial effects, when present. Based on the investigations of such models, I discuss the utility of those actual samples in spintronic applications. Next, I summarise the results from an *ab initio* DFT-based survey of 6 half-Heusler half-metal/GaAs heterostructure models in (110) texture, since compound semiconductors such as GaAs have very long spin lifetime in (110) layering. I show 3 half-Heusler alloys (CoVAs, NiMnAs, and RhFeGe), that when interfaced with GaAs(110), fully preserve the

half-metallicity at the interface. Finally, I show the advantages of inserting half-Heusler SCs, particularly CoTiAs and CoTiSb, as spacers in between CMS/GaAs systems in (110) layering. Based on DFT calculations, I show that CoTiAs is a promising spacer that could enhance the perpendicular magnetic anisotropy in CMS, while preserving the important half-metallic character at the heterojunctions between CMS/CoTiAs/GaAs(110). This spacer could also serve to prevent in-diffusion of magnetic impurities into the channel material.

DEDICATION

To my dearest wife Padma and son Amudhan, and to the loving memory of Aachi.

LIST OF ABBREVIATIONS AND SYMBOLS

μ_{B}	Bohr magneton.
T_{C}	Curie Temperature.
ϵ_0	Permittivity of free space.
E_{F}	Fermi energy.
E_{MCA}	Magnetocrystalline anisotropy energy.
H_K	Anisotropy field.
K_{u}	Uniaxial magnetocrystalline anisotropy.
m	Magnetic moment.
M	Magnetization.
M_{s}	Saturation magnetization.
P	Spin Polarization.
$\rho(\mathbf{r})$	Electron density.
2-DEG	Two-dimensional electron gas.
CMS	Co_2MnSi.
DFT	Density Functional Theory.
DMS	Dilute Magnetic Semiconductor.
DOS	Density of States.
D–P	D'yakonov–Perel'.
EELS	Electron Energy Loss Spectroscopy.
FM	Ferromagnet.
GaAs	Gallium Arsenide.
GGA	Generalized Gradient Approximation.

GMR	Giant Magnetoresistance.
HF	Hartree–Fock.
HM	Half-Metallic.
InP	Indium Phosphide.
KS	Kohn–Sham.
LDA	Local Density Approximation.
LDOS	Local Density of States.
MBE	Molecular Beam Epitaxy.
MRAM	Magnetoresistive Random Access Memory.
MTJ	Magnetic Tunnel Junction.
NHM	Near Half Metallic.
PAW	Projector Augmented Wave.
PBE	Perdew–Burke–Ernzerhof.
PMA	Perpendicular Magnetic Anisotropy.
SC	Semiconductor.
SOI	Spin–Orbit Interaction.
SP	Slater–Pauling.
SPIN-FET	Spin Field Effect Transistor.
STEM	Scanning Transmission Electron Microscopy.
SV	Spin Valve.
TMR	Tunneling Magnetoresistance.
VASP	Vienna *Ab initio* Simulations Package.

ACKNOWLEDGMENTS

With a deep sense of gratitude, I wish to thank the many people who created the ladders of opportunity in my life. I am deeply indebted to my advisor and committee chair William H. Butler for being an intellectual and moral support, right from my early days as a student in his Magnetic materials class. From sharing the many research expertise to extending invaluable support in the darkest and dullest hours of my life, without him, I would not have come this far. I also wish to thank the other members of my committee, Professors Paul Voyles, Chris Palmstrøm, Gregory Thompson, Eunseok Lee, and Jeffrey Weimer for the expertise and the encouragement that they provided throughout my research career.

With a sense of sorrow, I wish to remember the support and guidance provided by the Late Oleg Mryasov. I indebted to Sergey Okatov for sharing his valuable time and teaching many research techniques, and for the valuable guidance. I wish to thank Kamaram Munira and Javad Ghasemi for the valuable inputs and support. I wish to thank Professor Paul Crowell for providing valuable inputs during various research discussions and for the guidance. I wish to thank Professors Gary Mankey, Patrick LeCLair, Tim Mewes, Richard Tipping, Allen Stern, and many other professors from the Department of Physics for the many enriching lectures, motivation, and guidance throughout the early part of my time at the University of Alabama. My sincere thanks to Nancy Pekera, Karen Lynn, Sergio Fabi, and other office staff in the Physics department for their tireless support.

I would like to thank Jamie Crawford, Carrie Martin, and Casey McDow for their assistance in administrative matters, and MINT Director Takao Suzuki for his guidance.

I also wish to thank Jason Foster for providing support in accessing MINT computational clusters. I wish sincerely thank David Young from ASC cluster for the timely assistance and support in using Alabama supercomputer. I wish to thank Materials

Science Program Director Mark Weaver and campus Director Gary Warren for their support. A hearty thanks to Marie Rahne and Sylvia Hill for the various assistance provided during C-SPIN annual meetings. I wish to thank C-SPIN director Jianping Wang for extending C-SPIN funding for my research and travel.

During my graduate career, I received funding from C-SPIN, one of the six SRC STARnet Centers, sponsored by MARCO and DARPA. I was supported by the Tricampus Materials Science PhD Program of the University of Alabama System (UAS). I was also supported by Graduate Teaching Assistantship from the Department of Physics.

CONTENTS

ABSTRACT ii

DEDICATION iv

LIST OF ABBREVIATIONS AND SYMBOLS v

ACKNOWLEDGMENTS vii

LIST OF TABLES xii

LIST OF FIGURES xiv

1 INTRODUCTION 1

1.1 Magnetoelectronics 2

1.1.1 Band structure of a ferromagnet 3

1.1.2 The GMR effect 5

1.1.3 Spin valve and the two-resistor model 6

1.2 Semiconductor Spintronics 7

1.2.1 Spin–Orbit interaction 8

1.2.2 Spin relaxation times 8

1.2.3 Spin field effect transistors 9

1.2.4 Spin injection efficiency 11

1.3 Half-metal Heuslers 12

1.3.1 Slater–Pauling behavior 14

1.4 Importance of GaAs 18
1.4.1 D'yakonov–Perel' mechanism 19

2 METHODS 21
2.1 Density functional theory 21
2.1.1 Electron density 22
2.1.2 Exchange–Correlation energy 22
2.2 Computational Details 23

3 MODELING Co_2MnSi/GaAs INTERFACES IN (001) LAYERING 25
3.1 Introduction 25
3.2 Methods 28
3.2.1 Co_2MnSi/GaAs(001) with 0.5ML-flux 32
3.2.2 Co_2MnSi/GaAs(001) with 1ML-flux 37
3.3 Results and Discussion 39
3.3.1 Co_2MnSi/GaAs(001) with 0.5ML-flux 39
3.3.2 Co_2MnSi/GaAs(001) with 1ML-flux 46
3.4 Conclusion 57

4 HALF-METAL HALF-HEUSLER/GaAs(110) HETEROSTRUCTURES FOR EFFICIENT SPIN INJECTION 58
4.1 Introduction 58
4.2 Methods 59
4.2.1 Half-metal half-Heusler characteristics 59
4.2.2 Interface modeling 61
4.2.3 Computational details 62
4.3 Results 63

4.4 Conclusions 67

5 SEMICONDUCTING HALF-HEUSLER ALLOYS AS SPACERS BETWEEN Co_2MnSi/GaAs(110) 69

5.1 Introduction 69

5.2 Methods 70

5.3 Results 72

5.4 Conclusions 77

6 SUMMARY AND CONCLUSIONS 79

REFERENCES 81

A DFT models for 0.5ML CMS/GaAs(001) 89

A.1 Case91 DFT model 89

A.2 Case97 DFT model 90

LIST OF TABLES

1.1 Properties of selected Co-based full-Heusler alloys 16

3.1 Comparison of the projected-planar atomic distances 41
3.2 The atomic magnetic moments at the interface for the best-fit DFT model 44
3.3 Comparison of properties between identical DFT model structures 46
3.4 Calculated $P_{(s,p)}$ and $m(\mu_B)$ for Case1 DFT model 51
3.5 Calculated $P_{(s,p)}$ and $m(\mu_B)$ for Case2 DFT model 54
3.6 E_F and P for the DFT models for 1ML CMS/GaAs(001) 56

4.1 Selected properties of the 6 half-Heusler alloys used in this study 61
4.2 Calculated parameters of the 6 half-Heusler/GaAs(110) interfaces 65
4.3 Magnetic moments of atoms at the interface for half-Heusler/GaAs(110) . 67

5.1 Selected properties of CoTiAs and CoTiSb 70
5.2 Magnetic moment in the interface in CMS/CoTiAs/GaAs(110) system . 74
5.3 Bandgap properties of CMS/CoTiAs(n)/GaAs(110) for $n = 2, 3, 4$ 76
5.4 Geometric and magnetic properties of CMS/CoTiAs(n)/GaAs(110) . . . 77

LIST OF FIGURES

1.1 A simple model for the band structure of a ferromagnet. 4

1.2 Schematic of magnetization in a spin valve with FM/NM/FM junction. . 6

1.3 Schematic representation of a Datta–Das SPIN-FET. 10

1.4 Ball-and-stick representation of a full-Heusler alloy ($L2_1$ crystal structure). 13

1.5 Schematic representation of DOS in various elements. 13

1.6 SP behavior in some full-Heusler alloys. 16

1.7 Calculated DOS for bulk Co_2MnSi. 17

1.8 GaAs zinc-blende unit cell and surface. 18

1.9 The direction of the Dresselhaus and Rashba fields in a quantum wire. . 20

3.1 The β-structure model of GaAs(001)-c(4×4) surface reconstruction. . . 29

3.2 Non-local spin valve measurement of Co_2MnSi/GaAs samples. 30

3.3 Cubic unit cells of (a) Co_2MnSi and (b) GaAs in (001) direction. 31

3.4 Schematic top view of high symmetry patterns in CMS/GaAs(001). . . . 31

3.5 Periodic supercell of CMS/GaAs(001) with ideal abrupt termination. . . 32

3.6 Z-contrast STEM micrographs of the CMS/GaAs interface. 33

3.7 Schematic layer-by-layer top view of the complex interface. 34

3.8 Interlayer separation of the complex interface. 35

3.9 Periodic supercell structures to model 0.5ML-flux CMS/GaAs(001). . . . 36

3.10 STEM and EELS of 1ML CMS/GaAs(001) with MnSi-initial flux. 38

3.11 The interface structure in the DFT model for 0.5ML CMS/GaAs(001). . 40

3.12 Comparison of DFT-simulated STEM with actual STEM. 42

3.13 DOS of the best-fit DFT model for 0.5ML CMS/GaAs(001). 42

3.14 Atom-projected DOS of the interfacial atoms for the best-fit DFT model. 44

3.15 Comparison of atom-projected DOS of Int3 Mn with bulk-Mn. 45

3.16 The DFT supercell schematic of 1ML CMS/GaAs(001). 47
3.17 Ball-and-stick representation of the DFT-relaxed interface structure. . . . 49
3.18 DOS for 1ML-CMS/GaAs(001) with MnSi-initiated flux. 50
3.19 LDOS at the interface for Case1 DFT model for 1ML-CMS/GaAs(001). . 50
3.20 Ball-and-stick representation of the DFT-relaxed structure for Case2. . . 53
3.21 The total DOS of the periodic supercell structure for Case2. 54
3.22 LDOS at the interface for Case2. 55
3.23 The total DOS of the DFT-model for Case3. 56

4.1 Lattice mismatch plot for the 6 half-Heusler alloys chosen in this study. . 60
4.2 The cubic unit cell of the half-Heusler ABC and GaAs. 62
4.3 Energetically stable ideal interface patterns between half-Heusler/GaAs(110). 63
4.4 LDOS at half-Heusler interface. 66

5.1 Cross-sectional view of a (110) supercell. 71
5.2 Representation of CMS/CoTiAs/GaAs(110) heterojunction. 72
5.3 DOS of CMS/CoTiAs/GaAs(110) model with 2 layers of CoTiAs. 73
5.4 LDOS at the interface for CMS/CoTiAs/GaAs(110) model. 74
5.5 Comparison of the bandgap in CMS/CoTiAs(n)/GaAs(110) for $n = 2, 3, 4$. 75

A.1 Ball-and-stick representation of the interface structure in Case91. 90
A.2 DOS of Case91 DFT model with MnSi-initial flux. 91
A.3 DOS of Case97 DFT model with MnSi-initial flux. 92

CHAPTER 1

INTRODUCTION

Moore's Law [1], which states that the number of transistors per square inch on integrated circuits will double every 18 months, had been an excellent predictor of integrated circuit density for the past four decades. However, the scale of the electronic devices has now reached a fundamental size limit where quantum effects begin to interfere with the operation of the devices [2]. While conventional electronics exploits the charge associated with electrons to process and/or transmit information, an intrinsic quantum effect, namely the spin of the electron, is not utilized. Spintronics is a branch of science, which exploits the spin degree of freedom in addition to, or in place of, the charge of the electron to store, access, process, and/or transmit information. Using the spin degree of freedom of the electron adds promising functionalities to that of existing semiconductor electronics, namely, non-volatility of information in the absence of power, higher data processing speed, lower power consumption, and higher integration densities beyond the current fundamental size limit [3, 4].

From pioneering works of Mott [5, 6], which laid the foundation for spin-polarized transport, to that of Jullière [7], which proved that the tunneling current may remain spin-polarized ouside the ferromagnetic regime, the science of spintronics is built upon the results obtained in areas of physics as diversified as magnetism, semiconductor physics, optics, superconductivity, etc. [8]. However the potential for the use of the spin of the electron in the context of electronics was first established in 1988 with the discovery of Giant Magnetoresistance (GMR) [9, 10], wherein a large change in electrical resistance was observed in ultrathin multilayers of magnetic materials on the application of a magnetic field. Soon after, in 1990, a Spin Field Effect Transisitor (SPIN-FET) was proposed, for the first time, as an active spin-based semiconductor device in which the spin degree of

freedom of the charge carrier is used to process digital information [11]. Other notable discoveries that demonstrated the utility of semiconductors as both source and carrier of information are that of Ohno and coworkers in 1996 [12] of ferromagnetic semiconductors and that of Awschalom and Kikkawa in 1999 [13] of spin coherence reaching nanosecond time scales in II–IV and III–V semiconducting carriers.

The study of spintronics involves the investigation of (i) the generation of spin polarization, (ii) spin transport, and (iii) spin dynamics and spin relaxation in solid state systems [14]. Efforts are taken in Section 1.1, to explain in simple terms, the generation of spin polarization, and spin transport. In Section 1.2, a basic explication of spin dynamics and spin relaxation will be presented before a generic spintronic scheme using a SPIN-FET is illustrated.

1.1 Magnetoelectronics

Giant Magnetoresistnace (GMR), along with Tunneling Magnetoresistance (TMR) and Magnetoresistive Random Access Memory (MRAM), is based on magneto-resistive effects and the technology is traditionally called magnetoelectronics, with principal application in sensing and storing information [4]. Successful applications of magnetoelectronics include magnetic field sensors, which are widely used as read heads in hard disk drives and the development of MRAM, which combines non-volatility with faster read/write speeds and unlimited endurance [15].

The generation of non-equilibrium spin population and the transport of spin-polarized current are essential in the functioning of any magnetoelectronic device. Conventional methods of generating spin polarization are optical and electrical; in the optical method, the angular momentum of circularly polarized photons is transfered to electrons whereas in the electrical method, a magnetic electrode (ferromagnet) is connected to a sample so that current from the electrode can inject spin polarized electrons into the sample, causing a non-equilibrium spin population. For practical device applications, electrical spin injection is preferred. A simple band structure model of a ferromagnet is given

below followed by an explanation of spin transport in multilayered structures such as Spin Valves (SV) and GMR heterostructures.

1.1.1 Band structure of a ferromagnet

An electron is a tiny subatomic particle with mass, m_e, and charge, -e. For the sake of understanding, we can consider the intrinsic magnetic moment of the electron as arising from the spin of the electron about an axis, with the caveat that this classical picture is inaccurate and does not explain the measured magnitude of the magnetic moment.[1] The magnetic moment is usually expressed as a multiple of the Bohr magneton, μ_{B},

$$\mu_{\mathrm{B}} = \frac{e\hbar}{2m_e} = 9.274 \times 10^{-24}\,\mathrm{J/T} = 5.788 \times 10^{-5}\,\mathrm{eV/T}$$

In ferromagnetic metals, in the presence of an external magnetic field, the spin magnetic moment of the electron align either parallel or anti-parallel to the external field. The convention is to label the electron spin as 'majority spin' or 'up spin' if its moment aligns parallel to the external field, and as 'minority spin' or 'down spin' if its moment aligns anti-parallel to the external field.

A simple model for the band structure of a ferromagnet is shown in Fig. 1.1 [17]. In this model, the band structure of a ferromagnet is composed of two sets of bands; a majority spin subband and a minority spin subband. As depicted in Fig. 1.1, the conduction band minimum for the minority spins is displaced from that of the majority spins by an amount equal to δE_{ex}, the exchange splitting energy. In this model, the $E-k$ relationship for the majority spins is given by

$$E_{\uparrow} = \frac{\hbar^2}{2m_0}k^2,$$

[1] The magnetic moment, μ_s associated with the spin of an electron is given by $\mu_s = \gamma \cdot \mathbf{S}$, where γ is the gyromagnetic ratio and $\mathbf{S}$ is the spin angular momentum. For an electron with charge e and mass m_e, the gyromagnetic ratio is $\gamma = \frac{-e}{m_e}$, a value almost twice that of the classical value, an explanation for which is given in relativistic quantum theory by the Dirac equation [16].

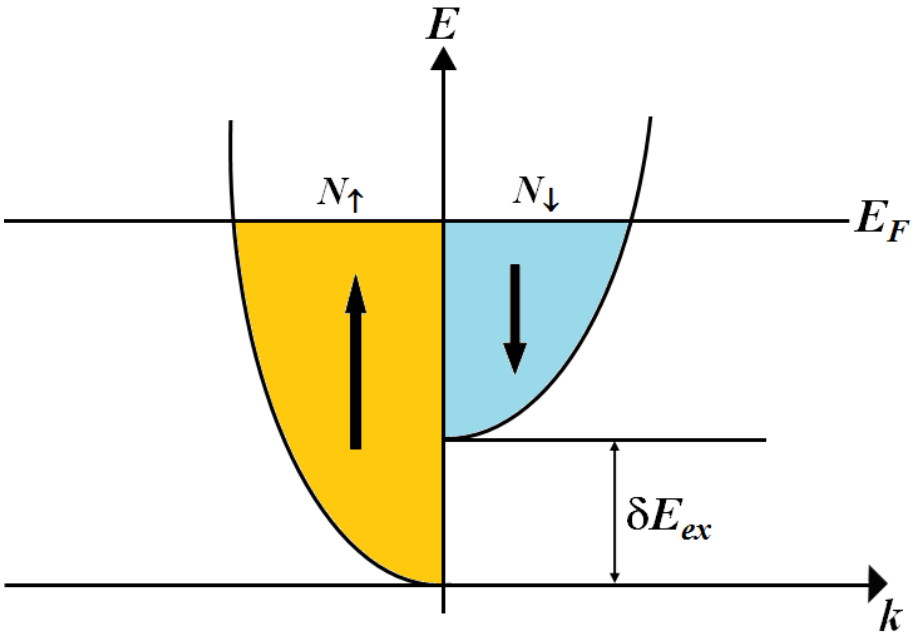

Figure 1.1: A simple model for the band structure of a ferromagnet is shown. The minimum of the conduction band for the minority spin is shifted upward from that of the majority spin by an amount δE_{ex}, the exchange splitting energy. The densities of electronic states at E_F for the majority and minority spins are denoted by $N_\uparrow$ and $N_\downarrow$, respectively.

and for the minority spins, it is given by

$$E_\downarrow = \frac{\hbar^2}{2m_0}k^2 + \delta E_{ex}.$$

Then at the Fermi energy, the Fermi wavevectors for the majority and minority electrons are different. As a result, the density of electronic states (DOS) at the Fermi level, E_F, for the majority spin subband ($N_\uparrow$) is different from that of the minority spin subband ($N_\downarrow$). The net spin polarization is given by

$$P = \frac{N_\uparrow - N_\downarrow}{N_\uparrow + N_\downarrow}. \tag{1.1}$$

The model for the band structure of the ferromagnet was motivated by the Mott two-current model [5] in which the direction of electron spin is preserved in the scattering process at temperatures well below the Curie temperature, T_C. Thus, the majority and minority spin currents $J_{FM}^{\uparrow}$ and $J_{FM}^{\downarrow}$ can be considered as two independent components

of the total current. Hence it is straightforward to explain spin transport in ferromagnets using the above band structure model; the motion of the conduction electron depends on its spin orientation with respect to the magnetization of the ferromagnet. Since the DOS at the Fermi level significantly differs for the two subbands, the conductivity of a ferromagnetic metal becomes spin dependent, causing a highly spin-polarized current.

If in our simple model, the exchange splitting energy is larger than the difference in energy measured from the conduction band minimum of the majority spin subband to the Fermi energy, the bottom of the minority spin subband will be above E_F. In such metals the minority band is completely unoccupied, making the spin polarization of the metal to be 100%. Such a material would be called a ferromagnetic half-metal [18]. We will discuss half metals in detail later in this chapter.

1.1.2 The GMR effect

The discovery of GMR, independently by Albert Fert [9] and Peter Grünberg [10], in 1988, was the first successful demonstration of the practical viability of spintronics in technology. Giant magnetoresistance is defined as a significant change in electrical resistance due to a change in the relative orientation of the magnetization of different regions of a metallic magnetic heterostructure. One type of GMR device is a multilayered thin-film structure comprised of alternate layers of ferromagnetic (FM) and non-magnetic (NM) metals, where the relative orientation of the magnetization of successive FM layers can be modulated to stay parallel or anti-parallel by adjusting the thickness of the NM spacer layer. This effect is achieved due to the interlayer exchange coupling which is mediated by the itinerant electrons in the metallic spacer layer. In this type of GMR device, the NM spacer layer is a few nanometer-thick, so as to create an anti-parallel orientation of magnetization of successive FM layers. Application of an external magnetic field can force the magnetizations to align parallel causing a significant reduction in resistance.

1.1.3 Spin valve and the two-resistor model

A basic unit of a GMR heterostructure is a spin valve, a trilayered structure consisting of a paramagnetic layer (NM) sandwiched between two FM layers. A simplified explanation for the resistance change in a GMR device can be given using the spin valve and the two current model of Mott as shown in Fig. 1.2. Earlier we saw that an electron whose

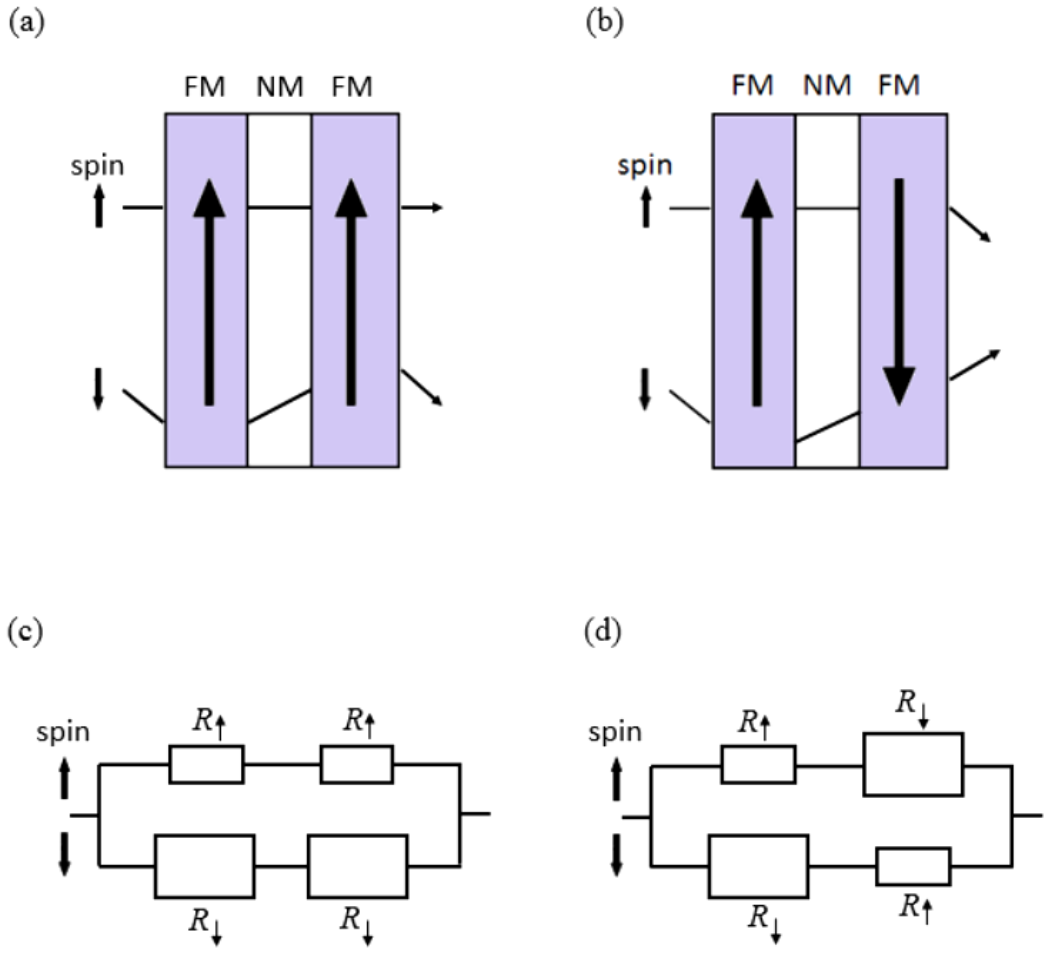

Figure 1.2: A spin valve with a FM/NM/FM junction when (a) the magnetization of the FM layers (indicated by large vertical arrows inside the FM layers) are either parallel or (b) anti-parallel. Small vertical arrows represent the spin of the conduction electrons through the spin valve. The horizontal arrows represent the motion of the conduction electrons; they are straight when the electrons experience minimal resistance, and scatter when they experience greater resistance. The simple two-resistor network model for the spin valve when (c) the FM layer magnetizations are parallel or (d) anti-parallel (adapted from Ref. [4]).

spin is parallel to the magnetization of a ferromagnet (majority spin) may experience much lower resistance than a minority spin electron. In Fig. 1.2(a), the magnetization

of both the FM regions are parallel to one another. The motion of an electron, with majority spin, through the spin valve is unhindered due to minimal resistance as depicted by the straight arrow.

However, an electron with minority spin experiences greater resistance at both the FM layers, as depicted by a zigzag arrow in Fig. 1.2(a). Figure 1.2(c) shows the corresponding two-resistor network model of the spin valve with the magnetic configuration as depicted in Fig. 1.2(a). For a spin valve system with the two FM layers having anti-parallel magnetization, the motion of the electron and the corresponding two-resistor network model are shown in Fig. 1.2(b) and (d), respectively. From the resistor network models of the spin valve for the two magnetic configurations, it is easy to show that the resistance for the anti-parallel configuration of the spin valve, $R_{\uparrow\downarrow}$, is higher than the resistance for the parallel configuration of the spin valve, $R_{\uparrow\uparrow}$. This simplified picture is useful for pedagogical reasons. Accurate calculation of the resistance of a multilayered GMR device is usually difficult and complicated by a number of transport effects. In GMR multilayer devices, the resistance may drop to less than one half its original value in a weak magnetic field,[2] causing giant magnetoresistance, given by

$$GMR = \frac{R_{\uparrow\downarrow} - R_{\uparrow\uparrow}}{R_{\uparrow\uparrow}},$$

where $R_{\uparrow\downarrow}$ is the resistance when successive FM layers have anti-ferromagnetic ordering (applied magnetic field = 0) and $R_{\uparrow\uparrow}$ is the resistance when successive FM layers have ferromagnetic ordering (applied magnetic field > 0).

1.2 Semiconductor Spintronics

Semiconductor spintronics differs from magnetoelectronics primarily in the aspect that it is the study of active spin-based devices capable of amplifying signals. A secondary difference is that magnetoelectronics usually covers paramagnetic and ferromagnetic metals

[2]The resistance change is device-dependent. Fert et. al. measured a factor of 2 reduction in resistance in Fe/Cr magnetic superlattices [9]. Often the resitance change is less.

and insulators, which utilize magnetoresistive effects, whereas in spintronics, semiconductors have the central role in the transport and modulation of the spin current.

1.2.1 Spin–Orbit interaction

An electron orbiting a nucleus experiences a magnetic field in its rest frame.[3] The spin magnetic moment, $\vec{\mu}_e$, arising from the spin of the electron interacts with the magnetic field, $\vec{B}$, arising from the orbital motion of the electron giving rise to an energy given by $E_{so} = -\vec{\mu}_e \cdot \vec{B}$. This interaction is known as the 'Spin–Orbit Interaction (SOI)'. However, in a solid, a quasi-free electron in the conduction band does not experience an electric field due to the strong nuclear attraction as in an atom, because the strong nuclear attraction of the nucleus is largely screened. But an electric field may be applied externally or may arise due to asymmetries in crystal. For example, a conduction band discontinuity in heterostructures can create an internal potential gradient, thereby creating a strong electric field. This field will induce a spin–orbit interaction. This is known as the Rashba interaction or interaction due to structural inversion asymmetry. In crystals, electric field may also arise internally due to crystallographic inversion asymmetry. The associated SOI due to this field is called as the Dresselhaus interaction. The Rashba interaction plays a central role in spintronics as it can be tuned by an external electric field.

1.2.2 Spin relaxation times

The spin current in a generic spintronic device refers to the net spin polarization of an ensemble of charge carriers. For efficient functioning of the device, random depolarization caused by spin relaxation should be minimized. Spin relaxation is the process by which a non-equilibrium spin population returns to equilibrium. There are two spin relaxation times; (i) the longitudinal relaxation time, T_1, also known as the spin relaxation time, and (ii) the transverse relaxation time, T_2, also known as the spin dephasing time. Time T_1 is a measure of the time required for spins in a higher-energy eigenstate to decay back

[3]Precisely, an electron orbiting a nucleus experiences an electric field in the rest frame of the nucleus. In the rest-frame of the electron it will experience a magnetic field as well as an electric field. The calculated interaction of the electron's spin moment with its orbital angular momentum was a factor of 2 larger than the observed fine structure effects. In 1926, L.H. Thomas explained that the rest-frame of an electron is not an intertial frame and calculated the Thomas precession, which introduces a factor of 1/2 to the spin–orbit interaction [19].

to the ground state. T_1 is associated with energy dissipation. Time T_2 is the time taken for transverse electron spins, precessing in phase about the longitudinal field, to lose their phase coherence due to spatial and temporal fluctuations of the precessing frequencies. In semiconductors, spin relaxation of conduction band electrons takes place by four major mechanisms, namely, (i) D'yakonov–Perel' mechanism, (ii) Elliot–Yafet mechanism, (iii) Bir–Aronov–Pikus mechanism, and (iv) hyperfine interactions with nuclear spins [20]. The D'yakonov–Perel' mechanism is important and we will discuss it briefly in Section 1.4.1.

1.2.3 Spin field effect transistors

In 1990, in what could be called a cornerstone event for spintronics, Datta and Das propsed a Spin Field Effect Transistor (SPIN-FET) [11], which is one of the first active devices to utilize the spin of the electron to process information. The basic idea is that in such a transistor, an applied electric field can modulate the spin current in a channel by controlling the spin–orbit coupling in the channel. Schematic of a SPIN-FET is shown in Fig. 1.3. It is like any three-terminal transistor device, except for two major differences; (i) the source and the drain are ferromagnetic metals capable of injecting a highly spin-polarized current and (ii) the channel, connecting the two ferromagnetic electrodes laterally, is a two-dimensional electron gas (2-DEG) formed at the heterojunction between two semiconductors. The 2-DEG would provide a very high mobility channel with very large spin diffusion lengths. Also, the channel is free of electric fields in the absence of a gate voltage, thus the Rashba interaction is absent. There is also no Dresselhaus interaction. Hence, the channel is free of spin-flip scattering and spin relaxation. For efficient functioning of the SPIN-FET, it is expected that the FM source injects only majority spins (100% spin-polarized current), the FM drain transmits only majority spins, and there is no spin-flip scattering at the interface between the source and the channel. Figure 1.3 shows the net magnetization of both the source and the drain are aligned parallel to each other (in +x direction). When a potential difference is applied between the two electrodes, 100% spin-polarized current flows in the channel in +x direction. In the absence of a gate voltage, there is no spin relaxation in the channel

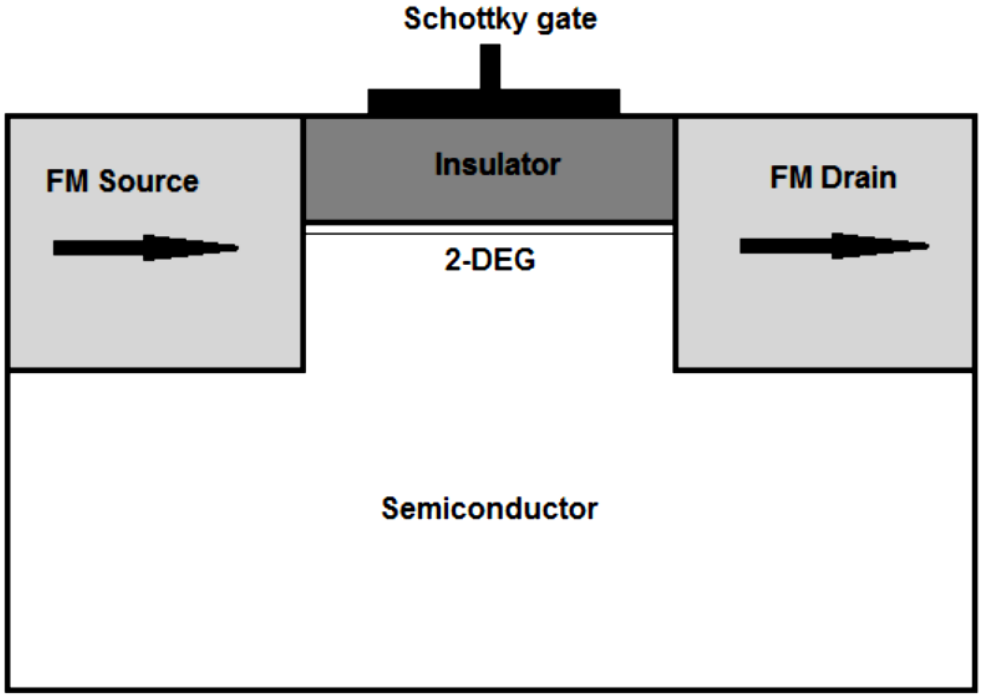

Figure 1.3: Schematic representation of a Datta–Das SPIN-FET. The net magnetization of the FM source and the FM drain are parallel to each other and point in the +x direction. The two-dimensional electron gas (2-DEG) that is formed at the heterojunction between two semiconductors acts as the channel, and is laterally connected to the FM electrodes.

thus the drain transmits the current with 100% efficiency. When the gate voltage is turned on, an electric field perpendicular to the direction of the current flow is generated, which causes Rashba spin–orbit interaction in the channel. Thus the gate voltage causes current modulation via spin precession.

1.2.4 Spin injection efficiency

Earlier experiments to inject spin-polarized current from FM metals to semiconductors (SC) proved rather unsuccessful [21, 22, 23]. Schmidt et. al. [24] argued that, in the diffusive transport regime, to get measurable spin accumulation in the semiconductor, the ratio of conductivity of the ferromagnet to that of the semiconductor has to be less than or equal to 1 ($\sigma_{\mathrm{FM}}/\sigma_{\mathrm{SC}} \leq 1$). When this ratio is much greater than 1, it is referred to as the 'conductivity mismatch problem' (or the resistivity mismatch problem), since the FM source itself behaves as an efficient sink, due to much lower resistance compared to the semiconductor, for any spin accumulation at the interface. The resistivity mismatch problem can be overcome by using suitable ferromagnetic semiconductors or half-metal ferromagnets (100% spin polarization). Rashba proposed [25] that the resistivity mismatch problem could be circumvented by sandwiching an appropriate tunnel barrier between the ferromagnet and the semiconductor.

Another important argument pertaining to spin injection efficiency arises from the conductance on/off ratio of modern transistors, whose value stands at 10^5. A conductance on/off ratio for SPIN-FETs depends on the spin injection efficiency at the source, ζ_S, and the spin detection efficiency at the drain, ζ_D. For SPIN-FETs to achieve a conductance ratio of 10^5, required of modern transistors, the efficiencies have to be $\zeta_S = \zeta_D = 99.9995\%$ [26]. To achieve 100% efficiency, it is imperative to use ferromagnets with 100% spin polarization such as half metals as both the source and the drain.

Spin injection into the semiconducting channel has been measured with a wide variety of ferromagnetic sources. The spin injection efficiencies as reported in various investigations are discussed below. While measurements based on Fe/SC yielded spin injection efficiencies of 40% [23, 27, 28], studies based on Dilute Magnetic Semiconductor (DMS) yielded slightly better efficiencies [29]. By insertion of a thin oxide barrier like MgO at

the FM/SC interface, spin injection efficiencies up to 70% were achieved [30]. While impedance mismatch between Fe and semiconductor is one of the main reasons for the decrease in spin injection efficiency, replacing Fe with a DMS helped to overcome this limitation. However, this approach is limited by the low Curie temperature (<150 °C) in typical ferromagnetic semiconductors like $Ga_{1-x}Mn_xAs$ [29]. Insertion of tunnel barriers like MgO overcame both limitations, but this approach too had shortcomings, namely, driving up the power consumption in device due to inefficient electrical transport across oxide tunnel barrier and increasing the complications of device fabrication.

There are very few studies that have measured spin polarization of currents injected from Heuslers into semiconductors [31, 32, 33, 34]. The highest spin injection measured so far with efficiency slightly above 50% is with Co_2FeSi as the source [32]. Atomic disorder and diffusion of magnetic impurities are considered to be the dominant features reducing the spin-injection efficiency in half-metal Heusler/SC interface.

1.3 Half-metal Heuslers

Different classes of materials are found to possess half-metallicity including oxides like Fe_3O_4 and CrO_2 [35, 36], transition metal pnictides like MnAs, MnSb, CrAs, and CrSb [37, 38, 39, 40], and certain half- and full-Heusler alloys [41, 42]. However the focus of this thesis is half metal Heuslers.

After de Groot and his collborators [41] predicted, using first-principle electronic structure calculations, that NiMnSb is half-metallic, a number of half- and full-Heuslers were predicted to be half metals. Since then half-metal Heuslers have attracted great interest, particularly in the field of spintronics, as promising candidates for a spin injection source. Heuslers are intermetallic alloys with two different crystal structures, namely $L2_1$ structure (full-Heuslers) and $C1_b$ structure (half-Heuslers) [43, 44]. The $L2_1$ structure comprises 4 interpenetrating fcc sublattices, while the $C1_b$ structure comprises 3 interpenetrating fcc sublattices. Figure 1.4 shows a ball-and-stick representation of the $L2_1$ crystal structure with chemical formula X_2YZ. The X ion occupies two of the four fcc

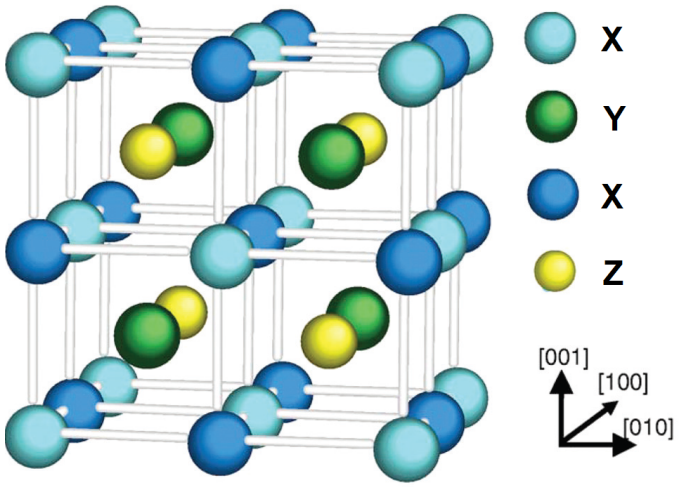

Figure 1.4: Ball-and-stick representation of a full-Heusler alloy ($L2_1$ crystal structure). Half Heuslers with $C1_b$ crystal structure form when there is a void in one of the X-ion sublattices.

sublattices. A $C1_b$ structure with chemical formula XYZ is formed when there is a void in one of the X sublattices in Fig. 1.4.

Typically, in half-metal Heuslers, the X- and Y-sites are occupied by transition metals, and the Z-site by a main group element. In half-metals, the Fermi level is populated for one spin band (majority), while it lies within a bandgap for the other spin band (minority), thereby having 100% spin-polarization. Figure 1.5 depicts a schematic sketch of Density of

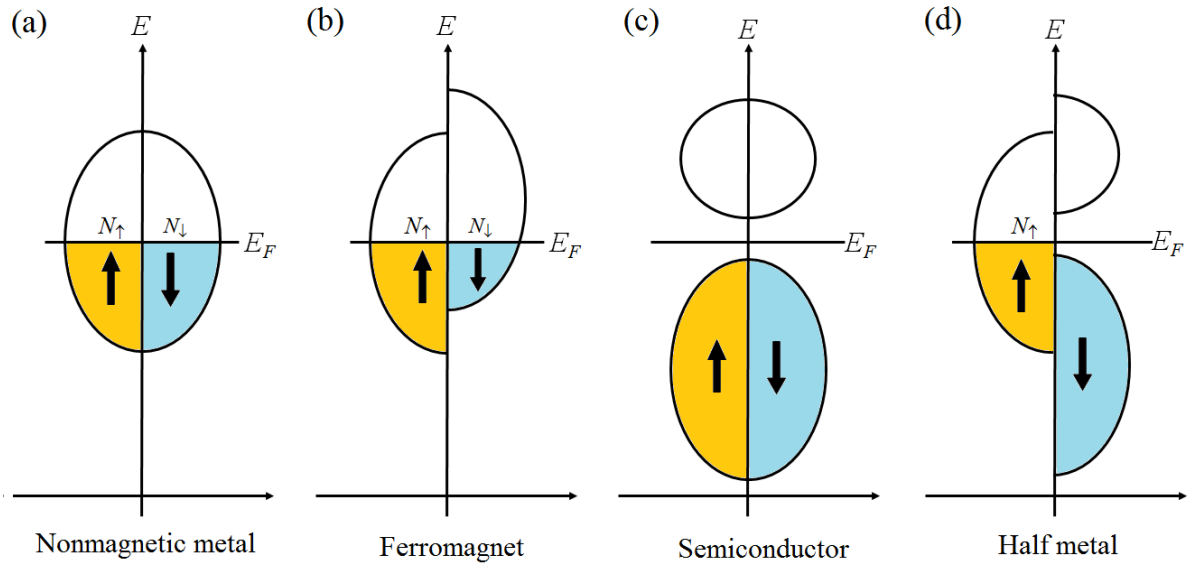

Figure 1.5: Schematic representation of the density of states for majority- and minority-spin subbands in (a) a nonmagnetic metal, (b) a ferromagnet, (c) a semiconductor, and (d) a half metal. For each material, the densities of electronic states at the Fermi energy, if present, are denoted as $N_\uparrow$ for majority- and $N_\downarrow$ for minority spins.

States (DOS) for majority- (up spin) and minority-spin (down spin) subbands in various types of materials. E_{F} denotes the position of the Fermi level. $N_{\uparrow}$ and $N_{\downarrow}$ are the densities of electronic states for up- and down-spins at the Fermi level. Metals have an equal population of spin-up and spin-down electrons at equilibrium as represented by the DOS. Thus, by invoking Eq. (1.1), $P = 0$, for a non-magnetic metal. As we discussed ealrier, ferromagnets have an imbalance in their spin-up and spin-down electron population, thereby having a finite spin polarization ($0 < P < 1$). For semiconductors, E_{F} is situated in the bandgap for both the spin subbands. In Fig. 1.5(d), we can see that for half metals, one of the spin bands (majority) behaves as a metal (with finite $N_{\uparrow}$), whereas the other band (minority) behaves like a semiconductor ($N_{\downarrow} = 0$). Hence the name half metal. Thus the net spin polarization is 100% ($P = 1$).

The origin of the bandgap in one of the spin bands in half-metal Heusler alloys is slightly different for half- and full-Heuslers. In half-Heuslers, the gap originates from the strong hybridization between the *d*-states of the higher valent and lower valent transition metal ions [45]. In full-Heuslers of the form X_2YZ, the band gap for one spin channel arises due to hybridization between the *d*-states of the two X atoms and the subsequent interaction of these hybrids with the *d*-states of the Y atom [46]. Thus the origin of gap in full-Heuslers is subtle. In both half- and full-Heuslers, the Z atom (*sp*-element) contributes only to the structural stability of the alloys.

1.3.1 Slater–Pauling behavior

In half-metal half-Heusler alloys, with chemical formula XYZ, exactly 9 bands are fully occupied in the minority band,[4] due to the gap at the Fermi level. Thus the minority band accommodates 9 electrons per unit cell. If Z_t represents the total number of valence electrons, and M_t represents the total moment per formula unit (measured in μ_{B}), then Z_t is given by the sum of the number of majority- ($n_{\uparrow}$) and minority ($n_{\downarrow}$) electrons, while M_t is given by the difference

$$Z_t = n_{\uparrow} + n_{\downarrow}, \qquad M_t = n_{\uparrow} - n_{\downarrow}$$

[4]The gap is usually (but not always) in the minority channel; for a few half-metallic half-Heuslers the gap is in the majority channel. For pedagocical purpose, I assume the gap to be in the minority channel.

Thus,

$$M_t = Z_t - 2n_\downarrow$$

Since in $C1_b$ Heusler alloys, the minority band accommodates 9 electrons, we have $n_\downarrow = 9$. Thus we get the simple "rule of 18" for half-metallicity

$$M_t = Z_t - 18. \tag{1.2}$$

This is an analogous relationship to the famous Slater–Pauling (SP) behavior of the binary transition metal alloys [47]. In many half-metal half-Heusler alloys, the minority population is fixed to 9 electrons, so the screening is achieved by filling the majority band.

In half-metal full-Heusler alloys, in general, the minority band is occupied by 12 electrons. Thus the minority band contains 12 electrons per unit cell. Thus, scaling the above equation for full-Heuslers, we get the "rule of 24" and the total moment is given as

$$M_t = Z_t - 24. \tag{1.3}$$

Figure 1.6 shows SP behavior in some of the full-Heuslers studied by Galanakis et. al. [45]. It shows the calculated total spin magnetic moment per unit cell (M_t, in units of μ_B) as a function of total number of valence electrons per unit cell (Z_t). The dashed line in the plot represents the SP behavior. From the figure, we see that a number of full-Heusler alloys, denoted by solid dots, obey the SP rule. We see that in these alloys, the total magnetic moment increases by 1 μ_B as the number of valence electrons increases by one.

As can be seen from the above SP curve, a number of Co-based full Heuslers of composition Co_2YZ exhibit the highest moment per unit cell. Many of these full Heuslers have very high Curie temperatures and are closely lattice matched with binary semiconductors.

Table 1.1 shows the Curie temperatures, magnetic moments, and lattice mismatch with GaAs of some of the Co-based full-Heusler alloys that are predicted to be half metallic. Although Co_2FeSi is not predicted to be a half metal, it is one of the FM sources which has shown a very high efficiency in injecting spin-polarized current into

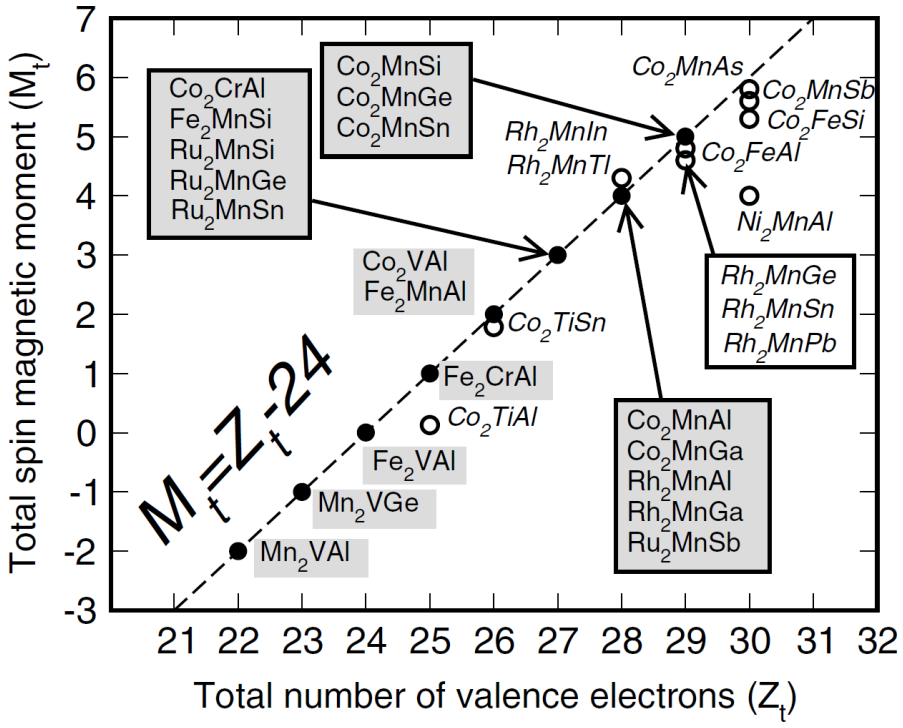

Figure 1.6: Calculated total spin moment per unit cell (M_t, in units of μ_B) as a function of the total number of valence electrons per unit cell (Z_t) for some of the full-Heusler alloys. The dashed line represents SP behavior. Compounds deviating from the SP curve, thus losing half metallicity, are denoted by open circles (adapted from Ref. [45]).

Table 1.1: Some Co-based full-Heuslers with their Curie temperatures, magnetic moments, and lattice mismatch with GaAs

Heusler alloy	Curie Temperature (K)	Magnetic moment[a] (μ_B/f.u.)	Lattice mismatch with GaAs (%)
Co_2FeSi[b]	1100[c]	5.46	0.08
Co_2FeAl[b]	1000[d]	4.98	1.3
Co_2MnSi	985[d]	5.0	0.3
Co_2MnGe	905[e]	5.0	1.6
Co_2MnAl	726[f]	4.0	1.8

[a]Magnetic moments and lattice parameters are theoretical values from first principle DFT calculations (from Heusler Database [44]).
[b]Not half metals. But spin injection from Co_2FeSi is one of the highest measured efficiencies.
[c]Reference [48].
[d]Reference [49].
[e]Reference [50].
[f]Reference [51].

a channel [32] and has one of the highest Curie temperatures. Co_2MnSi (CMS) is a promising half metal Heusler as it has a large magnetic moment and a very high Curie temperature [50, 52] as shown in Table 1.1. First principle DFT calculations show CMS to have one of the largest bandgaps, for a half metal, in the minority spin DOS (0.67 eV) with the Fermi energy placed roughly at the middle of the gap [44]. Figure 1.7 shows the

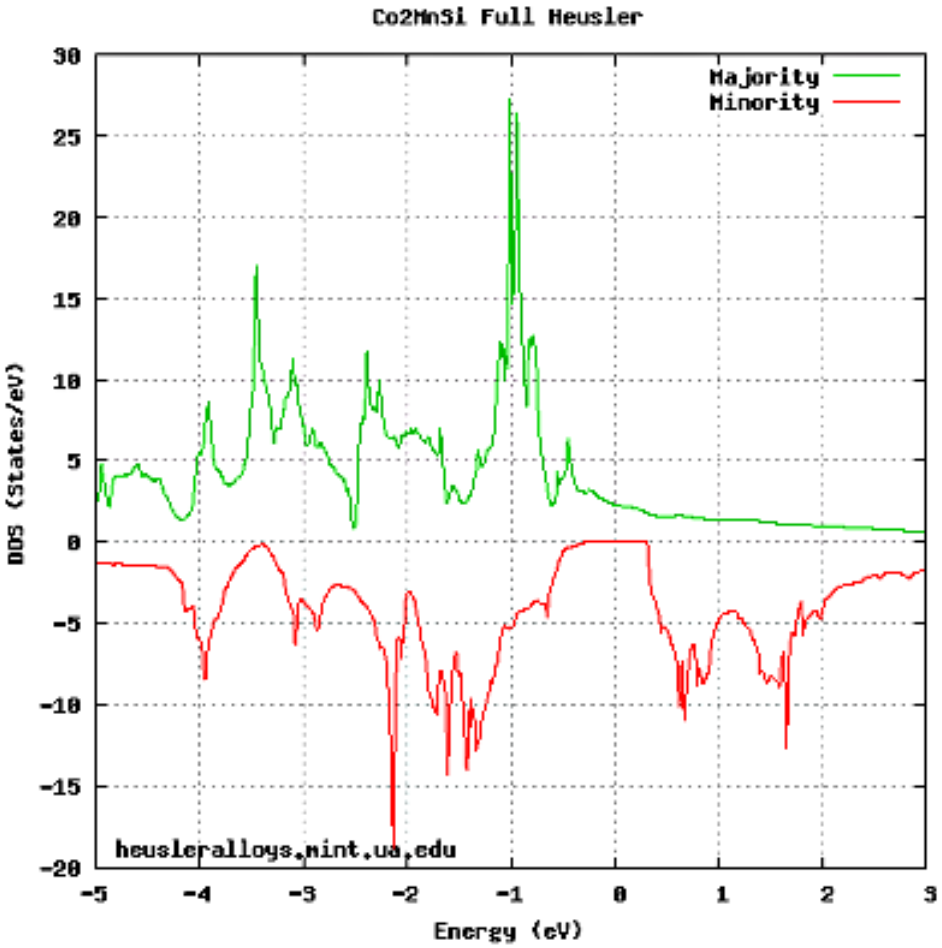

Figure 1.7: Calculated DOS per formula unit (States/eV) as a function of the Energy (eV) for bulk Co_2MnSi. The zero of the energy axis corresponds to the Fermi energy, E_F (adapted from Ref. [44]).

ab initio DFT calculated DOS of bulk CMS. The electronic states show that the Heusler alloy is metallic in the majority band (green curve) and semiconducting in the minority band (red curve), with a large bandgap around the Fermi level.

A mention about the effect of spin–orbit coupling in Heusler alloys would be relevant here. In half-metal Heuslers, the minority valence bands are completely occupied. In the majority bands, the DOS at the Fermi energy is relatively small since most of the d-states

are occupied (fully occupied in CMS). Thus the orbital moments are almost completely quenched. Spin moments are the dominant magnetic moment in Heusler compounds [53, 54]. Therefore the magnetic anisotropy of the half-metal Heusler alloys will usually be small.

1.4 Importance of GaAs

In spintronics research, Gallium arsenide (GaAs) has been widely used as the base semiconductor since mid-90s. GaAs is a III–V semiconductor with a zinc-blende crystal structure as shown in Fig. 1.8. It has a lattice parameter $a = 5.65\,\text{Å}$ and a large direct

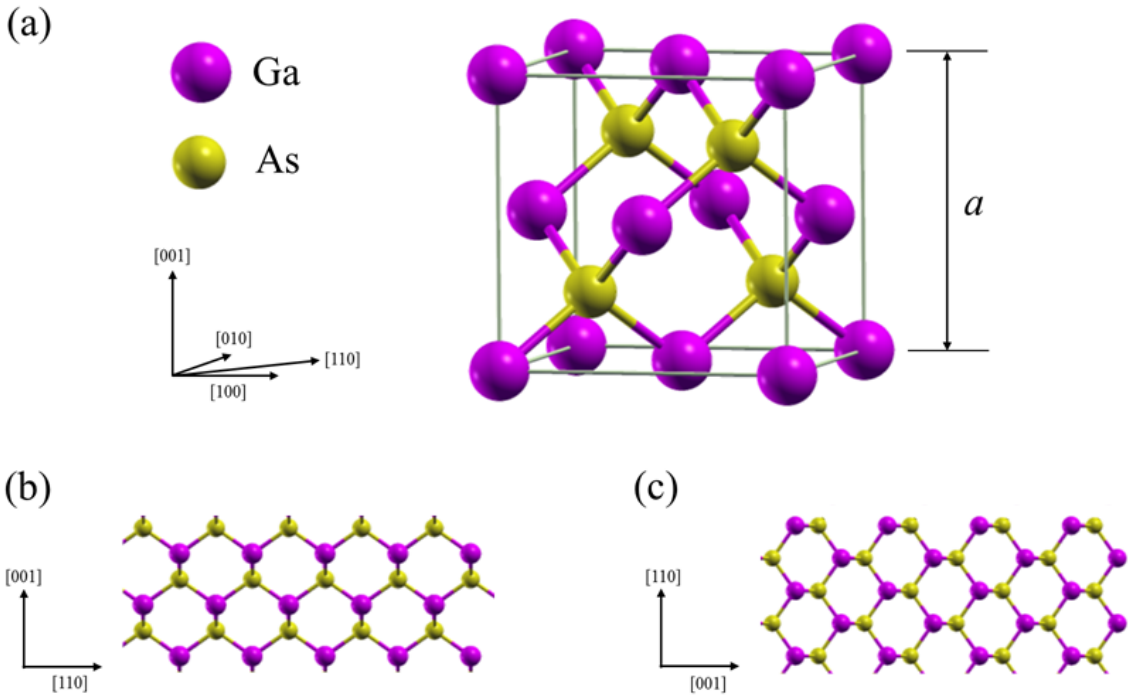

Figure 1.8: (a) Ball-and-stick representation of GaAs zinc-blende unit cell. Layerwise atomic composition in (b) GaAs(001) and (c) GaAs(110).

bandgap of 1.424 eV (at 300 K). The direct band-gap of GaAs is an advantageous aspect since a number of optical techniques can be used to create and detect spin polarized carrier populations within the semiconductor [55]. Moreover, the zinc-blende crystal structure and lattice parameter of GaAs are compatible with a variety of half metals such as full-Heusler alloys (Co_2MnSi, Co_2CrSi), half-Heusler alloys (NiMnAs), and pnictides (CrAs, MnGe) [56]. Substitution of small concentrations of Mn for the host elements in

GaAs was found to induce ferromagnetism, which formed a new class of elements called dilute magnetic semiconductors [12]. At low temperatures, moderately n-doped GaAs semiconductors near the metal–insulator transition (MIT) region are found to have spin relaxation lifetime $\tau_s \sim 100\,\text{ns}$ [13, 57]. The spin-diffusion length, a charecteristic length scale for spin transport in semiconductors, is given by $\lambda_s = \sqrt{D\tau_s}$, where D is the spin diffusion coefficient. For n-GaAs near the MIT region, λ_s is of the order of several microns [58].

1.4.1 D'yakonov–Perel' mechanism

Understanding the mechanism of spin relaxation in semiconductors is central in spintronics. GaAs is a compound semiconductor that lacks crystallographic inversion symmetry due to the presence of two distinct atomic species in the Bravais lattice, creating Dresselhaus-type spin–orbit coupling in it. Moreover, structural inversion symmetry could be broken by the presence of electric fields (internal or external), as is the case in devices such as SPIN-FETs, creating Rashba-type spin–orbit interactions. In n-GaAs near the MIT region, the D'yakonov–Perel' (D–P) mechanism is the dominant cause for spin relaxation [59], as the effective spin–orbit field causes electron spin to precess during diffusive transport. In a quantum wire (quasi 1-D system), the velocity of the electron is always along the wire direction (+x direction), as shown in Fig. 1.9. If this direction is assumed to be the crystallographic [100] direction, then the Dresselhaus field will be along the x-direction ($\vec{B}_{Dresselhaus}(\vec{v}) \propto v_x\hat{x}$). If the symmetry breaking electric field is along the y-direction, then the Rashba field will be along the z-direction ($\vec{B}_{Rashba}(\vec{v}) \propto v_x\hat{z}$). The resultant magnetic field will be along the x–z plane. This effective field interacts with the moment of the incoming electron's spin or the net spin polarization of an ensemble of charge carriers, causing spin relaxation. There are theoretical postulations and experimental demonstration that show that when the transverse dimension of the quantum wire shrinks, the strength of D–P relaxation reduces causing longer spin relaxation times [60, 61, 62]. Although the original SPIN-FET proposed by Datta and Das [11] is based on quantum wells, quantum wire channels are believed to be better suited for the above mentioned reason.

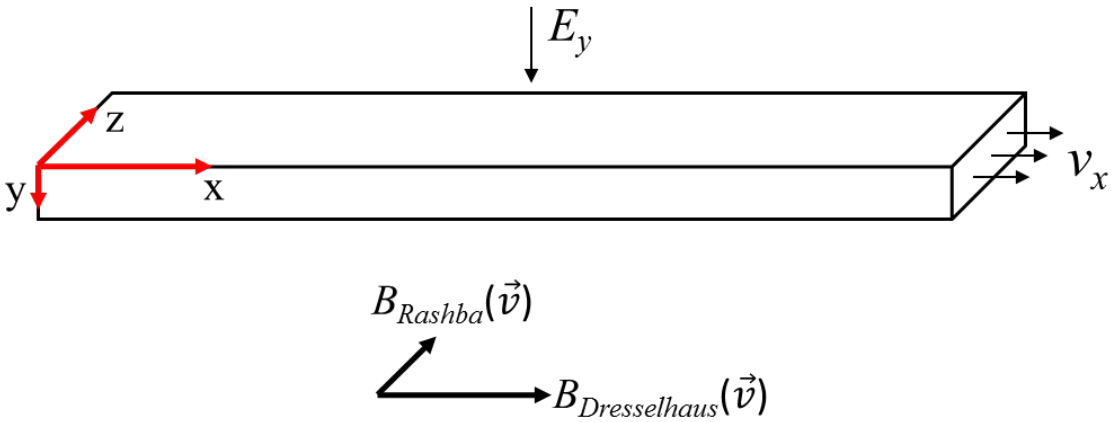

Figure 1.9: Schematic of a quantum wire with rectangular cross-section. Electrons flow along the direction of the wire (+x-direction) and the electric field is along the y-direction. The direction of the Dresselhaus and Rashba fields are also shown for such an arrangement.

In compound semiconductors, the atomic composition is different in different directions along the crystal lattice, as shown in Fig. 1.8(b) and (c). The Dresselhaus interaction is dependent on the crystallographic orientation (Miller indices) of the channel material, giving rise to an anisotropy in spin relaxation. This means the direction of spin transport within a crystal will decide the strength of spin relaxation. This anisotropy was experimentally demonstrated by Ohno et. al. using GaAs quantum wells [63]. They have shown that spin relaxation time was of nanosecond order at room temperature for GaAs(110) quantum wells, an order of magnitude larger than in GaAs(100) quantum wells.

CHAPTER 2

METHODS

Ab initio density functional theory as implemented in the Vienna *Ab initio* Simulations Package (VASP) [64, 65] is the primary modeling technique used in this study. VASP is a computational package that calculates the ground state energy, electronic structure, magnetic structure etc. among other things, of solid state systems by providing approximate solutions to the many-body Schrödinger equation, through solving the Kohn–Sham equations [66]. Below, I give a brief overview of Density Functional Theory (DFT).

2.1 Density functional theory

In many-body solid state systems, the ultimate goal is to solve the time-independent, non-relativistic Schrödinger equation. The hamiltonian for a many-body system can be expressed as

$$\begin{aligned}\hat{H} = &-\frac{\hbar^2}{2m_{\mathrm{e}}}\sum_i \nabla^2_{\mathbf{r}_i} - \sum_j \frac{\hbar^2}{2M_{\mathrm{N}_j}}\nabla^2_{\mathbf{R}_j} + \frac{1}{2}\sum_{i\neq j}\frac{e^2}{4\pi\epsilon_0|\mathbf{r}_i-\mathbf{r}_j|} \\ &- \frac{1}{2}\sum_{i,j}\frac{Z_j e^2}{4\pi\epsilon_0|\mathbf{r}_i-\mathbf{R}_j|} + \frac{1}{2}\sum_{i\neq j}\frac{Z_i Z_j e^2}{4\pi\epsilon_0|\mathbf{R}_i-\mathbf{R}_j|}\end{aligned} \tag{2.1}$$

where $\mathbf{r}_i$ is the electron position, $\mathbf{R}_i$ is the nuclei position, Z_i is the atomic number of the i^{th} atom, and ϵ_0 is the permittivity of free space. In the above equation, the first two terms represent the kinetic energy of the electrons and the nuclei. The fourth term represents the attractive electrostatic interaction between the nuclei and the electrons. The third and fifth terms represent the repulsive potential due to the electron–electron and nucleus–nucleus interactions, respectively.

The nuclei are massive compared to the electrons. One can consider the electrons as moving in the field of fixed nuclei. Thus it can be approximated that the nuclear kinetic energy is zero and their potential energy is merely a constant. This is called as Born–Oppenheimer approximation. This approximation greatly simplifies the many-body hamiltonian. But even with this simplification, the many-body problem cannot be solved exactly.

2.1.1 Electron density

In 1964, Hohenberg and Kohn [67] showed that electron charge density, $\rho(\mathbf{r})$, is the central quantity in determining the Hamiltonian and thus all the properties of the many-body system. The electron density is a non-negative function of only the 3 spatial variables and integrates to the total number of electrons. Hohenberg and Kohn showed that the kinetic energy, external potential, and correlation energy are all functionals of the electron charge density. Moreover, they showed that the energy can be expressed as a functional (a functional is a mathematical device that converts an input function, in this case $\rho(\mathbf{r})$ into an output number. It may be compared to a function which converts an input number into an output number.)

$$E\left[\rho(\mathbf{r})\right] = \int v(\mathbf{r})\rho(\mathbf{r})\, d\mathbf{r} + \frac{1}{2}\iint \frac{\rho(\mathbf{r})\rho(\mathbf{r}')}{|\mathbf{r}-\mathbf{r}'|} d\mathbf{r}\, d\mathbf{r}' + F[\rho] \tag{2.2}$$

where $F[\rho]$ is a universal functional of the electron density and $v(\mathbf{r})$ is the external potential (potentials of nuclei). The explicit form of this universal functional is unknown. The minimum value (ground state energy) for Eq. (2.2) can be achieved only if the input density is the true ground state density.

2.1.2 Exchange–Correlation energy

Kohn and Sham in 1965 [66] separated the universal functional, $F[\rho]$, into a kinetic energy term and an exchange–correlation functional, $E_{xc}[\rho]$, reducing the unknown to only the $E_{xc}[\rho]$ term. They suggested to calculate the exact kinetic energy of a non-interacting reference system with the same density as the real, interacting system.

The Local Density Approximation (LDA) was formulated to define an approximate exchange–correlation functionals. In LDA, the concept of a uniform electron gas was used. This is a system in which electrons move in a positive background charge distribution such that the total ensemble is neutral. Here, the exchange–correlation functional, $E_{xc}[\rho]$, is expressed as

$$E_{xc}^{LDA}[\rho] = \int \rho(\mathbf{r})\epsilon_{xc}[\rho(\mathbf{r})]\, d\mathbf{r}. \tag{2.3}$$

Here, $\epsilon_{xc}[\rho(\mathbf{r})]$ is the exchange–correlation energy per particle of a uniform electron gas of density $\rho(\mathbf{r})$. The exchange–correlation energy term, $\epsilon_{xc}[\rho(\mathbf{r})]$, can further be split into separate exchange and correlation terms,

$$\epsilon_{xc}[\rho(\mathbf{r})] = \epsilon_x[\rho(\mathbf{r})] + \epsilon_c[\rho(\mathbf{r})] \tag{2.4}$$

The exchange part of the above equation represents the exchange energy of an electron in a uniform electron gas of a particular density. It was originally derived by Bloch and Dirac [68, 69]. There is no explicit expression for correlation part.

A next logical step to improve the accuracy of the $E_{xc}[\rho]$ was taken by introducing the Generalized Gradient Approximation (GGA), which supplements the local charge density, $\rho(\mathbf{r})$, with its gradient, $\nabla\rho$, for evaluating the exchange–correlation energy. Then the exchange–correlation energy becomes a functional of both the electron density and the gradient of electron density, $E_{xc}[\rho, \nabla\rho]$.

To include electron spin, the local spin-density approximation is used in which the exchange–correlation functional is expressed as a functional of both spin-up and spin-down densities, $\epsilon_{xc}[\rho(\mathbf{r},\uparrow), \rho(\mathbf{r},\downarrow)]$. Generally, $\rho(\mathbf{r},\uparrow) + \rho(\mathbf{r},\downarrow) = \rho(\mathbf{r})$, while for spin-polarized systems, $\rho(\mathbf{r},\uparrow) \neq \rho(\mathbf{r},\downarrow)$.

2.2 Computational Details

Unless stated otherwise, all calculations and electronic structure modeling in this thesis are performed with *ab initio* density functional theory as implemented in the VASP

program [64, 65]. VASP uses plane wave basis sets to express quantities like the one-electron orbitals, the electronic charge density, and the local potential. Pseudopotentials are described by the projector-augmented wave (PAW) method [70]. The Perdew–Burke–Ernzerhof (PBE) version of the GGA to the exchange–correlation function of DFT was adopted [71]. A sufficiently large cut-off energy of 320 eV was chosen for the plane wave basis set for very large systems (more than 60 ions). For calculations of magnetic anisotropy and formation energy, a cut-off energy of 520 eV was chosen to be consistent with results from the Open Quantum Materials Database [72]. The conjugate gradient algorithm as implemented in VASP was used for performing ionic relaxation in crystal structures. An energy change of 1×10^{-6} eV was used as the stopping criterion for structural optimization. For integration cut-off at the Fermi energy, the Methfessel–Paxton method with smearing width of 0.2 eV was used.

CHAPTER 3

MODELING Co_2MnSi/GaAs INTERFACES IN (001) LAYERING

In this chapter, the physical, chemical, electronic, and magnetic properties of complex interfaces observed between various Co_2MnSi/GaAs(001) heterostructures are calculated using ab initio density functional theory calculations to provide insight for device performance in lateral spin valves. Ab initio DFT-based interface models that match closely with STEM micrographs of these heterostructures show diffusion of Mn, Si, and Co ions into the first few layers of GaAs. For a model based on 0.5ML-MnSi-flux initiated CMS/GaAs sample, a complex interface is present that is at least 4 layers thick. For models based on 1ML-Mn, 1ML-MnSi, and 1ML-Co-flux initiated samples, the interfaces are 5 to 6 layers thick with diffusion of Mn inside GaAs, pushing As above into CMS. The density of electronic states of the best-fit DFT models for all the observed samples show that the half-metallicity is destroyed at the interfaces. Atom-resolved DOS shows that the presence of Mn deeper into the interface plays the primary role in destroying the half-metallicity. All the best-fit-DFT models show high spin polarization (from 0.6 to 0.8) at the Fermi level.

3.1 Introduction

Co-based full-Heuslers are promising half metals due to their high magnetic moment/f.u., very high Curie temperatures, and excellent lattice matching with III–V semiconductors. Co_2MnSi (CMS) is particularly promising due to its large bandgap at the

Fermi level for one spin subband [73, 74] and its very small lattice-mismatch (a = 5.63 Å, mismatch $\sim 0.3\%$) with GaAs.

There have been a few promising *ab initio*-based DFT studies that showed the potential of CMS/GaAs heterostructures for (001) layering with large spin polarization across the interface. Initially, Galanakis et. al. [75] studied the surface properties of some half- and full-Heusler half metals and found that for the case of CMS, the surfaces lost half-metalicity with spin polarization nearing zero. Hashemifar et. al. [76, 77] have done extensive first-principle calculations of CMS surfaces and of abrupt terminations of CMS/GaAs with (001) layering. From their atomistic *ab initio* thermodynamics calculations, they conclude that MnSi-, pure Mn-, or pure Si-terminated CMS surfaces can be stabilized under suitable conditions. Analyzing the surface band structure, they found that a pure Mn-terminated CMS surface preserves half-metallicity. They also studied various ideal abrupt terminations of CMS on GaAs with (001) layering and found at least two terminations with high symmetry and low formation energy that preserve the half-metallicity at the interface; one is an ideal abrupt SiMn/As interface and the other, a Mn-rich interface (MnMn/As).

While theoretical studies of ideal abrupt interfaces retaining half-metallicity are promising, actual interfaces are rarely ideal, with diffusion, substitution, and formation of secondary phases being some common causes of the destruction of the ideal nature of interfaces. In a study that investigated the growth of Co_2FeSi on GaAs, it was found that the B2 phase, where Fe and Si are randomly intermixed, was the dominant phase near the interface, whereas the magnetic $L2_1$ phase was dominant away from the interface [78]. This mixed distribution of B2 and $L2_1$ phases was also observed in Co_2MnGe on GaAs by Dong et. al. [31]. Wang et. al. grew Co_2MnSi on GaAs(001) by pulsed laser deposition [79] and observed atomic disorder in Co_2MnSi that caused a reduction in spin polarization. To understand the effect of atomic disorder on spin polarization in Co-based Heuslers, Ozdogan and Galanakis conducted a DFT-based theoretical study for Co_2MnSi and Co_2MnAl and found that Co antisites destroyed the gap whereas random mixing of Mn and Si (Al) kept the half-metallic gap intact [80]. Miura et. al. studied the effects

of disorder in Co_2CrAl and found a similar trend [81]. Picozzi and Freeman studied the effects of point defects in Co_2MnSi and Co_2MnGe and found that Mn antisites can easily occur, due to low formation energies, and that they do not destroy half-metallicity but Co antisites give rise to defect states [82].

The reaction of magnetic species with an As-rich reconstructed-GaAs surface, during growth, has been studied systematically by the Palmstrøm group. When Fe was epitaxially grown on GaAs(001), the interface was shown to favor Fe–As bonding, with no extended interfacial reaction [83]. For MBE-growth of Co on c(4×4) GaAs(001), Co_2GaAs-like phases were observed at the interface between Co and GaAs at low temperature growth, and at higher growth temperature (95 °C), CoGa-like phases were observed in addition to Co_2GaAs-like phases [84]. These phase formations are interpreted to be due to the outdiffusion of Ga from GaAs. In the epitaxial growth of Mn thin films on GaAs(001), the tetragonal Mn_2As phase is formed near the Mn/GaAs interface [85].

Several studies have showed that Mn substituting for surface or subsurface Ga is energetically preferred in Mn/GaAs digital alloys and in (Mn, Ga)As random alloys [86, 87, 88, 89]. Ohtake et. al. have shown that by controlling the As atmosphere during growth, Mn atoms could be incorporated into interstitial sites [90]. Zhang et. al. have observed the GaAs(001):Mn surface and have developed a first-principles based theory for spin-driven reconstruction [91]; at lower Mn coverage, low-energy surface reconstructions are formed that are antiferromagnetic in nature and preserve the semiconducting bandgap.

In this chapter, I present a theoretical study performed to predict and understand the complex interface patterns observed for several CMS/GaAs(001) heterostructures, which were grown elsewhere. An *ab initio* DFT-based predictive modeling approach was used to find energy-minimized structures that agree well with the observed interface patterns in these samples. I present and discuss the physical, chemical, electronic, and magnetic structures of the DFT models for these CMS/GaAs samples to show how the interfaces affect the device performance in lateral spin valve devices.

3.2 Methods

Two types of CMS/GaAs samples were grown by Professor Palmstrøm's group at UCSB, using molecular beam epitaxy (MBE): (i) one set of samples with 0.5ML fluxes of CMS atoms (Co- and MnSi-fluxes) and (ii) one set of samples with 1ML fluxes of CMS atoms, on GaAs substrates. The 0.5ML-flux samples were accidental (intended to be 1ML flux), yet one of the 0.5ML samples gave the best result for non-local spin valve signal measurement. The Heusler alloy Co_2MnSi was deposited using MBE with alternate fluxes of Co and MnSi. Thus, a CMS/GaAs sample with MnSi-initial flux refers to the process of MBE deposition with an initial flux of MnSi, followed by a flux of Co, and so on. The labels 0.5ML and 1ML refer to the growth rate of the incoming flux (expressed in units of atoms/cm^2/s). High resolution scanning transmission electron microscopy (STEM) and electron energy loss spectroscopy (EELS) measurements were performed by Professor Voyles' group at the University of Wisconsin. Due to the presence of carbon contamination in the 0.5ML CMS/GaAs samples, there were constraints on scanning the electron beams for longer times, which prevented the group from acquiring EELS spectra for these samples. The CMS/GaAs samples with 1ML-flux were free of carbon contamination, which permitted the acquisition of both STEM and EELS measurements of the interfaces in these samples.

Ohtake et. al. [92, 93, 94] showed that, under ambient conditions in MBE, it is easy to produce As-rich stable reconstructions of the GaAs surface, known as c$(4 \times 4)\beta$-reconstructed GaAs. Figure 3.1 shows the beta structure model for As-rich GaAs(001)-c(4×4) surface reconstruction; (a) the top view of the GaAs(001)-c$(4 \times 4)\beta$ surface ([001] into screen) and (b) side view ([1-10] into screen). In Fig. 3.1, three layers are displayed (bottom - Ga, middle - surface As, and top - As–As dimer). Filled (open) circles denote As (Ga) atoms. A simple As-terminated GaAs(001) surface will have two dangling bonds, whereas in the above reconstructed structure, the As–As dimers compensate for these dangling bonds, making it a stable As-rich surface. It should be noted that the top surface of this particular As-rich GaAs reconstruction has only 0.75 ML coverage.

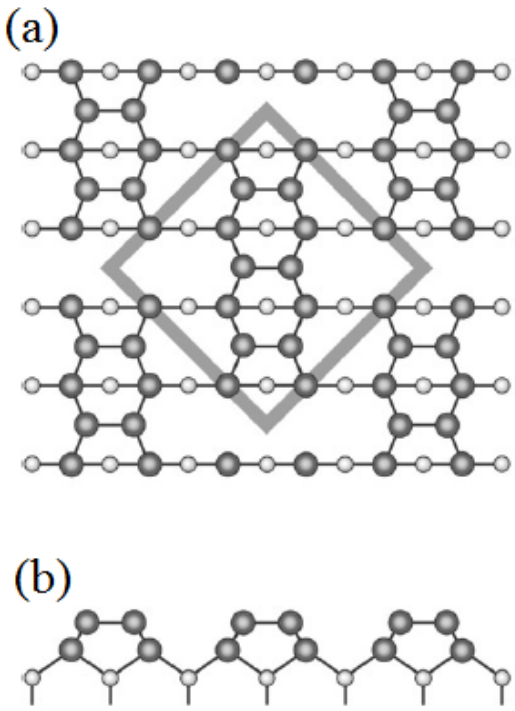

Figure 3.1: The β-structure model for As-rich GaAs(001)-c(4×4) surface reconstruction. (a) Top view of the GaAs(001)-c$(4\times4)\beta$ surface ([001] into screen) and (b) side view ([1-10] into screen) of the surface. Filled (open) circles denote As (Ga) atoms.

A similar $c(4\times4)\beta$-reconstructed GaAs surface was grown in Palmstrøm's group using MBE, by growing a several nm-thick GaAs buffer layer at high temperature and cooling it under As_4 flux. The 0.5ML Co_2MnSi/GaAs samples with MnSi as initial flux were deposited at a growth temperature of 270 °C. One part of the sample was patterned into a non-local spin valve structure for measurement of the spin polarization and the other part was used to perform high-resolution Z-contrast Scanning Transmission Electron Microscopy (STEM) to elucidate the interface atomic structure. Non-local spin valve measurements were performed by Professor Crowell's group at the University of Minnesota. They found that samples initiated with MnSi flux have spin signals twice greater than samples initiated with Co flux. Non-local spin valve measurements are shown in Fig. 3.2.

Before discussing in detail the atomic arrangement in and near the complex interface of the 0.5ML sample, as observed in the STEM image, I will first discuss the theoretical ideal abrupt terminations in CMS/GaAs(001) that preserve the half-metallic characteristic of the Heusler alloy Co_2MnSi at the interface of the heterostructure. To begin with,

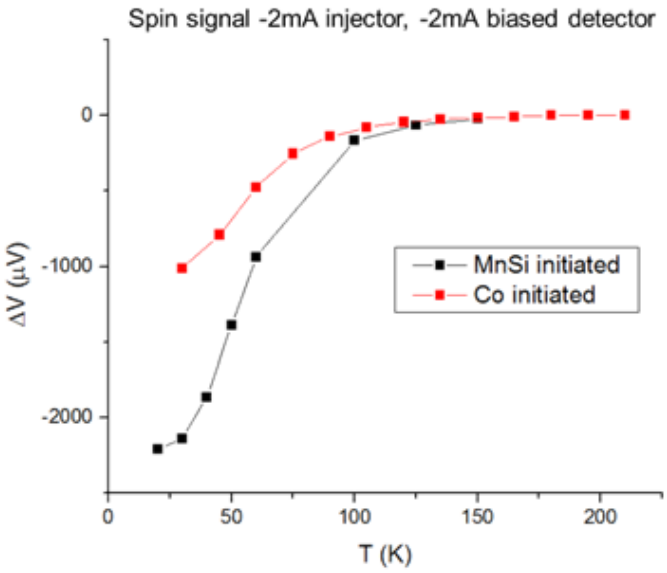

Figure 3.2: Non-local spin valve measurement of Co_2MnSi/GaAs samples initiated with MnSi- and Co-flux.

Figure 3.3 shows the ball-and-stick representations of cubic unit cells of (a) Co_2MnSi and (b) GaAs in (001) direction. Co_2MnSi is a full-Heusler alloy with $L2_1$ crystal structure comprising 4 interpenetrating fcc sublattices. In the (001) layering direction, CMS consists of alternating layers of Co and MnSi. GaAs crystallizes in the zinc-blende structure and has alternate layers of Ga and As in the (001) direction. Since the lattice matching is very good ($\sim 0.3\%$) between CMS and GaAs, it is possible to layer CMS on a GaAs substrate for a long range without distortions. Based on symmetry arguments, it is possible to deposit CMS on top of GaAs in the (001) direction in multiple ways, with terminations such as SiMn/As, CoCo/As, SiMn/Ga, etc. If the terminations are ideal, there are many ways for the ions to arrange, say, for a SiMn/As termination, Mn ions could be placed above As ions and Si ions could be above As on bridge sites or vice versa. Hashemifar et. al. [76] performed *ab initio* DFT calculations for many different terminations of CMS/GaAs(001), with different patterns of atomic arrangements in each of the terminations, and found two geometries with SiMn/As termination that preserve the half-metallic character of the Heusler alloy at the interface. For the Mn-rich interface with MnMn/As termination, they found one geometry which preserved the half-metallicity. All three patterns are characterized by high symmetry and low formation energy. Figure 3.4 shows the schematic top view of two different high symmetry patterns for the ideal

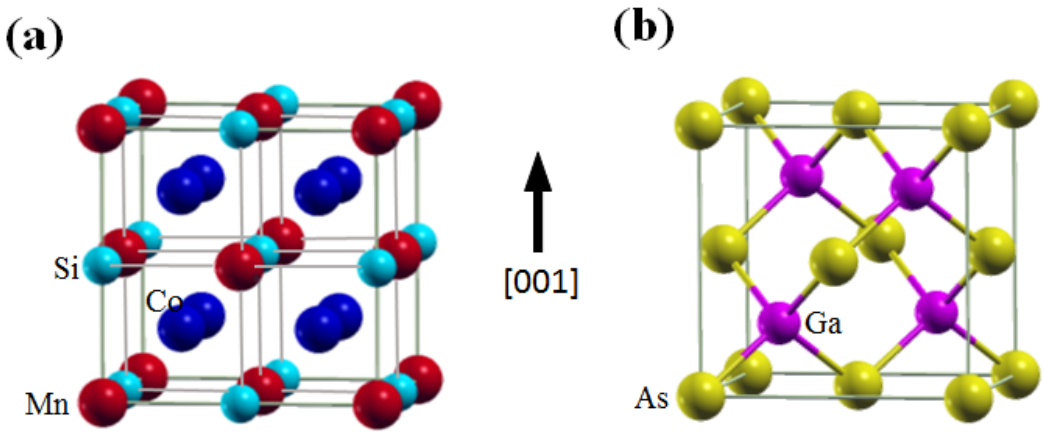

Figure 3.3: Ball-and-stick representations of cubic unit cell of (a) Co_2MnSi and (b) GaAs in (001) direction.

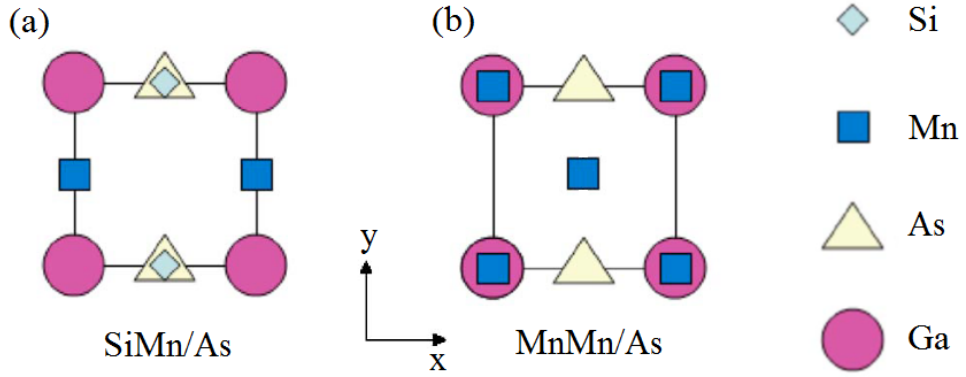

Figure 3.4: Schematic top view of high symmetry patterns in CMS/GaAs(001) for the ideal abrupt (a) SiMn/As termination and (b) MnMn/As termination.

abrupt (a) SiMn/As termination and (b) MnMn/As terminations in CMS/GaAs(001). The topview in Fig. 3.4(a) and (b) actually shows three layers near the ideal abrupt interface; Ga is the bottom layer, As is in the middle layer, and the top layer consists of (a) Mn and Si and (b) Mn. For the SiMn/As termination, Si ions are on top of As and Mn ions are in the hollow sites. For the MnMn/As termination, Mn ions occupy the bridge sites between As atoms.

To generate supercells that could model the above ideal abrupt terminations, a tetragonal unit cell is chosen with the square basis (of GaAs) rotated by 45° with respect to the cubic axis of the unit cell. The in-plane lattice parameter of the supercell is set to the experimental lattice constant of GaAs: $a = a_{\text{exp}}/\sqrt{2}$, where $a_{\text{exp}}(\text{GaAs}) = 5.65\,\text{Å}$. The periodic CMS/GaAs supercell consists of 15 layers of GaAs (8 layers of As, 7 layers of Ga) and 11 layers of CMS [6 layers of SiMn(MnMn) and 5 layers of Co]. The height of the supercell (c parameter) is optimized along the z-direction. The atomic positions (internal microscopic degrees of freedom) were also optimized by calculating and minimizing the magnitude of the interatomic forces. Figure 3.5 shows a periodic supercell of CMS/GaAs(001) heterostructure with an ideal abrupt SiMn/As termination.

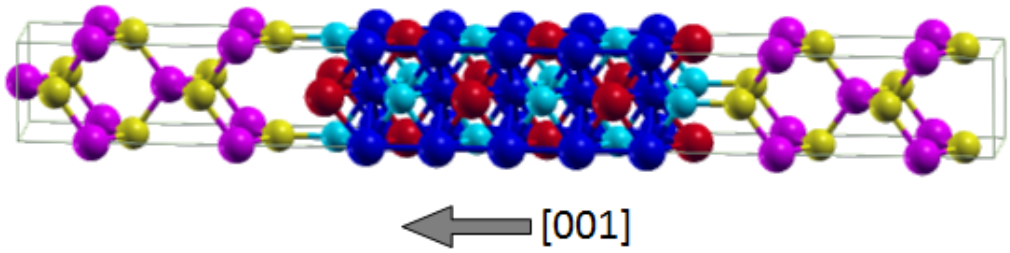

Figure 3.5: Ball-and-stick representation of a periodic supercell of CMS/GaAs(001) heterostructure with SiMn/As ideal abrupt termination. Color code of ions used in Fig. 3.4 is followed here.

3.2.1 Co_2MnSi/GaAs(001) with 0.5ML-flux

High resolution Z-contrast STEM of the CMS/GaAs interface along the [110] and [1-10] directions was performed by Professor Voyles' group. This STEM data was used to guide the construction of DFT models of the interface structure. Figure 3.6 shows high resolution Z-contrast STEM images of the 0.5ML-MnSi-initial-flux CMS/GaAs interface along the [1-10] and [110] directions. The technical details of the STEM imaging is beyond

the scope of this research. The figure shows planar side views of the sample from two orthogonal directions ([1-10] and [110] into screen). The lower part of the structure is GaAs and the upper part is CMS, with a complex interface in between, extending to at least 4 layers, due to diffusion of, probably, Mn and/or Si ions into the As-dimer row and into the first few layers of GaAs surface.

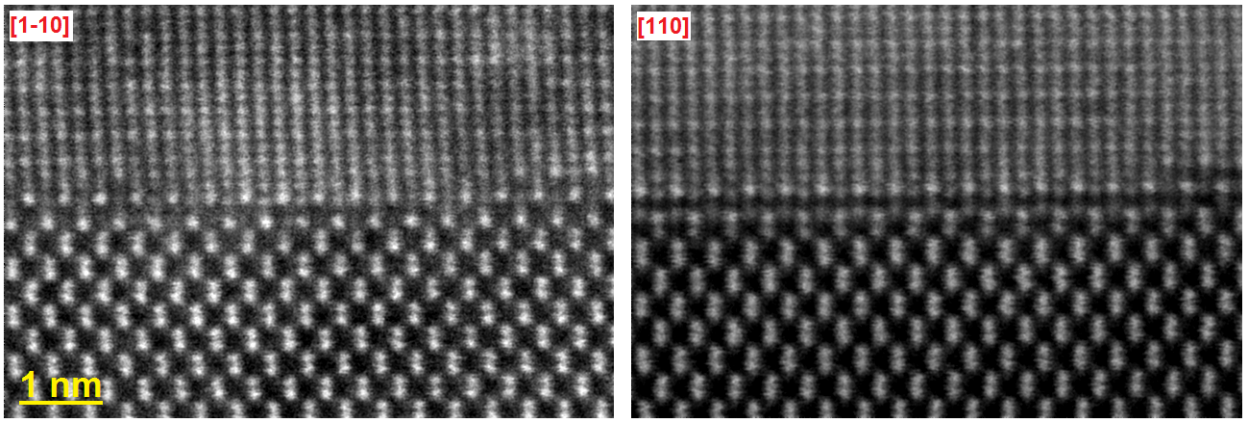

Figure 3.6: Z-contrast STEM micrographs of the CMS/GaAs interface along the [1-10] and [110] directions.

The Z-contrast STEM images from two orthogonal directions provide information about the physical properties of the complex interface that can guide in the predictive modeling approach to decode the physical and chemical structure of the complex interface. From the STEM micrographs, the ion distances can be measured to within $\pm 10\,\mathrm{pm}$. As the name of the technique suggests, atoms with high atomic number, Z, have high contrast in the images. It should be noted that the Heusler alloy CMS grows in B2 phase for the first few nm, near the interface. This is the reason for the absence of low-contrast Si atoms in the CMS region in the STEM images. The images from two orthogonal planes suggest that there are at least 4 layers of interface, including the As-dimer row as the last layer of the complex interface. It can also be inferred from the STEM image that the initial flux of MnSi has most probably diffused through the As–As dimer row and formed layers in between the As–As dimer row and surface row As. In the CMS part of the STEM micrograph, we see alternative layers with comparatively high contrast ions, suggesting these to be Co layers. These Co layers seem to begin immediately after the termination of the complex interface. In between the alternate layers of Co is layers of

Mn, forming B2 phase, based on the Z-contrast of the STEM image. However, we use MnSi to model these layers. Based on this information and from the placement of atoms as seen from the two orthogonal planes in the STEM images, a schematic represention of the atom position in each layer can be drawn to understand and explain the basis for predictive modeling.

Figure 3.7 shows a schematic topview of 6 layers in and near one possible interpretation of the complex interface. The solid square in each layer represents the smallest unit cell that can model this complex interface pattern. Figure 3.7(a) is subsurface Ga. A slight

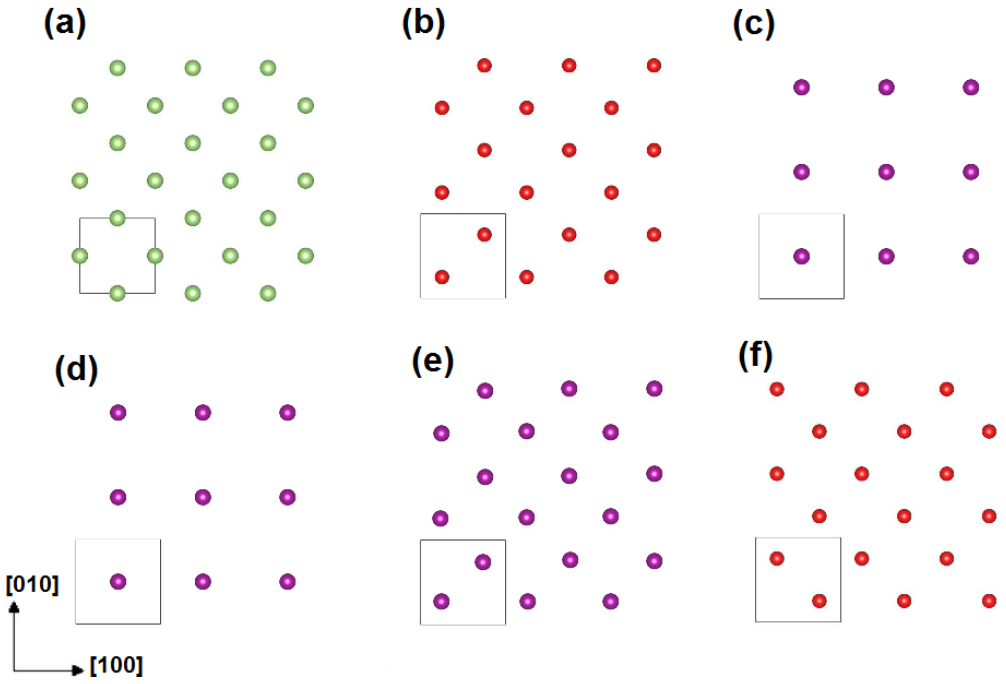

Figure 3.7: Schematic layer-by-layer top view of the complex interface and two layers of GaAs. (a) Subsurface Ga, (b) As, (c) Interface 1, Si or Mn, (d) Interface 2, Si or Mn ($\sim 60\%$ occupied), (e) Interface 3, Si or Mn, and (f) Interface 4, dimer row As.

contrast difference in ions in this layer casts suspicion that this layer is actually Ga. Substitution of Mn for Ga in this layer is highly probable based on previous findings in literature. Equivalent models with either Ga or Mn in this layer have been tested. Figure 3.7(b) is an As layer. This is the last layer of bulk GaAs. We denote the layer of atoms represented by Fig. 3.7(c) as interface 1. This is the first layer of the complex interface. It has Mn or Si atoms on bridge sites above As. Ions in interface 1 are 40 ± 10 pm above the surface As layer. This layer could either be Si or Mn and ion placement here is similar to

the ion placement as observed by LeBeau et. al. [83] at the interface for Fe/GaAs(001). The lattice structure of ions in this layer is equivalent to that of As planes with vacancies at alternate sites. Figure 3.7(d) represents interface 2. Ions in this layer could either be right above ions in interface 1 or above interface 1 vacancy sites. This layer could have either Si or Mn. From STEM observations, this layer seems to be roughly 60% occupied. For convenience of modeling, this layer is taken to be either 0% occupied or 50% occupied. Note that if we reduce the occupancy in interface 2 to be 50%, a bigger unit cell has is needed to model the pattern. (e) Ions in interface 3 are 270 ± 10 pm above the As ions in (b). Its ions could be Si or Mn. (f) This is interface 4 of the complex interface. The As–As dimer row of the original GaAs-reconstruction has shifted to interface 4. Note that the schematic shows 1 ML coverage of As in interface 4, whereas the As–As dimer row has 0.75 ML coverage. This is again on account of simplifying the model. Since the initial flux in the MBE growth for this sample is 0.5ML MnSi, the schematic shows the ions at interfaces 1 to 3 to be either Mn or Si. But it is possible for Co to be present in these interface layers. For predictive modeling, Co too is considered in these interface layers. Figure 3.8 shows interlayer separation in the interface as measured from the STEM micrographs. All dimensions are measured to within ± 10 pm.

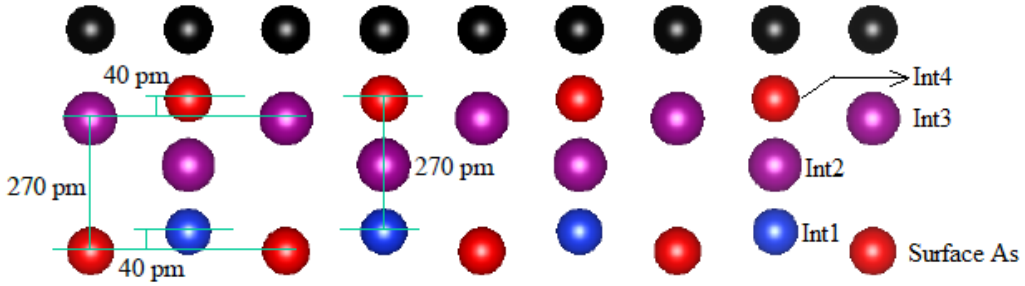

Figure 3.8: Interlayer separation of the complex interface as measured from the STEM micrographs.

With Mn, Si, or Co in interface layers 1 to 3, and by modeling Int2 with 0% or 50% occupancy, there are multiple combinations in which a periodic supercell could be modeled for *ab initio* DFT-based energy minimization to look for structures that could agree well with the physical structure as observed by the STEM imaging. Once a DFT model is relaxed by reducing the interatomic forces to less than 0.01 eV/Å, the Quantum

Mechanical-simulated STEM micrograph of the DFT-relaxed structure can be computed from first principles using the multislice method for electrons in the energy range of approximately 100 keV to 1000 keV [95]. The interlayer separation of the DFT-relaxed structure model can also be measured and the results can be compared with the experimental distances shown in Fig. 3.8.

Figure 3.9 shows the ball-and-stick representation of two supercell structures used to model the complex interface in 0.5ML CMS/GaAs(001) by electronic structure calculation; (a) supercell to model 0% occupancy at interface layer 2 (Int2) and (b) supercell to model 50% occupancy at Int2. A portion of the interface for the 50% occupancy model is zoomed out and labeled to show the interface layers clearly. The superlattices

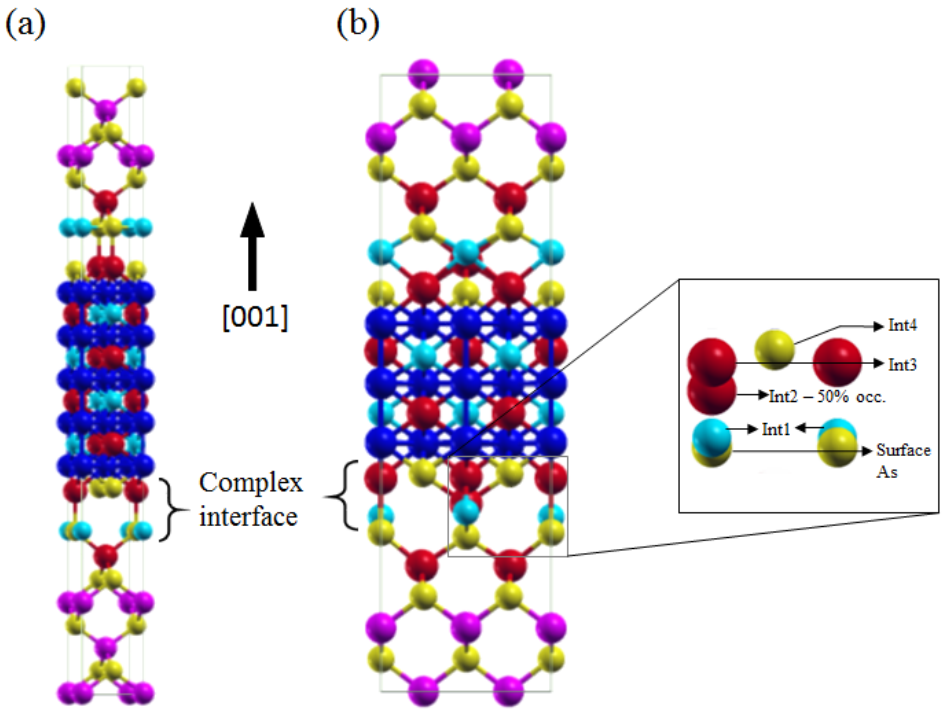

Figure 3.9: Ball-and-stick representation of the periodic supercell structures to model the complex interface in 0.5ML-flux CMS/GaAs(001) with (a) 0% occupancy in Int2 and (b) 50% occupancy in Int2. A part of the interface for the 50% occupancy model is zoomed out and labeled to show the interface layers clearly.

are tetragonal unit cells with square bases and the in-plane lattice parameter of the cell is set to the experimental lattice constant of GaAs; for the smaller cell in Fig. 3.9(a) $a = a_{exp}/\sqrt{2}$ and for the larger cell in Fig. 3.9(b) $a = a_{exp} * \sqrt{2}$, where $a_{exp} = 5.65\,\mathring{A}$. The cell in Fig. 3.9(a) has 15 layers of GaAs, 9 layers of CMS, and 3 layers of the complex

interface (0% occupancy at Int2) on both sides of the heterojunction, with a total of 39 ions in the supercell. In this model, with ions at the interface remaining the same, subsurface Ga (on both sides of the interface) is substituted with Mn ions, as that seemed a possibility by inferring atom identities from the z-contrast in the STEM image. The cell in Fig. 3.9(b) has 11 layers of GaAs, 5 layers of CMS, and 4 layers of the complex interface on both sides of the heterojunction, with a total of 106 ions in the supercell. This larger cell was used to compare models in which Int1 or Int2 had full or half occupancy. A partial occupancy at Int1 corresponds to the interface coverage as observed for Fe/GaAs(001) by LeBeau et. al. [83]. The height of the supercell (c parameter) is optimized by minimizing the stress along the z-direction. The atomic positions (internal microscopic degrees of freedom) were also optimized by calculating and minimizing the magnitude of the interatomic forces. Plane wave basis sets with cut-off energy of 357 eV were used for self-consistent field calculations. The integration in the irreducible wedge of the supercell Brillouin zone was performed using a (8, 8, 1) k-point mesh according to the Monkhorst–Pack scheme [96].

For metastable structures relaxed from DFT calculations, energy of formation/atom can be computed as follows:

$$E_{\text{form}} = \frac{E_{\text{tot}} - \sum_i n_i * \mu_i}{\sum_i n_i}, \qquad \text{for} \qquad i = \text{Co, Mn, Si, As, and Ga} \tag{3.1}$$

where E_{tot} is the total energy for a model obtained from self-consistent energy calculation in DFT, n_i is the number of constituent ions in the model, and μ_i is the chemical potential for the i^{th} element.

3.2.2 Co_2MnSi/GaAs(001) with 1ML-flux

In the case of 1ML-flux growth of CMS/GaAs(001), three samples with different initial flux (MnSi-, Mn-, and Co-flux) were prepared by Professor Palmstrøm's group. For these three 1ML samples with different initial fluxes, high-resolution STEM along with EELS spectra were taken by Professor Voyles' group. In addition to information about the atom position and distance between ionic species in the heterojunction derived from the

STEM micrographs, chemical analysis provided information about the identity of ions in the complex interface with a certain level of confidence. Figure 3.10 shows the STEM and the EELS spectral imaging performed on a 1ML MnSi-initial flux CMS/GaAs(001) sample ([110] into the screen). In Fig. 3.10(a), the area inside the green rectangular

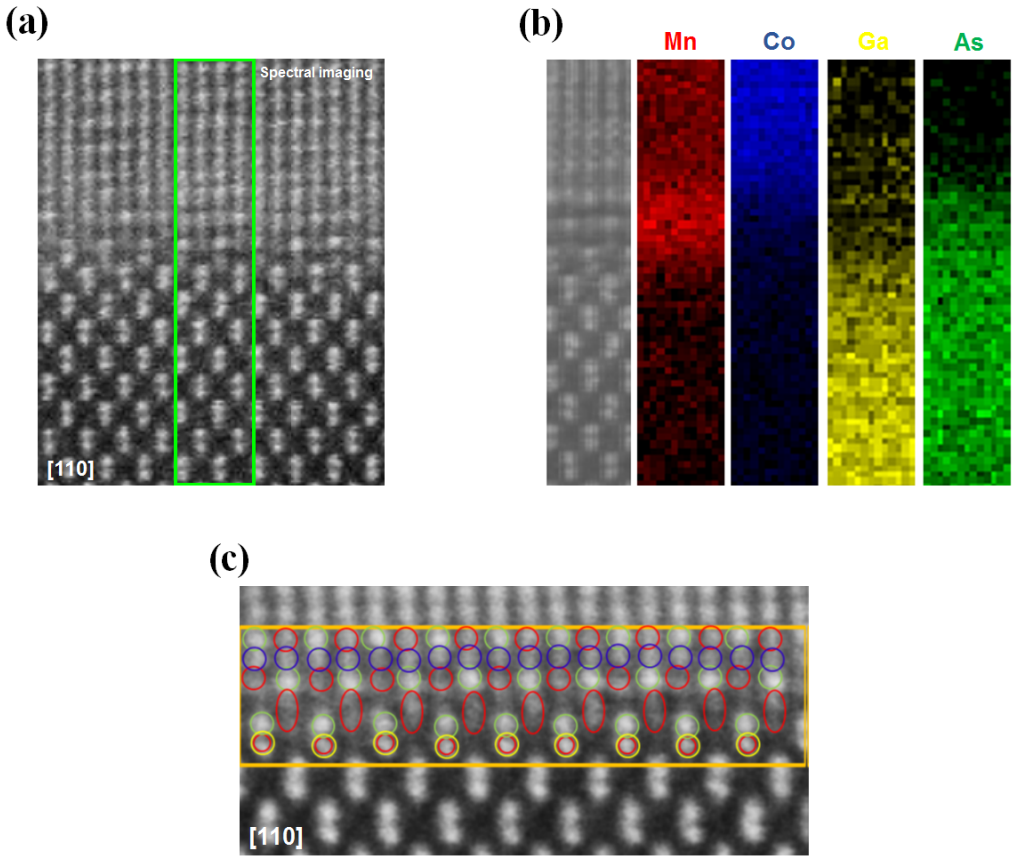

Figure 3.10: STEM micrograph of 1ML CMS/GaAs(001) with MnSi-initial flux ([110] into the screen) and EELS spectral imaging. (a) STEM micrograph at [110] plane with green rectangle specifying the spectral imaging region. (b) Spectral mapping of four atomic species at the specified region (Colors: Mn - red, Co - blue, Ga - yellow, and As - green). (c) The spectral mapping result is overlayed as circles and ovals with atom-specific colors above the STEM micrograph to schematically represent the position of each atom in the interface.

region is chosen for EELS spectral scanning of the ionic species, the results of which for 4 atoms (Mn - red, Co - blue, Ga - yellow, and As - green) are shown in Fig. 3.10(b). Based on the EELS spectra and the spectral mapping, a schematic of the chemical composition at the complex interface for 1ML MnSi-initial flux CMS/GaAs(001) is overlayed on the STEM micrograph [shown in Fig. 3.10(c)]. The interface, in this case, is at least 6 layers

thick, with As pushed above into the CMS region and Mn pushed at least 2 layers into the GaAs. A Mn_2As like region is formed inside the first 4 layers of the interface.

For all the three samples with different initial flux (MnSi-, Mn-, and Co-flux) in 1ML CMS/GaAs(001), STEM and EELS spectral mapping were performed in two orthogonal planes ([110] into the screen and [1-10] into the screen) by Professor Voyles' group. In all three cases, the interface is at least 6 layers thick, with rich Mn presence. In all three cases, EELS spectra of Si is inconclusive and Si could be present anywhere within the interface in the DFT models. With this information, supercells similar to the 0.5ML case were created for *ab initio* DFT calculation of the interfacial structure in each case of 1ML-flux samples.

3.3 Results and Discussion

3.3.1 Co_2MnSi/GaAs(001) with 0.5ML-flux

As described in Section 3.2, a predictive modeling approach was used to search for metastable DFT structures consistent with the experimental observation of the complex interface pattern in 0.5ML CMS/GaAs(001). Using the two supercells shown in Fig. 3.9, metastable structures for more than 90 models of the complex interface structure were calculated. Out of these, a handful of model structures compared well with the experimental structure after comparing the experimental STEM images with the simulated STEM images (from DFT models), and also after comparing the inter-atomic distances of the experimental samples with that of DFT models. In cases where the comparison between experiment and the DFT model was good, the formation energy/atom was calculated. The results for the best-fit model is presented in detail here. The detailed results of other DFT models that agree reasonably well with the experiment are presented in the Appendix.

Figure 3.11 shows the ball-and-stick representation of the best-fit DFT model for the 0.5ML CMS/GaAs(001) sample with MnSi-initial flux. The figure shows the interface pattern in two projections (left side: [1-10] into screen, right side: [110] into screen). On the right side, the ions in and near the interface are labeled for clarity. As shown in the

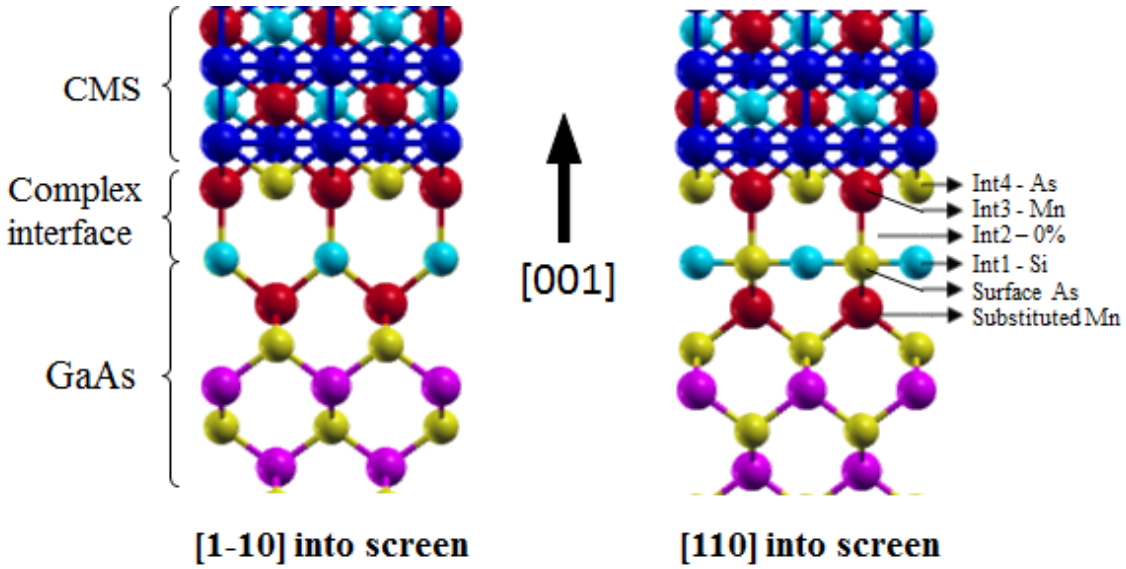

Figure 3.11: Ball-and-stick representation of the complex interface structure in the best-fit DFT model for 0.5ML CMS/GaAs(001) with MnSi-initial flux, shown in two projections (left side: [1-10] into screen, right side: [110] into screen). Color scheme: Co - blue, Mn - red, Si - turquosie, Ga - purple, As - yellow.

figure, the interface in the best-fit DFT model has a Si atom at Int1, which is at the same layer as the 'surface As'. The Si atom fills every vacancy site of the 'surface As' (unlike LeBeau et. al. [83], where Fe fills alternative sites above 'surface As'). Si at Int1 has 'surface As' as its nearest neighbor with a separation of 2 Å. Interface 2 (Int2) is modeled with 0% occupancy in this model. In models where Int2 is 50% occupied, the 'surface As' displaces considerably in the x–y plane, thus appearing asymmetric in one of the projections (inconsistent with the STEM image). Observing the atom displacement after relaxation in almost all models, it is certain that Int3 is occupied by Mn, since Si or Co in this position distorts the structure of the interface very differently from the experimental STEM. Mn at interface 3 (Int3) is equidistant from Co (first layer of CMS above the interface) and 'surface As' (2.59 Å). In the above DFT model, Int4 is completely covered with As, as described in Fig. 3.7(f), and is separated from Co, its nearest neighbor above it, by 2.47 Å. The subsurface Ga is substituted with a Mn atom as labeled in Fig. 3.11. The substituted Mn increases the Mn–As bondlength by 4% (2.57 Å) compared to the original Ga–As bondlength of 2.47 Å. The properties of a similar DFT model, with no Mn substitution, will be compared with that of the best-fit model, later in this chapter.

Table 3.1 compares the experimental projected planar atomic distances (z-separation) in the complex interface with that of the best-fit DFT model. The atom separation distances agree to within 30 pm.

Table 3.1: Comparison of the projected-planar atomic distances (z-separation) in the complex interface, as measured from the STEM image, with that of the best-fit DFT model

	Planar-projected distance (pm)	
	Experimental[a]	Best-fit DFT
Surface As–Int1	40 ± 10	0
Surface As–Int3	270 ± 10	260
Int1–Int4	270 ± 10	277
Int3–Int4	40 ± 10	20

[a]Figure 3.8.

Figure 3.12 shows the comparison of a quantum-simulated STEM generated for the best-fit DFT model with the STEM image of the experimental sample viewed from two orthogonal directions (top row: [110] and bottom row: [1-10]). The QM-simulated STEM of the best-fit DFT model agrees well with the experimental STEM of the 0.5ML CMS/-GaAs(001) sample with 0.5ML-flux MnSi initiation.

The spin-resolved total density of states (DOS) of the periodic supercell of the best-fit DFT model is shown in Fig. 3.13. For comparison, the total DOS of CMS/GaAs(001) with an ideal abrupt SiMn/As termination (shadowed portion of the plot) is added to the DOS plot in Fig. 3.13. The most important feature in this plot is the presence of a finite density of interface states at the Fermi level for the minority spin band in the DOS plot for the best-fit DFT model. Thus, the complex interface does not posses the half-metallic character of the Heusler alloy, Co_2MnSi. However, there is still a large spin polarization at the Fermi level (P = 0.67) due to the disproportionately large number of states for the majority band compared to that of the minority band. This feature of large spin polarization (P > 0.5) extends over a reasonably large energy range (0.52 eV) as can be seen from the deep well shaped curve of the minority spin band near the Fermi level. Thus, it can be assumed that even though the complex interface destroys the half-metallicity, the sample may transfer large spin-polarization into the semiconductor.

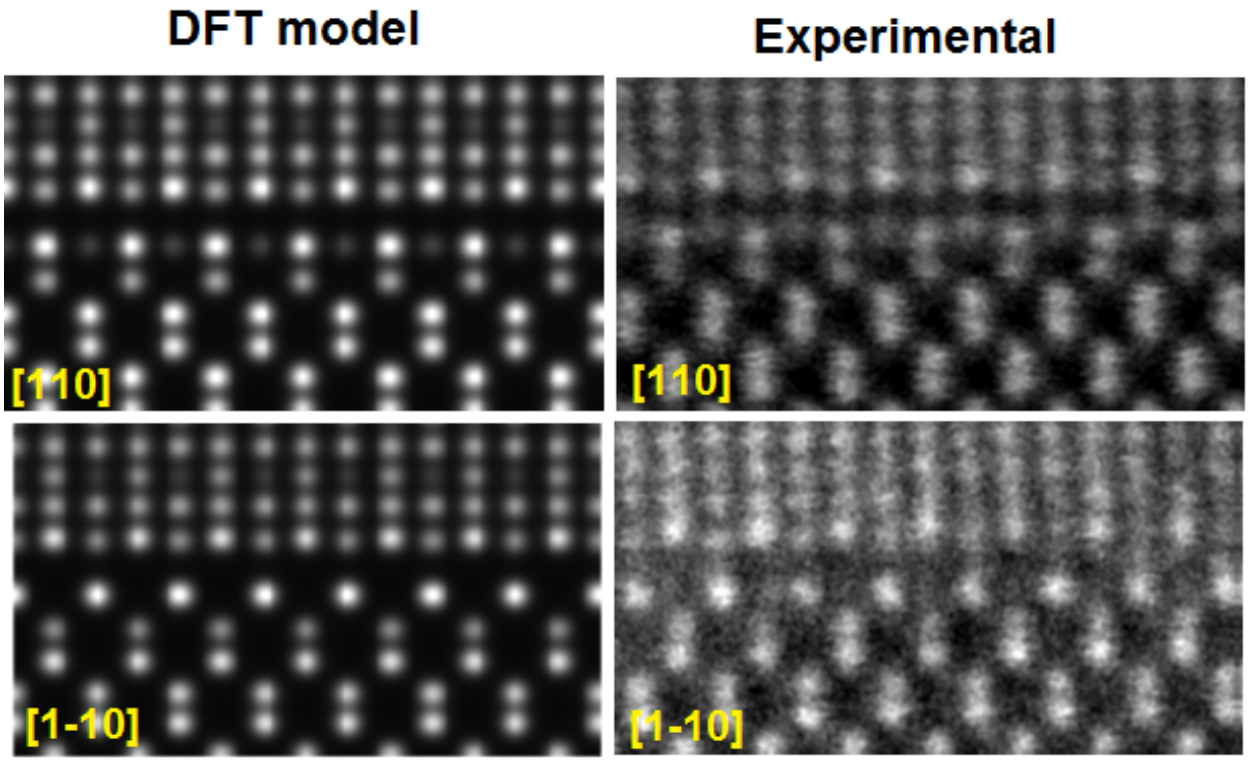

Figure 3.12: The QM-simulated STEM of the best-fit DFT model compared with the experimental STEM of the 0.5ML CMS/GaAs(001) sample with 0.5ML-flux MnSi initiation, observed from two orthogonal directions (top: [110] and bottom: [1-10]).

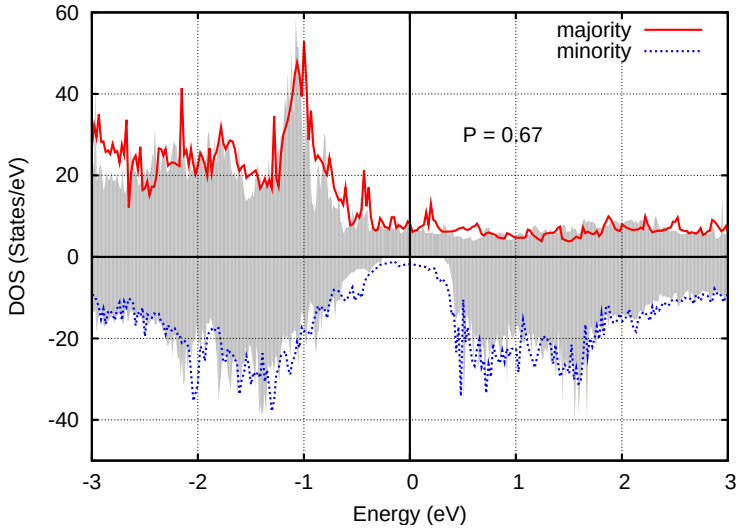

Figure 3.13: Total DOS of the best-fit DFT model for 0.5ML CMS/GaAs(001) with MnSi-initial flux. The total DOS of a theoretical CMS/GaAs(001) with an ideal abrupt SiMn/As termination is shown by the background grey portion.

In order to understand the origin of this destruction of half-metallicity, a closer inspection of the atom-projected DOS of the complex interface model is performed. Galanakis et. al. [75] have shown that in Co_2MnSi, the orbitals in the neighborhood of the bandgap are dominated by Co-d character. Hashemifar et. al. [77] have shown that for the ideal abrupt SiMn/As termination that retains half-metallicity, the band edges around the minority gap are dominated by orbitals of As-p character and of Mn-d character. In such a geometry of SiMn/As termination, the Co layer is screened from the As layer at the interface by a layer of MnSi at the ideal abrupt interface. In our best-fit model above, as shown in Fig. 3.11, a layer of Co atoms is right next to Int4 As ions. In fact, both Int4 As and Int3 Mn have Co as their nearest neighbors. We also have Si at Int1 with surface As being its nearest neighbor. Surface As is bonded to the substituted Mn below it. Figure 3.14 shows the spin-resolved Local Density of States (LDOS) of the three interface ions (Int1 - Si, Int3 - Mn, and Int4 - As) along with the LDOS of surface Co (above Int4), surface As, and the substituted Mn ions. For comparison, the LDOS of Si and As ions are multiplied by a factor of 6.

By investigating the LDOS of ions in Fig. 3.14, we can see that interface states, especially around the Fermi level, are dominant in substituted Mn and Int1 Si. The states around the conduction band edge of the minority band are dominated by the d character of Mn and Co as shown in Fig. 3.14(f) and (a), and the states around the valence band edge are dominated by the p character of As and Si as shown in Fig. 3.14(b), (d) and (e), and by Co-d character as in Fig. 3.14(a). The Co-d states, especially near the band gap for the minority band, are significantly different from Co states in bulk Co_2MnSi. The gap has become norrower and states appear very close to the Fermi energy. Also, the As p states have shifted to higher energies as shown in plots (b) and (e).

To understand how magnetism is affected locally, we investigate the atomic spin magnetic moments, in μ_B, of ions at the interface. Table 3.2 shows the atomic magnetic moments of the 6 ions listed in Fig. 3.14 along with the magnetic moments of the SiMn/As ideal abrupt pattern of CMS/GaAs, and bulk moments of components in Co_2MnSi for comparison.

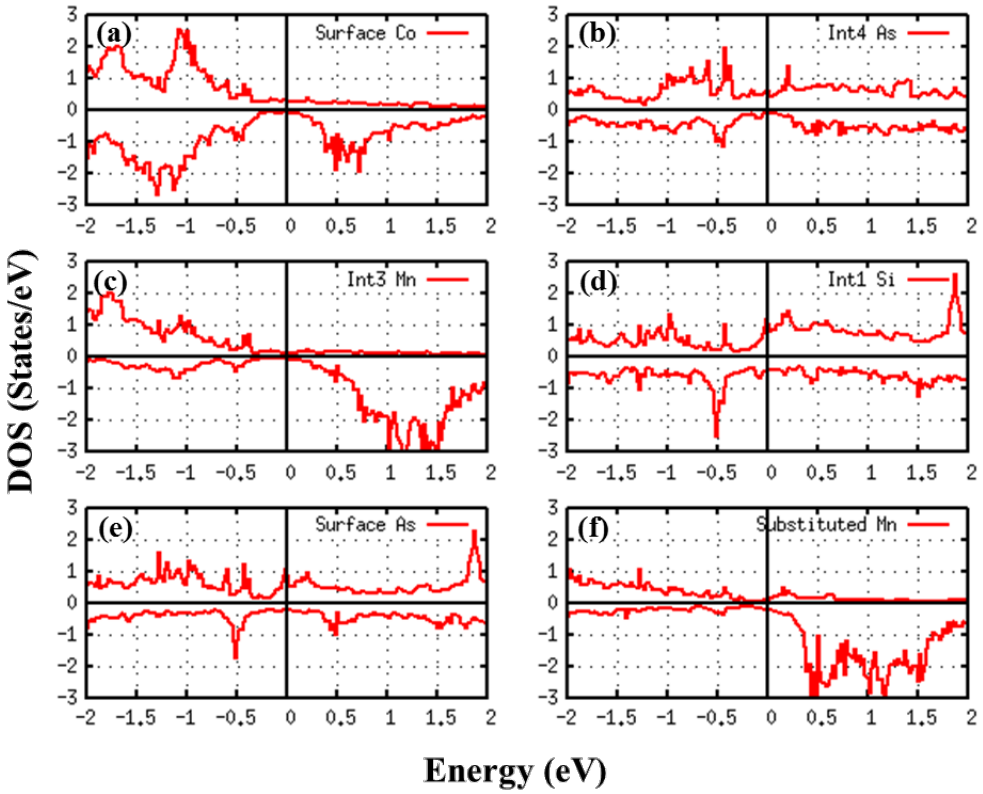

Figure 3.14: Atomic projected DOS of the interfacial atoms for the best-fit DFT model of 0.5ML CMS/GaAs(001) with MnSi-initial flux. LDOS of (a) Surface Co (layer above Int4), (b) Int4 - As, (c) Int3 - Mn, (d) Int1 - Si, (e) Surface As, and (f) Substituted Mn. The density of states of As p-states and Si p-states are multiplied by a factor of 6 for comparison.

Table 3.2: The atomic magnetic moments of the 6 ions listed in Fig. 3.14 along with the magnetic moments of SiMn/As ideal abrupt pattern of CMS/GaAs, and bulk moments in Co_2MnSi.

Model	Magnetic moment (μ_B)					
	Surface Co	Int4 As	Int3 Mn	Int1 Si	Surface As	Substituted Mn
Best-fit model	0.988	-0.018	3.692	-0.084	-0.031	3.738
	Co	Mn	Si	As		
SiMn/As interface	-	3.846	-0.034	-0.046		
Bulk Co_2MnSi	1.039	2.997	-0.040	-		

In the best-fit model, the spin moments of both Int3 Mn and substituted Mn are larger than that of Mn atoms in bulk Co_2MnSi. This can be attributed to the reduction of the number of nearest neighbors for Int3 Mn and substituted Mn, which has led to rehybridization of Mn-*d* states. This effect is shown in Fig. 3.15 in which the atom-resolved DOS of Int3 Mn (red curves) is shown along with that of a Mn ion in bulk-CMS (shaded portion in the background). There is also transfer of some minority electrons into the majority states, which is the reason for the increase in the magnetic moment in Int3 Mn. Interface 4 As, Int1 Si, and surface As are all antiferrmoagnetically coupled to the Mn ions at the interface. While the As ion moments in the best-fit model are reduced compared to SiMn/As interface, the Si moment is slightly increased.

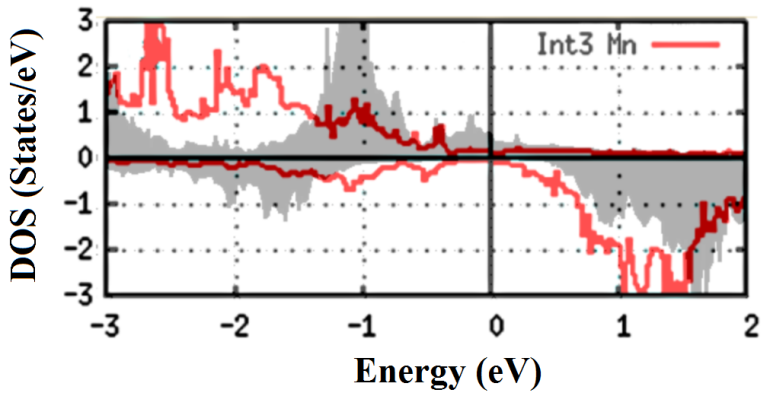

Figure 3.15: Atomic projected DOS of Int3 Mn (red curves) compared to that of Mn ions in bulk-CMS (shaded region).

From comparison of the experimental STEM with that of the QM-simulated STEM images of the DFT models, we can say with confidence that the physical structure of the complex interface as shown in Fig. 3.11 is the best-fit of the many models that we calculated. We can apply the same confidence to the chemical composition of the interface, except for two specific positions, namely Int1 and substitutional site (of Mn). The substitutional site with Mn (or with Ga) has relaxed to a similar metastable structure, for Int1 with Si or Mn. In this situation, it is useful to calculate the formation energy/atom for the different models with similar physical structure after relaxation. Table 3.3 shows the formation energy and the spin polarization at the Fermi level for four structures with

Table 3.3: Formation energy (ev/atom) and spin polarization (P) at the Fermi level for DFT models with physical structure similar to the best-fit DFT model.

Model	Interface composition	E_{form} (eV/atom)	P
Case90 (best-fit DFT)	Int1 - Si, substitional Mn	-0.118	0.67
Case91	Int1 - Mn, substitional Mn	-0.100	0.05
Case95	Int1 - Si, Ga (no Mn substitution)	0.066	0.27
Case96	Int1 - Co, Ga (no Mn substitution)	-0.002	0.36
Case97	Int1 - Mn, Ga (no Mn substitution)	-0.055	0.52

slightly different chemical composition. As shown in Table 3.3, for metastable DFT structures that are physically identical, case90 (best-fit DFT model) has the lowest formation energy/atom, E_{form}, and case91 with a slightly higher formation energy. The other model with reasonable formation energy/atom is case97.

3.3.2 Co_2MnSi/GaAs(001) with 1ML-flux

For the 1ML CMS/GaAs(001) case, there are more constraints on the possible interface structures due to the presence of chemical information at the interface in the form of EELS spectral mapping. For 1ML CMS/GaAs(001), there are 3 samples with different initial flux (MnSi, Mn, and Co) and for each of them, high-res STEM and EELS mapping were performed by Professor Voyles' group. The placement of Mn, Co, Ga, and As inside the interface is predicted with a certain level of confidence from the EELS spectral mapping, as shown in Fig. 3.10(c). Based on the analysis of STEM micrographs and EELS spectra, the interface pattern in MnSi- and Mn-initial flux samples look identical, and we could not tell definitively the presence, or absence thereof, of Si in the complex interface patterns. There is one vacancy site inside the complex interface structure in MnSi- and Mn-flux samples, where there is a possibility for Si to be present. To reproduce the interfacial pattern in MnSi- and Mn-initial flux samples, I modeled two supercells,

as shown in the schematic in Fig. 3.16 (Case1 no Si; Case2 Si in layer3), to calculate the metastable structure from *ab initio* DFT method. The results for these 2 cases along with the results of a DFT model for the Co-flux-initiated sample are discussed in this section.

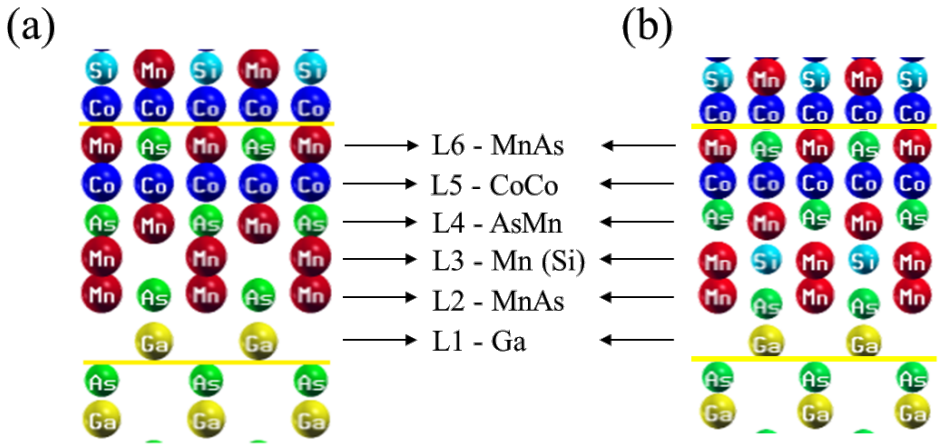

Figure 3.16: The DFT supercell schematic of the complex interface in 1ML CMS/-GaAs(001) samples with (a) Mn in layer L3 (Case 1) and (b) MnSi in layer L3 (Case 2). [shown in [110] planar view]

Case1 DFT model - Mn in layer L3

The ball-and-stick representation of the interface shown in Fig. 3.16(a) is constructed based on the scheme of atoms in the interface as measured from the EELS spectra. The interface layers are labeled from L1 to L6 in Fig. 3.16, along with the atomic composition in each interface layer. The difference between Case1 of the DFT supercell model and Case2 is the presence of Si in layer L3 in the vacancy site in the interface. In Case1, the interface is 6 layers thick, with Mn diffusing inside the GaAs surface, pushing As above, at least 3 layers into the CMS alloy. Based on the DFT-relaxed metastable structure of the interface in Case1, there is a MnGaAs-like structure in layers L1 and L2, with L2-Mn having L1-Ga as its nearest neighbor. While the L1-Ga atom and L2-As atom follow the zinc-blende pattern of GaAs, the bond-length between L1Ga–L2As is stretched by 20 pm, compared to their bond-length in bulk-GaAs (2.47 Å). Interface layers L2–L4 form a Mn_2As-like pattern. There is one layer of Co inside the complex interface (at L5) with a layer of MnAs above and below it (L6 and L4), forming a Co_2MnAs-like structure.

Figure 3.17 shows the comparison of actual STEM micrograph (middle panel) of 1ML CMS/GaAs(001) sample (with MnSi-initial flux) with QM-simulated STEM of the DFT-calculated metastable structure of Case1 (left panel). The ball-and-stick representation of the DFT-relaxed metastable structure (right panel) of Case1 is shown for clarity. The upper row [Fig. 3.17(a)] shows [110] planar view of the interface, and the lower row [Fig. 3.17(b)] shows [1-10] planar view of the interface. The colored circles in the experimental STEM represent the position of different ionic species, based on the EELS spectral mapping. As observed in the figure, the STEM micrograph of the DFT-relaxed interface model is in good agreement with the experimental STEM image.

The total DOS of the periodic supercell structure for Case1 is shown in Fig. 3.18, and it is compared with the DOS of CMS/GaAs(001) with an ideal abrupt SiMn/As termination (shaded portion of the plot). As expected for such a complex interface, a density of interface states appears at the Fermi level, E_{F}, for the minority band that destroys the half-metallicity of the bulk CMS, although the number of minority states at the Fermi level is much lower than the majority states, thus giving a high spin polarization of P = 0.6. There is a finite gap of 0.07 eV that is shifted to lower energy, and there is a well-shaped feature near this gap over a range of 0.68 eV for which the spin polarization remains larger than 0.59.

To better understand the source of the interface states, as observed in the total DOS plot above, the layer-by-layer DOS of the complex interface is plotted in Fig. 3.19. The major sources of interface states at the Fermi level for the minority spin bands are L2 - MnAs and L1 - Ga. Inspection of the individual atom-projected DOS of Mn-*d* character and the *s,p*-characters of Ga, and As suggest a strong hybridization between these orbitals. Unlike the hypothetical case of half-metallic CMS/GaAs(001) with ideal abrupt SiMn/As termination in which the last layer of Co in CMS is shielded from As by interfacial MnSi, in the Case1 DFT model, the Co layer at L5 is adjacent to As in both layers L4 and L6, with As at L4 being the nearest neighbor to Co at L5. As a result, Co hybridizes with As such that the minority *d* band of Co shifts to lower energy and also the Co band gap for the minority reduces.

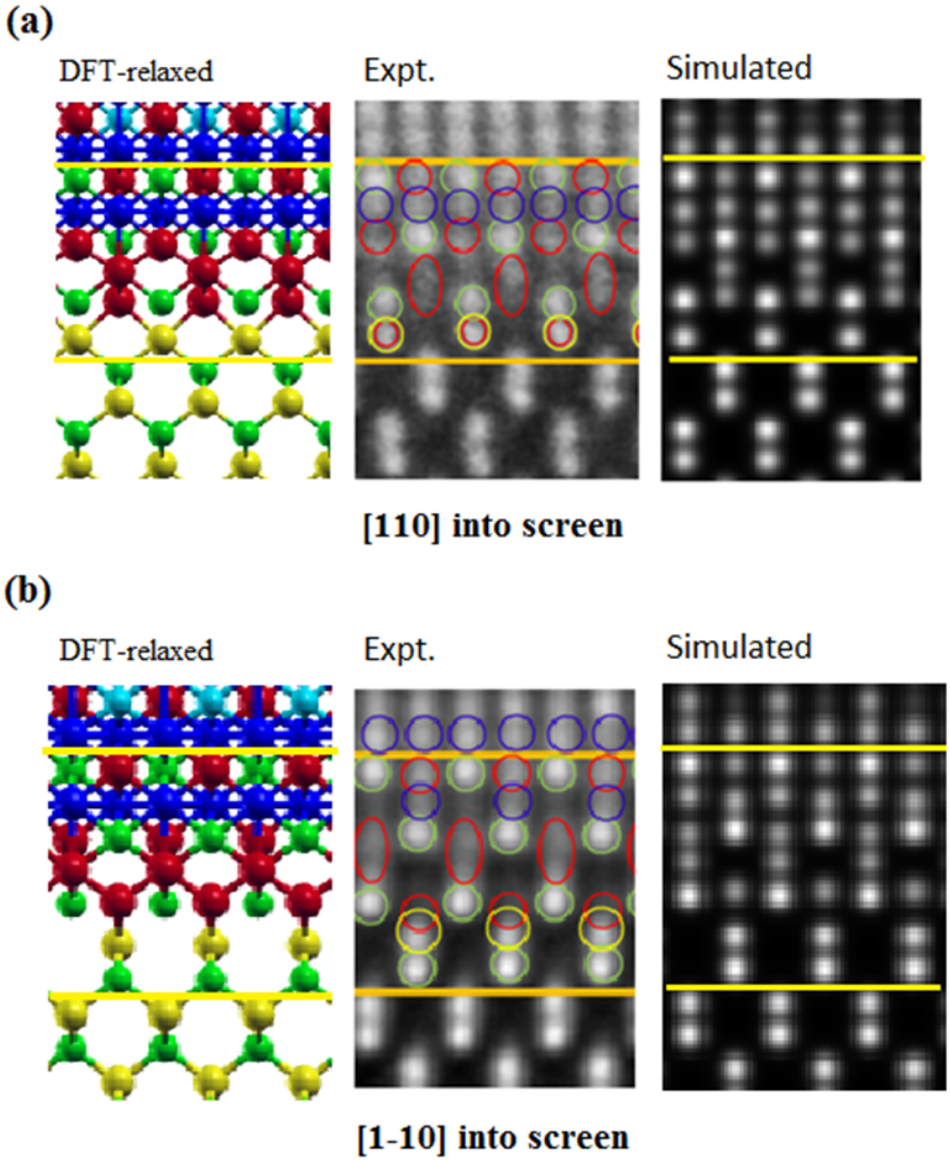

Figure 3.17: Ball-and-stick representation of the DFT-relaxed interface structure for Case 1 (left), the experimental STEM image (middle) of 1ML CMS/GaAs(001) with MnSi-initiated flux growth, and the QM-simulated STEM micrograph of the DFT-relaxed interface model for Case 1 (right), observed from two orthogonal planes (a) [110] into screen and (b) [1-10] into screen. The colored circles in the experimental STEM represent the position of different ionic species, based on the EELS spectral mapping. Color scheme: Co - blue, Mn - red, Si - turquois, As - green, and Ga - yellow.

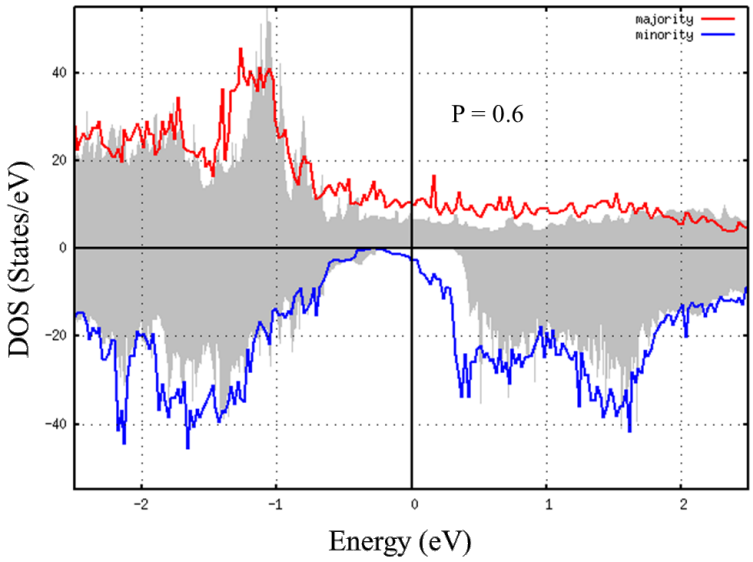

Figure 3.18: The total DOS for 1ML-CMS/GaAs(001) with MnSi-initiated flux. The total DOS for CMS/GaAs(001) with ideal abrupt SiMn/As termination is shown in the shaded portion.

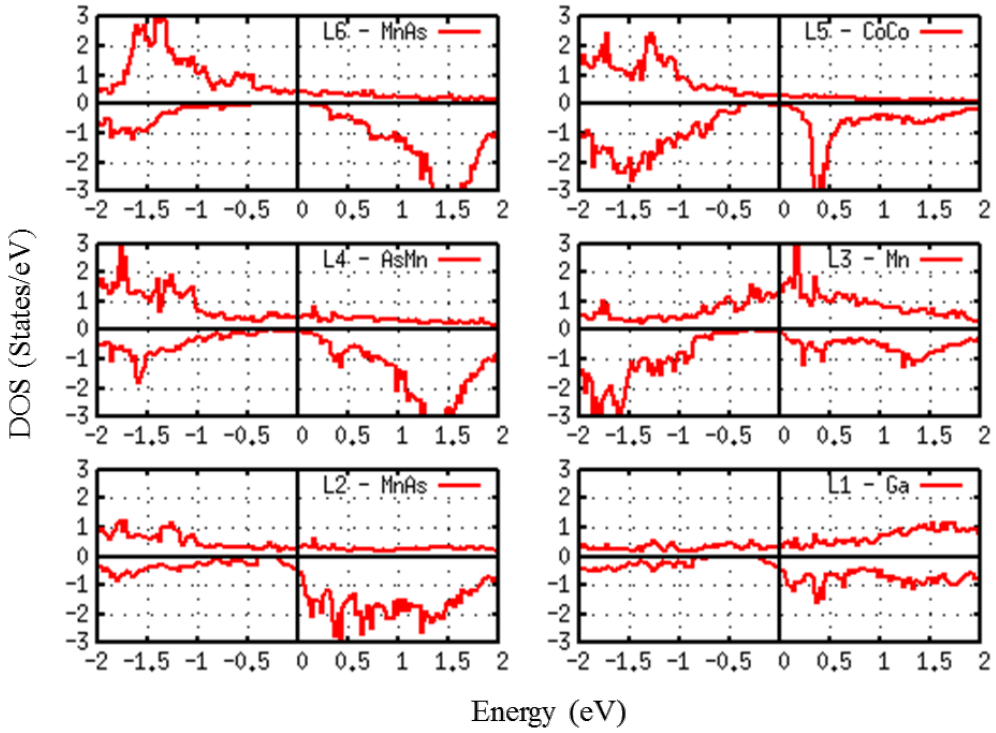

Figure 3.19: The layer-by-layer LDOS at the interface for Case1 DFT model for 1ML-CMS/GaAs(001). The DOS of L1-Ga are multiplied by a factor of 5 with respect to other panels for comparison.

For each atom at the interface, the spin polarization of only the (s,p)-character $P_{(s,p)}$, which is a more relevant quantity for transport properties, is listed along with the magnetic moment, $m(\mu_B)$, in Table 3.4. As shown by the spin polarization values of individual atoms at the interface, the major sources of the interface states are layers L1 and L2, and to an extent in layer L3. The magnetic moment of Mn atom in L2 is larger ($3.594\,\mu_B$) than that of Mn atom in bulk-CMS, which is $2.997\,\mu_B$. The moments of L1-Ga and L2-As are also significantly enhanced compared to bulk-GaAs. The magnetic moment of the Mn atom in L3 is anti-ferromagnetically aligned to the moments of MnAs in layers L4 and L2. The magnetic moments and the spin polarization in CoCo, and MnAs in layers L4 and L5 behave similar to those in bulk-Co_2MnAs, except for a small loss in spin polarization.

Table 3.4: The calculated (s,p)-character spin polarization, $P_{(s,p)}$, and the magnetic moment, $m(\mu_B)$, of atoms at the interface for Case1 DFT model.

Int. layer	$P_{(s,p)}$				Magnetic moment (μ_B)			
	Co	Mn	As	Ga	Co	Mn	As	Ga
L6		0.98	0.98			3.231	0.019	
L5	0.88 (0.93)				1.15 (1.01)			
L4		0.86	0.88			2.999	0.017	
L3		0.52				-0.936		
L2		0.24	-0.16			3.594	0.022	
L1				-0.11				0.028

Case2 - MnSi in layer L3

Figure 3.20 shows the comparison of actual STEM micrograph of 1ML CMS/GaAs(001) sample (with MnSi-initial flux) with the QM-simulated STEM of the DFT-calculated metastable structure of Case2 (MnSi in layer L3). The ball-and-stick representation of the DFT-relaxed metastable structure of Case2 is shown for clarity. A comparison of the QM-simulated STEM of the DFT-model for Case2 with the actual STEM micrograph of 1ML CMS/GaAs(001) sample with Mn-initial flux looks very similar to Fig. 3.20, since the interfacial structure for MnSi- and Mn-flux initiated samples looks similar from the corresponding STEM micrographs. The upper panel [Fig. 3.20(a)] shows [110] planar

view and the lower panel [Figure 3.20(b)] shows the [1-10] planar view. The colored circles in the experimental STEM represent the position of different ionic species, based on the EELS spectral mapping. As observed in the figure, the STEM micrograph of the DFT-relaxed interface model is in good agreement with the experimental STEM image. In the QM-simulated STEM of the DFT model for Case2, the signal for Si atoms in layer L3 is very weak compared to a relatively high-Z atom like As or Ga. Apart from Si in layer L3, the interfacial structure in Case2 is identical to that of Case1. The interface is 6 layers thick, with Mn diffusing inside the GaAs surface, pushing As above, at least 3 layers into the CMS alloy. As shown in Fig. 3.16(b), there is MnSi in layer L3. Unlike Case1, there is no Mn_2As-like interface pattern in layers 2–4 (L2–L4) in Case2, due to the presence of Si in layer L3. The Mn atom in L2 has Si in L3 as its nearest neighbor and Mn in L3 as its nearest neighbor. The Si atom in L3 has Mn in L4 as its next nearest neighbor. While the Ga atom in L1 and As atom in L2 follow the zinc-blende pattern of GaAs, the bond-length between L1Ga–L2As is stretched by 12 pm, compared to their bond-length in bulk-GaAs (2.44 Å). There is one layer of Co inside the complex interface (at L5) with a layer of MnAs above and below it (L6 and L4), forming a Co_2MnAs-like structure.

The total DOS of the periodic supercell structure for Case2 is shown in Fig. 3.21, and is compared with the DOS of CMS/GaAs(001) with ideal abrupt SiMn/As termination (shaded portion of the plot). The total DOS plot for Case2 looks very different from that of Case1, especially around the Fermi level, E_F, for the minority band. The spin-polarization value is higher (P = 0.77) compared to Case1, but there is no actual gap in the minority band in Case2. Also, away from E_F the number of states at the minority band increases drastically, with no well-shaped feature around E_F.

To better understand the source of the interface states, the layer-by-layer local DOS (LDOS) of the complex interface is plotted in Fig. 3.22. Interface states appear due to all but one layer (L6 - MnAs) in the interface structure. There is a complex hybridization due to the presence of Si in layer L3. The minority conduction band edge approaches the Fermi energy due to hybridization of Co *d*-states (L5) and As *s,p*-states (L4). The

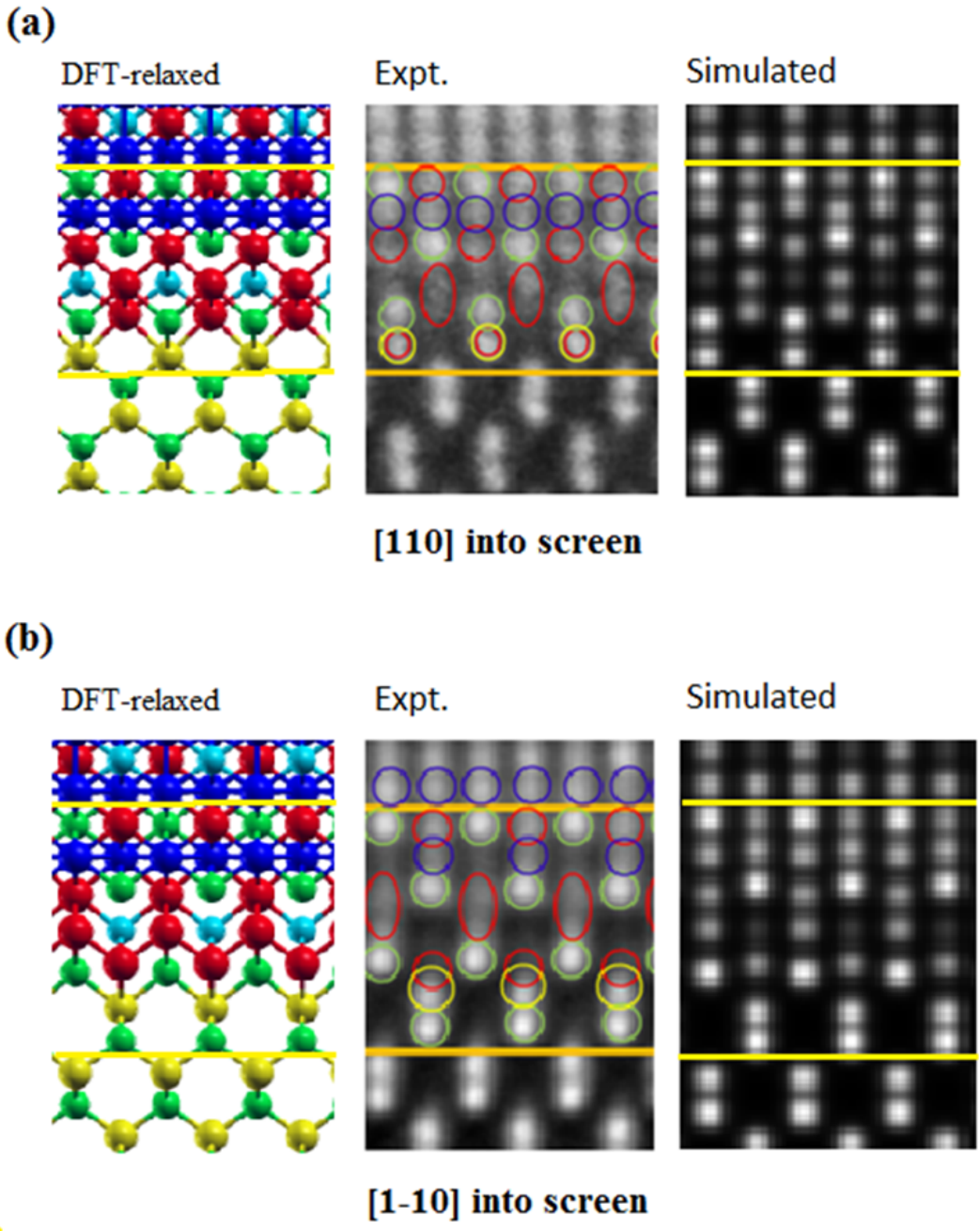

Figure 3.20: Ball-and-stick representation of the DFT-relaxed interface structure for Case2 (left), the experimental STEM image (middle) of 1ML CMS/GaAs(001) with MnSi-initiated flux growth, and the QM-simulated STEM micrograph of the DFT-relaxed interface model for Case 2 (right), observed from two orthogonal directions (a) [110] into screen and (b) [1-10] into screen. The colored circles in the experimental STEM represent the position of different ionic species, based on the EELS spectral mapping. Color scheme: Co blue, Mn red, Si turquois, As green, and Ga yellow.

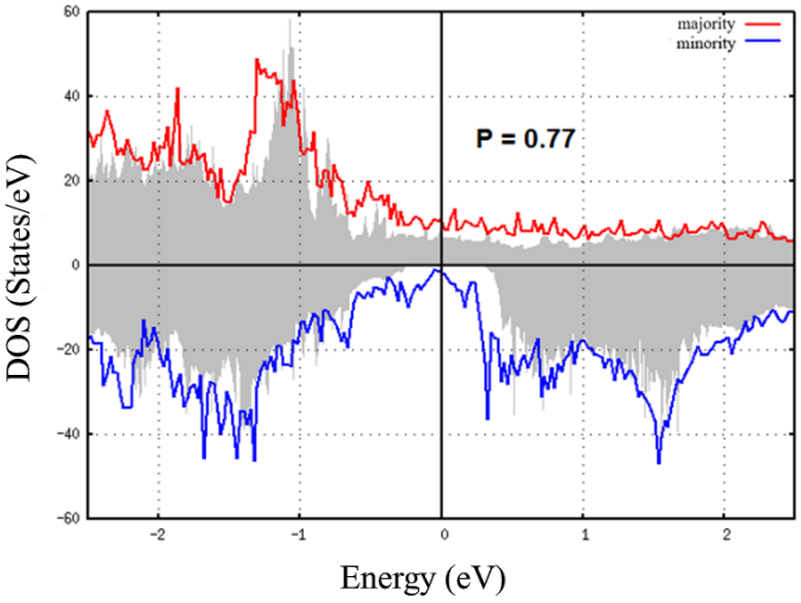

Figure 3.21: The total DOS of the periodic supercell structure for Case2 (MnSi in layer L3). The total DOS for CMS/GaAs(001) with ideal abrupt SiMn/As termination is shown in the shaded portion.

minority valence band edge is destroyed by hybridization of Mn d-states in L2 and Si s,p-states in L3. Further inspection of the atomic LDOS of Mn in L3, there seems to be a charge transfer from this Mn atom to Si in L3.

For each atom at the interface, the spin polarization of only the (s,p)-character ($P_{(s,p)}$), which is a more relevant quantity for transport properties, is listed along with the magnetic moment, $m(\mu_B)$, in Table 3.5. As shown by the spin polarization values of individual atoms at the interface, interfacial states appear in all layers of the complex interface structure, and the spin polarization value is particularly low for Si in L3 and for As in L2 and L4. A major difference in magnetic ordering in Case2 compared to that of Case1 is

Table 3.5: The calculated (s,p)-character spin polarization, ($P_{(s,p)}$), and the magnetic moment, $m(\mu_B$, of atoms at the interface for Case2 DFT model.

Int. layer	$P_{(s,p)}$				Magnetic moment (μ_B)			
	Co	Mn	As	Si	Co	Mn	As	Si
L6		0.85	0.91			3.165	0.017	
L5	0.74 (0.58)				1.07 (1.03)			
L4		0.5	0.38			2.842	-0.001	
L3		0.7		0.34		1.218		-0.11
L2		0.76	0.47			2.551	-0.01	

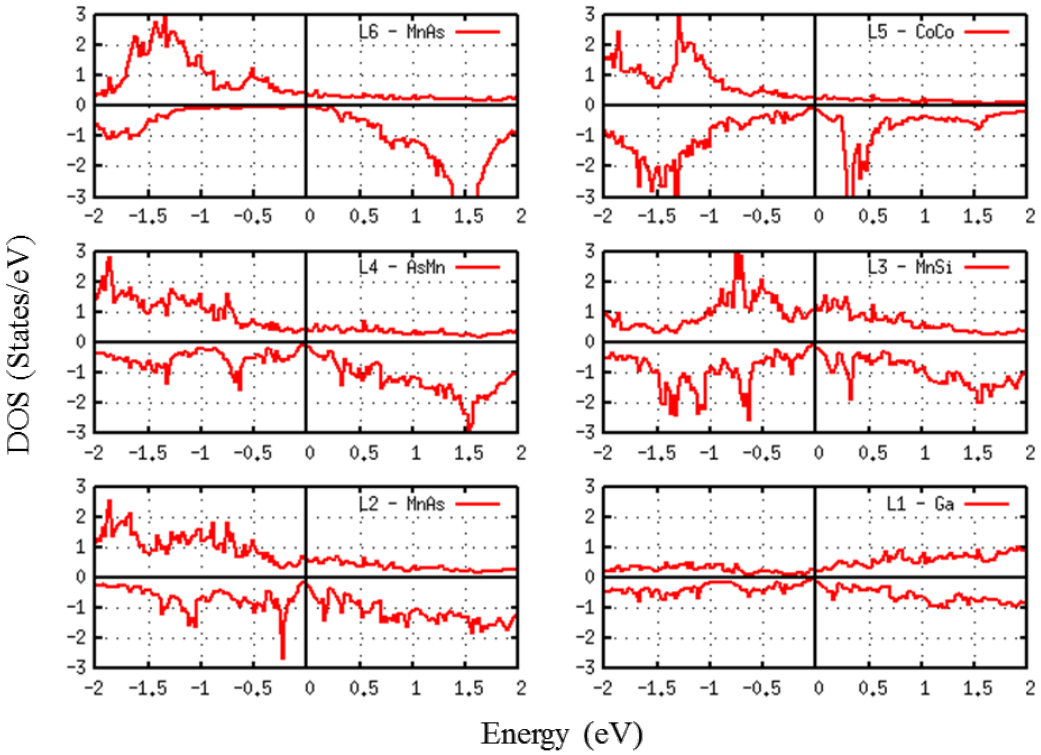

Figure 3.22: The layer-by-layer LDOS at the interface for Case2 (MnSi in layer L3). The LDOS plot of L1-Ga is multiplied by a factor of 5 for comparison.

the moment of Mn in L3. In Case1, Mn in L3 is anti-ferromagnetically ordered to the moments in layers L2 and L4, whereas for Case2, Mn in L3 has a positive moment of $1.218\,\mu_B$. The moment of Si in L3 has AFM ordering with a value of $-0.11\,\mu_B$.

For 1ML CMS/GaAs(001) samples with Co-initiated flux, named as Case3, the results of the total DOS, the formation energy/atom, and the spin polarization at the Fermi level are presented below and compared with the results of Case1 and Case2.

Figure 3.23 shows the total DOS for Case3 DFT model (Co-initial flux). In Case3 DFT model, the spin polarization at the Fermi level is reduced by the presence of interface states. The spin-polarization at E_F is P = 0.52. Unlike Case1, where there is an actual gap in the minority spin band, there is no gap in the total DOS in Case3.

The formation energy per atom and the spin polarization at the Fermi level for all the 3 cases in 1ML CMS/GaAs(001) are shown in Table 3.6. All three models agree well with the experimental STEM, and also with the schematic chemical composition at the interface as observed from the EELS spectral mapping. As shown in Table 3.6, all three

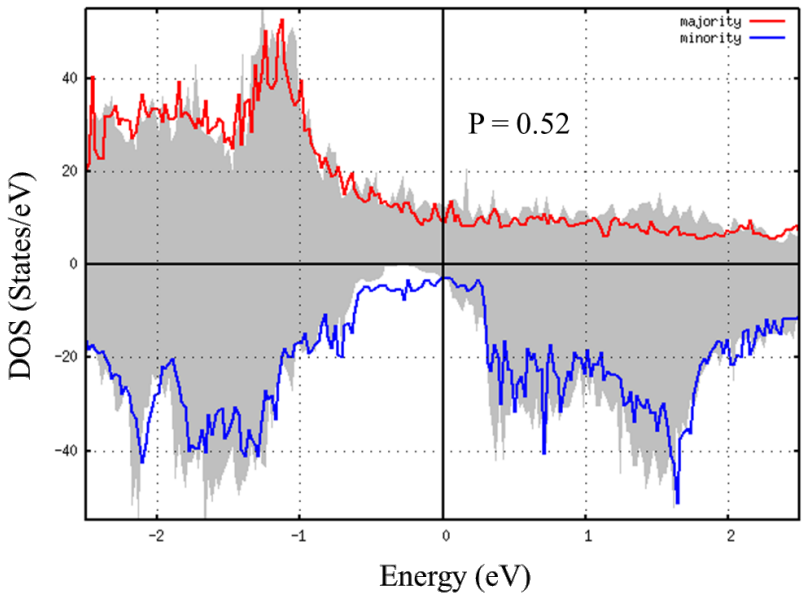

Figure 3.23: The total DOS of the DFT-model for 1ML-CMS/GaAs(001) with Co-initiated flux (Case3). The total DOS for Case1 DFT model is shown in the shaded portion, for comparison.

Table 3.6: Formation energy (ev/atom) and spin polarization (P) at the Fermi level for the DFT models for 1ML CMS/GaAs(001).

Model	Initiation	E_{form} (eV/atom)	P
1ML CMS/GaAs(001)	Case1 Mn in layer L3	-0.272	0.6
	Case2 MnSi in layer L3	-0.213	0.77
	Case3 Co-initiation	-0.299	0.52

DFT models have relatively low formation energy per atom, implying that the schematic structures based on the EELS spectrum is quite reliable.

3.4 Conclusion

For a 0.5ML CMS/GaAs(001) sample with MnSi-initiated flux, based on a predictive DFT modeling approach, we decoded the physical, chemical, electronic, and magnetic structure of the complex interface observed at the heterojunction. The model interface agrees well with the sample interface as observed by STEM micrographs. From *ab initio* DFT calculations, we find that the complex interface model has low formation energy/atom, and from the DOS of the periodic supercell that models the interface, we find that the complex interface destroys the half-metallicity of the bulk CMS, but the spin polarization at the Fermi level is still very high (P = 0.67). For 1ML CMS/GaAs(001) samples with MnSi-, Mn-, and Co-initiated flux, we follow the schematic chemical composition, based on EELS spectral mapping at the complex interface, to model the complex interface for *ab initio* DFT calculations. The agreement between the DFT modeled interfaces and the experimental STEM micrographs of the samples is quite good. The formation energy/atom for all three DFT models are relatively low, implying that the chemical scheme based on the EELS spectrum is quite reliable. The DOS of Case1 DFT model is promising, with high spin polarization at the Fermi level (P = 0.6) and a well-shaped region around the Fermi level for the minority band for a range of 0.68 eV for which the spin polarization remains larger than 0.59. The physical and chemical structure of this model is in good agreement with the STEM and EELS spectra of both Mn- and MnSi-initial flux 1ML CMS/GaAs samples.

CHAPTER 4

HALF-METAL HALF-HEUSLER/GaAs(110) HETEROSTRUCTURES FOR EFFICIENT SPIN INJECTION

In this chapter, the electronic structure, magnetism, and structural stability of 6 half-metal half-Heusler/GaAs heterostructures in (110) layering (CoMnAs-, CoVAs-, FeVGe-, NiMnAs-, RhFeGe-, and RhMnP with GaAs) are investigated using ab initio density functional theory simulations, with the aim of identifying possible interface morphologies that preserve the peculiar half-metallic character of the constituent Heusler alloy. Among these, 4 heterostructures (NiMnAs,) with energetically stable interfacial geometries are identified to preserve the half-metallic character.

4.1 Introduction

Generation of a non-equilibrium spin population in a semiconducting channel is crucial for the efficient functioning of spintronic devices [97, 98]. While there are many ways of generating spin polarization, traditionally this has been achieved by using optical transitions or electrical injection techniques. Generally, for device applications electrical spin injection is more desirable [14, 99]. Half-metals are promising candidates as sources for electrical spin injection due to their 100% spin polarization. Half-metal Heusler alloys have a particularly prominent place in spintronics as many of them have high Curie temperature, and good lattice matching with a number of widely used semiconductors [99]. The central challenge in electrical spin injection is that the half-metallicity should be preserved at the interface between the spin source and channel [100]. Detailed first principle calculations have been performed to investigate the interfacial properties of many half metals, and it was found that most of the time the helf-metallic character is lost

at the interfaces [100, 101, 102, 103]. But a few promising theoretical interfaces in (001) layering have been found that preserve the half-metallicity at the interface [76, 104, 105]. Particularly in (110) layering, Nagao et. al. [106] have studied a theoretical interface between several full Heusler alloys and GaAs, and have found at least one interface pattern of Co_2CrAl/GaAs and one of Co_2MnSi/GaAs that preserve the half-metallic characteristic of the bulk Heusler alloy.

In the case of GaAs(110) quantum wells, electric field will be absent in the z-direction due to crystallographic and structural symmetry along the z-axis. Hence, the spin–orbit generated magnetic field will be aligned in the z-direction. If the spin of the incoming electron is in the z-direction, then there will be no precession of the spin. This is the basis of D'yakonov–Perel' spin relaxation. Ohno et. al. experimentally measured the spin relaxation times in GaAs quantum wells [63] and showed that spin relaxation time is an order of magnitude larger for (110) GaAs quantum wells compared to that of (100) quantum wells.

Recently, Butler et. al. published an extensive Heusler databsae [44] that provide results of *ab initio* calculations of three families of Heusler alloys, namely, full Heuslers (A_2BC), half Heuslers (ABC), and inverse Heuslers (ABAC). Based on density functional theory calculations, they found tens of half-Heusler alloys to posses the peculiar half-metallic character, with low formation energy/atom. I performed first-principles calculations on 6 half-metal half-Heusler alloys from this database (CoMnAs, CoVAs, FeVGe, NiMnAs, RhFeGe, and RhMnP) that have good lattice matching with GaAs, to explore the electronic and magnetic structure, and stability at the interface between half-metal half-Heusler/GaAs heterostructures in (110) layering.

4.2 Methods

4.2.1 Half-metal half-Heusler characteristics

A brief discussion here outlines the rationale for choosing the above 6 half-Heusler alloys from a large pool of half Heuslers that were determined to be half metallic. The foremost aspect is that the compounds should be half-metallic with reasonably large

bandgap around the Fermi level for minority bands, and are stable compounds with large formation energies. Second, the half-metal alloys should posses high M_s such that they will have high Curie temperature, T_C [107]. For successful layering with GaAs over large areas without dislocations and other imperfections, it is essential that the half-Heusler lattice constant match closely with the experimental lattice constant of GaAs ($a_{exp} = 5.65\,\text{Å}$). Finally, half-Heuslers with Cr and Ni as components are avoided in our calculations as they are prone to diffuse easily into GaAs during MBE growth, with the exception of NiMnAs as it is a half-metal half-Heusler alloy with one of the largest calculated M_s (828.55 emu/cc) and its lattice matches closely with GaAs. Figure 4.1 shows the lattice constant, a(Å), of the six half-Heusler alloys choices based on the proximity with GaAs, and compares the percentage change in lattice constant of the Heusler alloys with GaAs. GaAs is included in the plot for comparison.

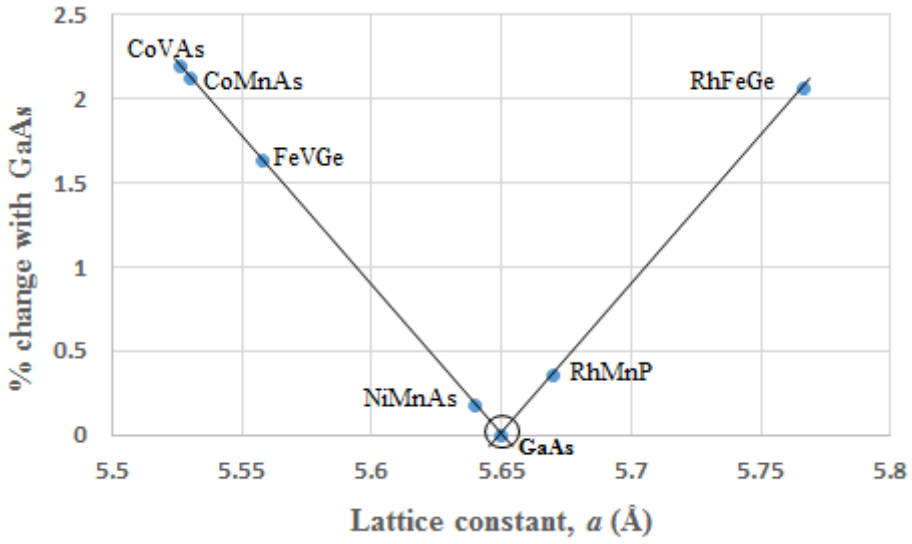

Figure 4.1: Percentage change in lattice constant with GaAs, plotted as a function of the lattice parameter, a(Å), for the 6 half-metal half-Heusler alloys chosen in this study. GaAs is added as a data point for comparison.

Table 4.1 shows the consequential properties of the 6 half-metal half-Heusler alloys used in our calculations, that are reported in the Heusler database. For all the above half-Heusler alloys, the formation energy/atom as reported in the Heusler database is relatively high ($< -0.125\,\text{eV}$). The alloys NiMnAs, CoMnAs, RhMnP, and RhFeGe have high saturation magnetization. The properties of CoMnAs, NiMnAs, and RhMnP

Table 4.1: Magnetic moment in units of Bohr magneton (μ_B), saturation magnetization, M_s, in (emu/cc), Curie temperature in K as reported in literature, and the calculated bandgap around the Fermi level for minority band in eV, for the 6 half-metal half-Heusler alloys used in this study.

Heusler alloy	Magnetic moment (μ_B)	M_s (emu/cc)	Curie temp. (K)	Gap width (eV)
CoVAs	1	220.05	-	1.25
CoMnAs[a]	3	658.07	-	1.21
FeVGe	-1	215.58	-	0.78
NiMnAs	4	828.55	840[b]	0.72
RhMnP	3	611.60	401[c]	0.9
RhFeGe	3	575.19	-	0.46

[a]Reported in literature to be stable [108].
[b]Ref. [109].
[c]Ref. [110].

have been studied theoretically and reported in literature, with Curie temperature values reported for NiMnAs and RhMnP [109, 110]. Except for RhFeGe, all other half Heuslers in this table have very large calculated bandgap ($> 0.7\,\text{eV}$). NiMnAs has one of the largest values of magnetic moment/f.u. of the half-Heusler alloys and a very large Curie temperature.

4.2.2 Interface modeling

Figure 4.2 shows the cubic unit cell of (a) a half-Heusler alloy ABC, with $C1_b$ crystal structure and (b) GaAs with zinc-blende crystal structure. The [110] lattice plane is represented by the pink sheet slicing the cubic unit cell. Figure 4.2(c) shows the unit cell and the atomic arrangement in [110] layering for the half-Heusler ABC, and (d) for GaAs. As shown in Fig. 4.2(c) and (d), a unitcell in the [110] plane is stoichiometric for both the half-Heusler and for GaAs, meaning only one unit of the representative atoms in the chemical formula is present in this unit cell.

Based on symmetry considerations, there are at least 24 different ways to geometrically arrange a layer of half-Heusler ABC one top of a layer of GaAs in the [110] direction; (i) either one or two of the atoms of a half-Heusler alloy (A, B, or C) can be placed directly on top of As and Ga ions in a unit cell in [110] layering, (ii) atoms of the half-Heusler can occupy a bridge site in between two As atoms (and/or two Ga atoms), and

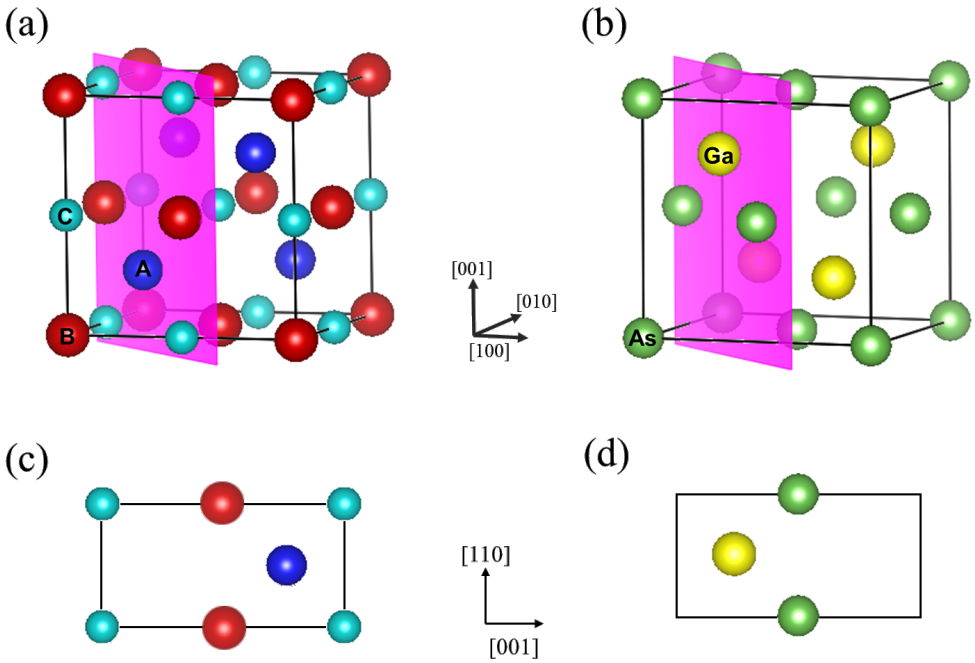

Figure 4.2: The cubic unit cell of (a) half-Heusler ABC with $C1_b$ crystal structure and (b) GaAs with zinc-blende crystal structure. The [110] lattice plane is represented by the pink screen slicing the cubic unit cell. Top view of atomic arrangement in [110] layering for (c) half-Heusler ABC, and (d) GaAs.

(iii) atoms of the half-Heusler can occupy hollow sites above the GaAs unit cell. For each of the 6 Heusler alloys, supercells modeling ideal abrupt interfaces between the half-Heusler alloy and GaAs based on the above mentioned geometrical arrangements were energetically relaxed using DFT calculations. We study the electronic and magnetic structure of the periodic supercells which include these interfaces for those geometries that are energetically more stable.

4.2.3 Computational details

The central features of the computation are explained in Section 2.2. For half-Heusler/GaAs heterostructures in (110) layering, the superlattices are tetragonal unit cells with rectangular bases. The in-plane lattice parameter of the cell is set to the experimental lattice constant of GaAs, such that $a = a_{exp}$ and $b = a_{exp}/\sqrt{2}$, where $a_{exp} = 5.65\,\text{Å}$. The periodic supercell has 10 layers of GaAs and 8 layers of the half-Heusler alloy (ABC), with identical interfaces at both sides of the junction. A large cut-off energy of 320 eV was chosen for the plane wave basis set. The integration in

the irreducible wedge of the supercell Brillouin zone was performed using a (10, 7, 1) k-point mesh according to the Monkhorst–Pack scheme [96], resulting in 24-k-points in the irreducible zone. An energy change of 1×10^{-6} eV was used as the stopping criterion for structural optimization, to reduce forces between ions in all degrees of freedom to less than 0.01 eV/Å. For integration cut-off at the Fermi energy, the Methfessel–Paxton method with smearing width of 0.2 eV was used.

4.3 Results

For the 6 half-metal half-Heusler alloys mentioned in Table 4.1, out of the many interfacial patterns with GaAs in (110) layering, there are three patterns as shown in Fig. 4.3 that are energetically very stable. Among these, pattern I is the most stable

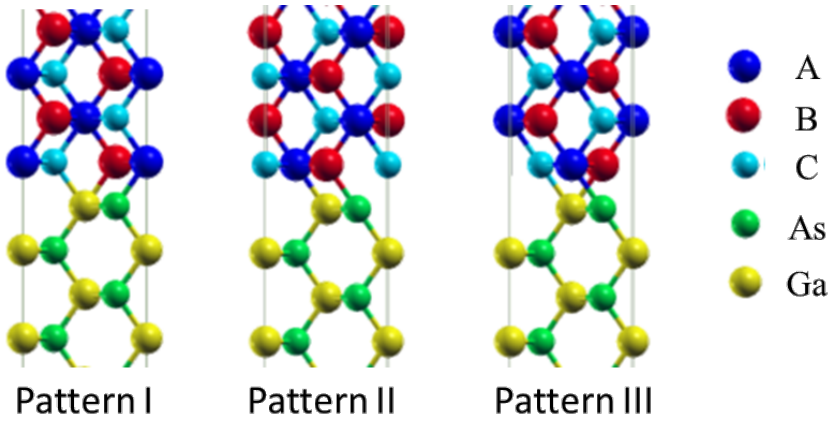

Figure 4.3: Ideal abrupt interface patterns between half-Heusler/GaAs(110) that are energetically very stable.

pattern for all the 6 Heusler alloys, and pattern II is the second most stable pattern for CoVAs, CoMnAs, NiMnAs, and RhFeGe. For FeVGe and RhMnP, pattern III is the second most stable interfacial pattern. In pattern I, at the interface, the B atom of the half-Heusler (B = Mn, Fe, V) is in a bridge site above As, and the A atom (A = Co, Ni, Fe, Rh) occupies the corner of the rectangular lattice. In pattern II, the B atom (for CoVAs, CoMnAs, NiMnAs, and RhFeGe) occupies the bridge site above Ga ions, and the C atoms occupy the corner of the rectangular lattice. In pattern III, the B atom (for FeVGe and RhMnP) occupies the bridge site above As, and the A atom occupies

the bridge site above Ga. In all interface patterns, a notable feature after relaxation is that the As ion at the interface in GaAs reconstructs in such a way that As goes slightly above Ga ($\sim 20\,\mathrm{pm}$).

Table 4.2 lists the electronic properties, relevant for spintronics, calculated for the two most stable interface patterns in all the 6 half-Heusler/GaAs(110) systems. The formation energies are presented by using the energy of the most stable interface pattern as the reference energy. The spin polarization at the Fermi level is denoted as P. The width of the band gap in the minority band is given as gap width in units of eV. Distance reported in eV is the distance from E_f to the nearest band edge in minority channel. It is important to measure this quantity since for a few structures, even though there is a large band gap, the edge of the gap is very close to E_f, thus making the interface spin sensitive to small thermal fluctuations. If the Fermi level is inside the bandgap, then the interface pattern is considered to preserve the half-metallic (HM) character of the half-metallic half-Hesuler alloy.

For all the 6 Heusler/GaAs systems, the most stable interface pattern is more stable than the second-most stable pattern by hundreds of milli electron volts. The most stable interface pattern in CoVAs-, NiMnAs-, and RhFeGe/GaAs(110) preserves the half metallicity at the interface. Though the band edge is closer to E_f in all 3 cases ($< 65\,\mathrm{meV}$), there is a deep well-shaped feature centered around E_f in all three cases, for which the spin polarization remains very high (> 0.9) [not shown in Table 4.2]. In the most stable interface pattern (pattern I) in CoMnAs/GaAs(110) and RhMnP/GaAs(110), interface states appear at E_f that destroy the half-metallicity, although spin polarization is still high (P = 0.9 for CoMnAs, and P = 0.82 for RhMnP). In FeVGe/GaAs(110), there is no band gap in the minority channel for either interface pattern. In all the above models, except FeVGe, the second-most stable interface pattern has a wider band gap and the electronic structure is always half-metallic at the interface.

For the 3 half-Heusler alloys, which preserve the half-metallicity at the interface with GaAs(110) (pattern I of CoVAs, NiMnAs, and RhFeGe), Fig. 4.4 shows the spin-resolved local density of electronic states (LDOS) for ABC atoms of the corresponding half-Heusler

Table 4.2: Energy stability and spintronics relevant electronic properties for 6 half-Heusler/GaAs(110) interfaces. E_{form} is the formation energy in eV, calculated by using the energy of the most stable interface pattern as the reference energy, P is the spin polarization, distance in eV is the nearest distance from E_{f} to a band edge. HM - half-metallic.

Alloy	Interface pattern	E_{form} (eV)	P	Gap width (eV)	Distance (eV)	HM
CoVAs	I	0.000	1	0.471	0.042	Yes
	II	0.839	1	0.861	0.022	Yes
CoMnAs	I	0.000	0.9	0.337	0.169	No
	II	0.759	1	0.799	0.301	Yes
FeVGe	I	0.000	-	No gap	-	No
	II	0.439	-	No gap	-	No
NiMnAs	I	0.000	1	0.259	@E_{f}	Yes
	II	0.719	1	0.645	0.307	Yes
RhMnP	I	0.000	0.82	0.246	0.168	No
	II	0.856	1	0.466	0.202	Yes
RhFeGe	I	0.000	1	0.282	0.065	Yes
	II	0.276	1	0.362	0.171	Yes

alloys at the interface. The LDOS of C atom (C = As and Ge) are multiplied by a factor of 10 for comparison. In NiMnAs/GaAs(110) [middle panel], interface states begin to

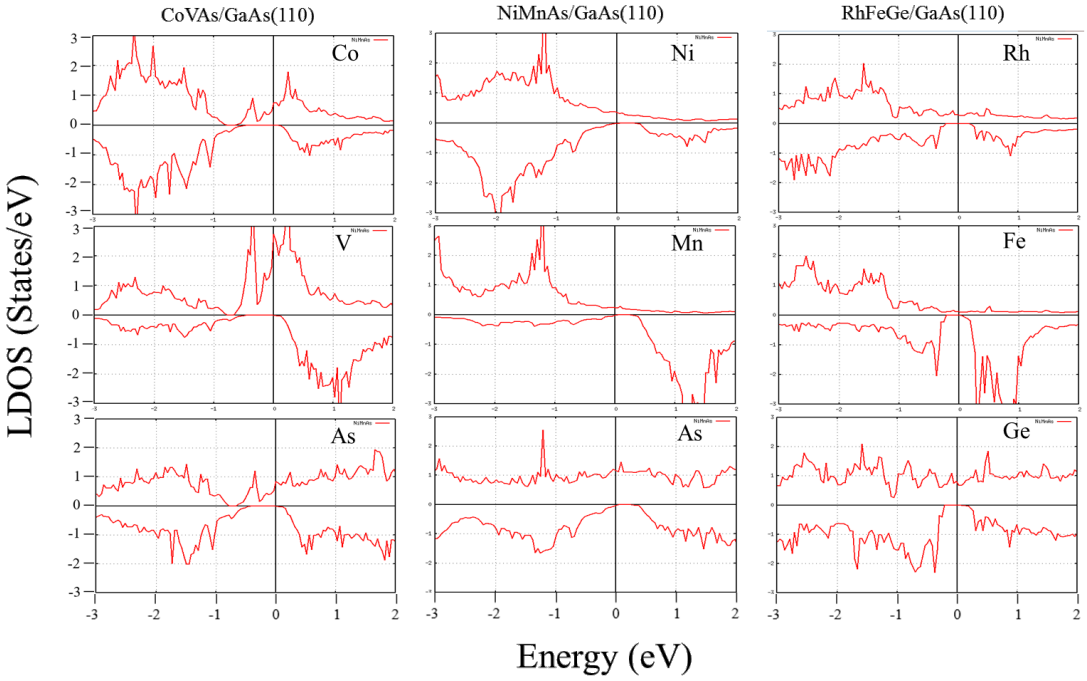

Figure 4.4: LDOS at half-Heusler interface with pattern I (most stable) for CoVAs/-GaAs(110) [left panel], NiMnAs/GaAs(110) [middle panel], and RhFeGe/GaAs(110) [right panel]. The LDOS of C atom (C = As and Ge) is multiplied by a factor of 10 for comparison.

appear just below the Fermi level for all three atoms (Ni, Mn, and As) at the interface. In RhFeGe/GaAs(110) [right panel], for the LDOS of Rh, the bandgap extends to $> 0.2\,\text{eV}$ on both sides of the Fermi level, whereas for Fe, interface states begin to appear right after E_f. In CoVAs/GaAs(110), interface states begin to appear immediately after E_f for the LDOS of V and As, whereas for Co, the band gap extends upto $0.1\,\text{eV}$ into the conduction band. For LDOS of V, the majority band has a sharp peak at the Fermi level, resembling localized *d*-character.

To avoid the influence of localized states, we investigated the spin polarization of interfacial atoms in CoVAs/GaAs(110) without *d*-components on the assumption that the non-*d* components of the DOS may be more important for transport than the more localized d-states. Without *d*-components, the spin polarization P is 1 for all component

atoms (Co, V, As, and Ga) from the interface to the bulk of CoVAs and GaAs, suggesting the spin polarization is relevant for spin transport.

Table 4.3 lists the magnetic moments in μ_B for individual atoms at the interface and in the bulk region for half-Heusler alloys (CoVAs, NiMnAs, RhFeGe – pattern I) layered with GaAs(110), that preserve the half-metallicity at the interface. In all 3 cases, the magnitude of magnetic moment of the A atom (Co, Ni, and Rh) and the C atom (As and Ge) of the half-Heusler reduces at the interface, while the moment of the B atom (V, Mn, and Fe) increases at the interface with respect to that of the bulk. The magnetic moment of surface Ga and As atoms of GaAs increases slightly at the interface.

Table 4.3: Magnetic moments in μ_B for individual atoms at the interface and in the bulk region for half-Heusler/GaAs(110) systems (pattern I) that preserve the half-metallicity at the interface.

System	Magnetic moment (μ_B)				
	Co	V	As	Ga	As
CoVAs/GaAs(110)	-0.126	1.452	-0.015	0.005	0.006
Bulk	-0.176	1.283	-0.031	0.003	0.002
	Ni	Mn	As	Ga	As
NiMnAs/GaAs(110)	0.223	3.633	-0.044	0.01	0.002
Bulk	0.296	3.604	-0.05	0.001	0.001
	Rh	Fe	Ge	Ga	As
RhFeGe/GaAs(110)	0.163	2.897	-0.057	0.013	0.015
Bulk	0.179	2.854	-0.077	0.001	0.001

4.4 Conclusions

In summary, we have investigated the structural, electronic, and magnetic properties at the interface for 6 half-metal half-heusler alloys having ideal abrupt interface with GaAs(110) using first principles calculations. Our results show that 3 systems [CoVAs/GaAs(110), NiMnAs/GaAs(110), and RhFeGe/GaAs(110)] preserve the half-metallic character at the interface for the most stable interface pattern. Two other systems [CoMnAs/GaAs(110) and RhMnP/GaAs(110)] posses very high spin polarization at the

interface. The spin polarization at the interface remains unchanged even if localized *d*-components are eliminated, suggesting that the half-metallic character may be reflected in transport properties.

CHAPTER 5

SEMICONDUCTING HALF-HEUSLER ALLOYS AS SPACERS BETWEEN Co_2MnSi/GaAs(110)

The structural, electronic, and magnetic properties of Co_2MnSi*/(half-Heusler-semiconductor-spacer)/GaAs(110) systems are investigated using ab initio density functional theory calculations, with CoTiAs and CoTiSb as the semiconducting spacers. It is found that insertion of CoTiAs as spacer preserves the half-metallic character of CMS through the CMS/CoTiAs/GaAs(110) heterojunction, for the most stable heterojunction between the three alloys. Furthermore, increasing the thickness of CoTiAs spacer layer significantly improves the bandgap- and perpendicular magnetic anisotropy (PMA) characteristics of the system, making it a promising candidate for PMA-based devices.*

5.1 Introduction

Even though half-metal Heusler alloys, believed to be completely spin polarized, are promising candidates for spintronic applications, the majority of spin-injection experiments from Heusler electrodes into semiconductors (SC) have shown relatively low efficiency, sometimes even lower than elemental ferromagnet/SC counterparts [23, 27, 99, 111, 112]. Among the various causes for the underperformance of Heusler/SC, are important materials challenges arising from atomic disorder, in-diffusion of magnetic impurities into the semiconductor, and formation of multiple phases between the Heusler and the compound semiconductor [82, 113, 114, 115, 116]. Farshchi and Ramsteiner have proposed insertion of an MgO tunnel barrier at the Heusler/SC interface to reduce in-diffusion [99]. Munira et. al. have shown from theoretical calculations that it is possible to induce perpendicular magnetic anisotropy (PMA) at the junction between Heusler/MgO, while

retaining half-metallicity at the interface [46]. A number of Heusler alloys have been successfully integrated with Al-O barriers to make magnetic tunnel junctions (MTJs) in (001) and (110) layering [52, 117, 118].

In this study, we model half-Heusler semiconductors as spacer layers between Co_2MnSi (CMS) and GaAs(110) and investigate, within the framework of density functional theory, the electronic and magnetic properties of the heterojunction. We also calculate the magnetic anisotropy to understand the nature of anisotropy (in-plane or perpendicular) in these systems. CoTiAs and CoTiSb are the two half-Heuslers we chose from the Heusler alloy database [44]. Table 5.1 lists some essential properties of the two half-Heusler semiconductors.

Table 5.1: The calculated lattice constant, a_{calc} in Å, percentage change of a_{calc} with GaAs, formation energy/atom in eV, semiconducting bandgap (eV), and the gap type for CoTiAs and CoTiSb.

Half-Heusler	a_{calc} (Å)	% change with GaAs	E_{form} (eV)	Bandgap (eV)	Gap type
CoTiAs	5.61	0.71	-0.852	1.29	Direct
CoTiSb	5.88	4.07	-0.670	1.06	Direct

5.2 Methods

We performed *ab initio* density functional theory calculations for CMS/GaAs(110) with either CoTiAs or CoTiSb as a spacer layer between CMS and GaAs in the heterostructure. Figure 5.1 shows the atomic arrangement in a (110) layering for (a) a full-Heusler with X_2YZ chemical formula and an $L2_1$ crystal structure, (b) a half-Heusler with XYZ chemical formula and $C1_b$ crystal structure, and (c) GaAs with zinc-blende crystal structure. There are many ways to arrange a half-Heusler on top of a compound semiconductor like GaAs, and many ways to arrange a full-Heusler alloy on top of a half-Heusler alloy. The most-stable ideal abrupt interfaces between CMS/spacer and spacer/GaAs were found from DFT relaxation calculations by exhausting all combinations of atomic arrangements, when the in-plane lattice constant of the supercell is fixed to the experimental lattice of GaAs. Based on the results from these calculations,

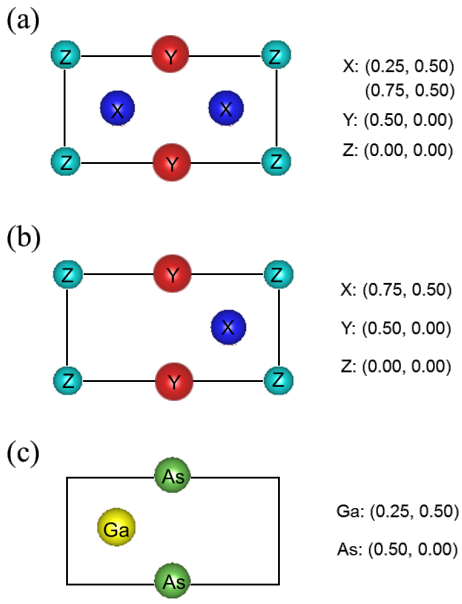

Figure 5.1: Cross-sectional view of a (110) supercell with planar atomic arrangement in (a) a full-Heusler with X_2YZ chemical formula and an $L2_1$ crystal structure, (b) a half-Heusler with XYZ chemical formula and $C1_b$ crystal structure, and (c) GaAs with zinc-blende crystal structure.

a periodic supercell of the form CMS/spacer/GaAs(110) is modeled to investigate the electronic and magnetic properties.

The superlattices are tetragonal unit cells with rectangular bases and the in-plane lattice parameter of the cell is set to the experimental lattice constant of GaAs, such that $a = a_{exp}$ and $b = a_{exp}/\sqrt{2}$, where $a_{exp} = 5.65\,\mathring{A}$, while the height of the supercell is optimized. The periodic supercell has 5 layers of GaAs, 5 layers of GaAs, and n layers of the semiconductor ($n = 2, 3, 4$), with identical interface at both sides of the 2 junctions. A large cut-off energy of 320 eV was chosen for the plane wave basis set. The integration in the irreducible wedge of the supercell Brillouin zone was performed using a (10, 7, 1) k-point mesh according to the Monkhorst–Pack scheme [96], resulting in 24-k-points in the irreducible zone. An energy change of 1×10^{-6} eV was used as the stopping criterion for structural optimization, to reduce forces between ions in all degrees of freedom to less than 0.01 eV/Å. For integration cut-off at the Fermi energy, the Methfessel–Paxton method with smearing width of 0.2 eV was used.

For anisotropy calculations, volume relaxation of the supercell is performed to reduce the forces between the ions to 0.0001 eV/Å. A very high cut-off energy of 539.75 eV

was chosen for the plane wave basis set. The integration in the irreducible wedge of the supercell Brillouin zone was performed using a (10, 7, 1) k-point mesh according to the Monkhorst–Pack scheme [96], resulting in 176-k-points in the irreducible zone.

5.3 Results

Figure 5.2 shows the ball-and-stick representation of a DFT-relaxed metastable structure of CMS/CoTiAs/GaAs(110) heterojunction with 2 layers of CoTiAs spacer layer. At the CoTiAs/GaAs interface of the heterostructure, Ti occupies a bridge site above

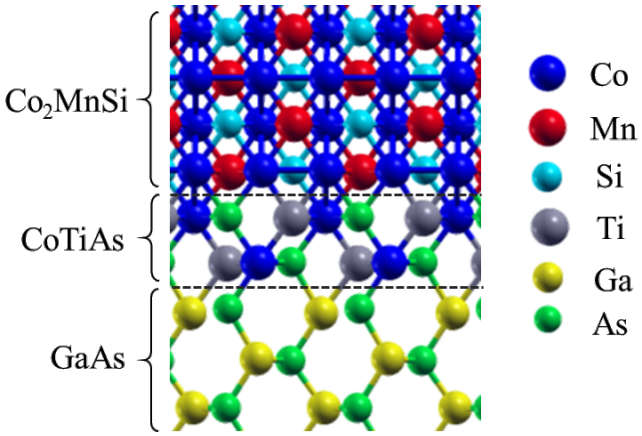

Figure 5.2: Ball-and-stick representation of CMS/CoTiAs/GaAs(110) heterojunction with 2 layers of CoTiAs spacer layer.

As, and CoAs follows the zinc-blende pattern of GaAs. At the interface layer of GaAs, As reconstructs by moving above Ga by 10 pm. At the CMS/CoTiAs interface of the heterostructure, CoTiAs follows the fcc-sublattices of CMS, with Ti occupying a Mn site and As occupying a Si site.

The total spin-resolved DOS of the periodic supercell that models CMS/CoTiAs/-GaAs(110) with 2 layers of CoTiAs is shown in Fig. 5.3. Although a very small density of interface states appears at the Fermi level for the minority spin band, the spin polarization is 0.98 at E_F. There is a wide bandgap like feature that extends away from E_F on both sides. The actual bandgap is 0.12 eV and it is 0.035 eV away from E_F in the valence band region.

To understand the origin of the interface states, the LDOS of component atoms at each interface layer is plotted in Fig. 5.4. Each row represents an interface layer of the

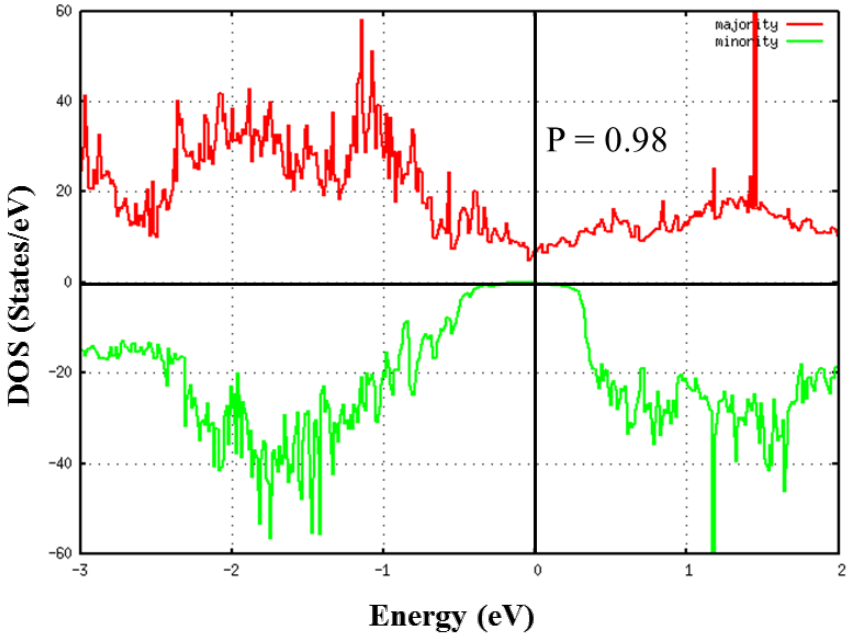

Figure 5.3: Total DOS of CMS/CoTiAs/GaAs(110) model with 2 layers of CoTiAs at each heterojunction.

heterostructure. The spin polarization based on *s,p*-character, relevant for spin transport, is calculated for each atom and is shown in the LDOS plot. Interface states originate at the CoTiAs/GaAs interface. A hybridization between Ti in CoTiAs and Ga (Ti atom's second-nearest neighbor) in GaAs seems to influence the interface states, and influences the DOS of As atoms in both the layers to a lesser extent. Spin polarization, P, of the component atoms demonstrates the origin of the interface states. Again, these interface states will have a very small effect since the overall spin polarization of the system shows a spin polarization of 0.98, and the bandgap features are very promising in this heterostructure.

Table 5.2 lists the component atom magnetic moments in μ_B for ions at the interface. The CMS interface layer is followed by a half-Heusler (XYZ) layer of CoTiAs, with a vacancy in one of the X sites. Due to the loss of a neighbor, one of the Co atoms in CMS loses its moment significantly. There is a slight increase in moments for the other Co atom and Mn atom in the CMS interface layer compared to the moments in bulk CMS. The Si atom at the CMS interface layer has a small moment anti-ferromagnetically coupled with CoMn of CMS. This Si atom occupies a bridge site above Ti (of the CoTiAs

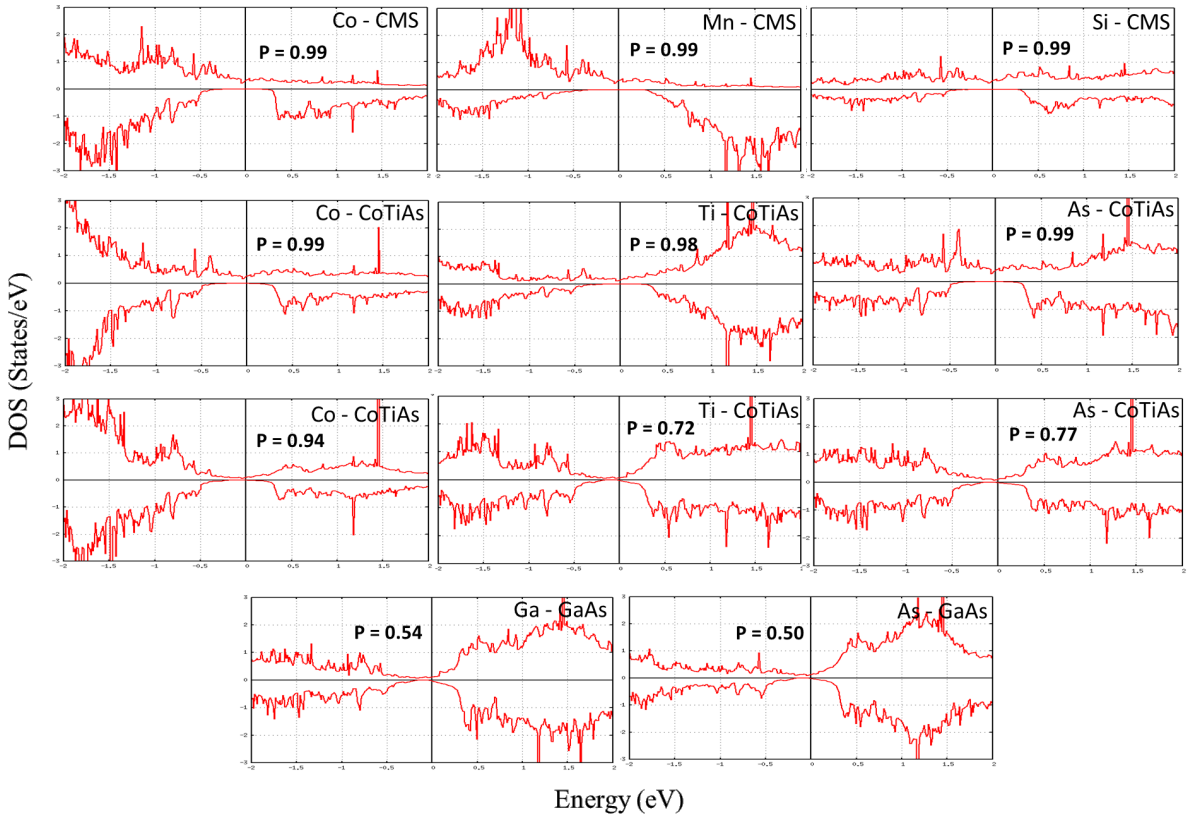

Figure 5.4: Atom-resolved LDOS at the interface for CMS/CoTiAs/GaAs(110) model. Each row represents an interface layer. P is the *s,p*-character spin polarization, calculated for component atoms in the interface. For comparison, LDOS plots of Si, Ga, and As atoms are multiplied by a factor of 10.

Table 5.2: The magnetic moment in μ_B for atoms in the interface in CMS/CoTiAs/-GaAs(110) system.

Alloy	Interface	Magnetic moment (μ_B)			
		Co	Co	Mn	Si
CMS	Int /w CoTiAs	1.058	0.672	3.142	-0.018
		Co	Ti	As	
CoTiAs	Int /w CMS	0.165	-0.087	0.008	
	Int /w GaAs	-0.004	0.012	-0.003	
		Ga	As		
GaAs	Int /w CoTiAs	0.000	-0.001		
		Co	Mn	Si	
Bulk CMS		1.046	2.998	-0.032	

layer), which too has a small negative moment. The Co and As atoms in CoTiAs interface layer facing CMS have small positive moments. There is no significant enhancement in magnetic moment in the next CoTiAs layer facing GaAs or in the GaAs interface layer.

The thickness of the spacer layer, CoTiAs, was increased to 3 and 4 layers to investigate the effects in the electronic and magnetic properties. Figure 5.5 compares the bandgap region of the DOS for CMS/CoTiAs(n)/GaAs(110) for $n = 2, 3, 4$. Increasing

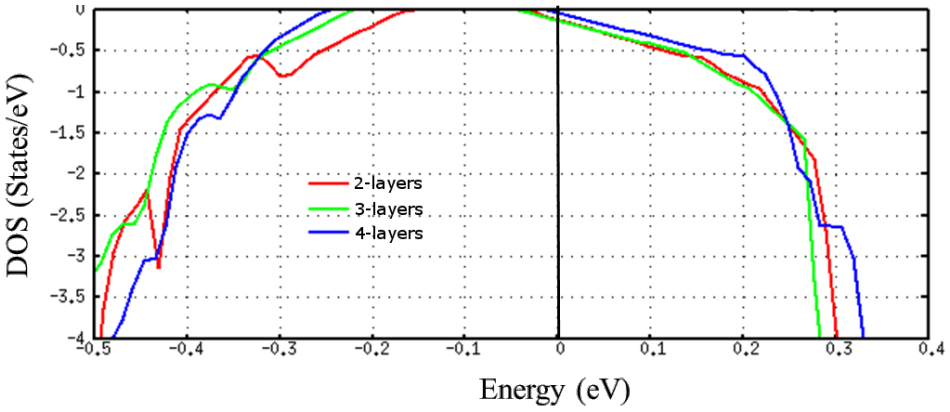

Figure 5.5: Comparison of the minority spin bandgap in the DOS for CMS/CoTiAs(n)/GaAs(110) for $n = 2, 3, 4$.

the number of spacer layers from 2 to 4 increases the bandgap in the minority spin band, and the bandgap gets closer to the Fermi energy, $E_{\rm f}$.

Table 5.3 lists the bandgap properties of CMS/CoTiAs(n)/GaAs(110) for $n = 2, 3, 4$ and CMS/CoTiSb/GaAs(110) for 2 layers of CoTiSb. In CMS/CoTiAs(n)/GaAs(110) system for $n = 2, 3, 4$, the gapwidth and the spin polarization at $E_{\rm f}$ increase as the thickness of the spacer layer increases from 2 to 4. For all the 3 systems, the bandgap is away from $E_{\rm f}$, but as thickness of the spacer layer increases, the edge of the bandgap gets closer to $E_{\rm f}$. In CMS/CoTiSb(2)/GaAs(110) system, the gapwidth is $\sim 50\%$ larger than that for CoTiAs(n) spacer layer system, but the band edge is farther. Also, the spin polarization at $E_{\rm f}$ is 0.9 for the CoTiSb(2) system, compared to 0.97 for the CoTiAs(2) system.

In general, half-metal full-Heusler alloys such as Co_2MnSi have a cubic lattice. When layered with MgO, however, it was found that the lattice could have a tetragonal distortion, which could induce magnetic anisotropy in the Heusler alloy [46]. Moreover, in (110)

Table 5.3: Bandgap properties of CMS/CoTiAs(n)/GaAs(110) for $n = 2, 3, 4$ and for CMS/CoTiSb/GaAs(110) with 2 spacer layers. P is the spin polarization at E_{f}, gapwidth in eV, distance in eV is the distance from the nearest band edge to E_{f}, location of E_{f}, and HM - whether the system is half-metallic. NHM - near half-metallic.

Spacer	# spacer layers, n	P	Gap width (eV)	Distance (eV)	Where is E_{f}?	HM?
	2	0.97	0.12	0.035	@CB	NHM
$CoTiAs_n$	3	0.99	0.19	0.007	@CB	Yes
	4	0.99	0.236	0.010	@CB	Yes
$CoTiSb_n$	2	0.9	0.169	0.1	@CB	NHM

layering direction, the atomic arrangement is different for in-plane and perpendicular directions. Certain Heusler alloy superlattices were found to have perpendicular magnetic anisotropy (PMA) in (110) layering direction (Ref. [119]). To check if insertion of half-Heusler semiconductors between CMS/GaAs(110) systems induced PMA, we calculated the magnetocrystaline anisotropy energy, E_{MCA}, and magnetic anisotropy constant K for these systems, as follows: The magnetocrystalline anisotropy energy, $\Delta E_{\mathrm{MCA}} = E_{\perp} - E_{\parallel}$, where $E_{\perp}$ and $E_{\parallel}$ are the energies of the system, when non-collinear spins of the system is quantized perpendicular and parallel to the interface plane, respectively.

The magnetic anisotropy constant,

$$\perp K = \frac{\Delta E_{\mathrm{MCA}}}{V_{\mathrm{CMS}}},$$

where V_{CMS} is the volume of CMS region in the supercell.

To check if the anisotropy is robust enough to overcome the demagnetization field ($4\pi M_{\mathrm{s}}$) of a thin film, , we calculate $H_K - 4\pi M_{\mathrm{s}}$, where $H_K = \frac{2K}{M_{\mathrm{s}}}$ is the anisotropy field.

Table 5.4 lists the parameters for crystal structure distortion and anisotropy in CMS-/CoTiAs(n)/GaAs(110) for $n = 2, 3$ and for CMS/CoTiSb(2)/GaAs(110). For calculation of anisotropy, the supercell lattice and volume were relaxed. The lattice constant a_r is the relaxed in-plane lattice constant and c_r is the average spacing between the 5 CMS layers in the supercell. A value of c_r/a_r far from 1 denotes the distortion of the full-Heusler alloy CMS into a tetragonal system. In the 2 cases for CoTiAs, listed in Table

Table 5.4: Summary of geometric and magnetic properties of CMS/CoTiAs(n)/GaAs (110) for $n = 2, 3$ and of CMS/CoTiSb(2)/GaAs(110). Number in the bracket in spacer column denotes the number of spacer layers. HM - half metallic.

Spacer	Relaxed a_r (Å)	Relaxed c_r/a_r	$\perp K \times 10^6$ (erg/cm^3)	$[H_K - 4\pi M_s]$ $\times 10^3$ (Oe)	HM?
CoTiAs(2)	5.6351	1.007	1.873	-110.8	Yes
CoTiAs(3)	5.6318	1.01	3.508	-78.5	Yes
CoTiSb(2)	5.7761	0.99	0.092	-157.4	NHM
No spacer	5.6647	0. 99	0.79	-159.6	Yes

5.4, the in-plane lattice constant has not distorted far from the CMS lattice constant of 5.65 Å, but in the case of CoTiSb(2), the lattice distortion from the experimental CMS lattice is 2.23%. As a test case, the most-stable CMS/GaAs(110) system with no spacers in between has been computed and the anisotropy and lattice parameters for this case is listed at the bottom of Table 5.4. A positive value of $\perp K$ signifies PMA for the half-metal Heusler (CMS). In the case of CoTiAs as the spacer, increasing the spacer layer thickness increases the strength of perpendicular magnetic anisotropy. Comparing these anisotropy values with the test case of CMS/GaAs(110) with no spacer, insertion of the CoTiAs spacer has very slightly increased the lattice distortion perpendicular to the interface plane and has significantly improved the PMA, with the addition of each layer of CoTiAs spacer. However, in both cases of CoTiAs ($n = 2, 3$), anisotropy field is not strong enough to overcome the demagnetization field, as given by negative values for $H_K - 4\pi M_s$. But if the strength of the perpendicular magnetic anisotropy continues to increase with increasing thickness, then PMA value will be useful for device applications. It should be noted that the bandgap of CMS/CoTiAs(n)/GaAs(110) system increases with increasing spacer layer thickness, as noted in Table 5.3.

5.4 Conclusions

We investigated, using first principle calculations, the structural, electronic, and magnetic properties of CMS/spacer/GaAs(110) with CoTiAs and CoTiSb as spacer layers.

Our results have shown that the most stable CMS/CoTiAs(n)/GaAs(110) systems are near half-metallic and possess perpendicular magnetic anisotropy. The bandgap and anisotropic characteristics improve with increasing thickness of the CoTiAs spacer layer, transitioning from near half-metallic to half-metallic with 4 layers of CoTiAs. The strength of the perpendicular anisotropy also improves significantly with increasing thickness, suggesting to be a strong contender for PMA-based devices. Also, we propose that the insertion of half-Heusler semiconductors as spacer could be a solution to avoid diffusion of magnetic impurities into GaAs channel.

CHAPTER 6

SUMMARY AND CONCLUSIONS

To date, the field of metallic spintronics has been successful in advancing information technology with devices such as hard disk read heads, based on GMR and TMR, and magnetic random access memory (MRAM). However the advancement of semiconductor-based spintronics is essential in addressing the requirements of the near future. One of the fundamental challenges in semiconductor-based spintronics is the successful integration of half-metal electrodes and spin channels in a way that creates a path for efficient injection of highly spin-polarized current into the channel material. Fundamental understanding of the various physical properties at the interface between spin electrodes and channel is essential in designing efficient spintronic systems. With huge advancements in computing power, first principles-based computational techniques can be utilized to great effect in modeling and investigating complex spintronic structures.

The work presented in this dissertation focuses on two major aspects. First, to utilize experimental data to the full possible extent to model real-world spintronic systems to study, from first principles calculations, the physical properties of such systems. Second, to proceed in the reverse direction to propose efficient spin-based electrode/SC systems, from first principles, as promising candidates.

In Chapter 3, I utilize extensive experimental information of actual Co_2MnSi/GaAs heterostructures, such as STEM micrographs, EELS spectral mapping, and non-local spin valve measurements to predictively model the system as accurately as possible. Using *ab initio* density functional theory calculations, I investigate the physical, chemical, electronic, and magnetic properties to understand the complexity of these structures and the utility of such real-world-based models as spintronic devices.

In Chapter 4, I describe a survey of alternative half-metal sources from the half-Heusler family, from the recently published exhaustive Heusler database. I chose 6 suitable half-Heuslers to model ideal abrupt interfaces with GaAs(110), and perform DFT calculations. I found 3 half-Heusler alloys (CoVAs, NiMnAs, and RhFeGe), which when interfaced with GaAs(110), that preserve the half-metallicity at the interface.

Finally in Chapter 5, I propose, based on first principles, half-Heusler semiconductors as spacers between CMS/GaAs systems in (110) layering. Based on DFT calculations, I show that CoTiAs is a promising spacer which could enhance the perpendicular magnetic anisotropy (PMA) in CMS, while preserving the important half-metallic character at the heterojunctions between CMS/CoTiAs/GaAs(110). This spacer could also serve to prevent in-diffusion of magnetic impurities into the channel material.

REFERENCES

[1] G. Moore, Progress in digital integrated electronics, in *Electron Devices Meeting, 1975 International*, volume 21, pages 11–13, 1975.

[2] S. Lloyd, Ultimate Physical Limits to Computation, Nature **406**(6799), 1047–1054 (2000).

[3] D. D. Awschalom, R. E. Buhrman, J. E. Daughton, S. von Molner, and M. L. Roukes, *Spin Electronics*, Kluwer Academic Publishers, Dordrecht Boston, 2004.

[4] S. Bandyopadhyay and M. Cahay, *Introduction to Spintronics*, CRC Press, 2008.

[5] N. F. Mott, The Electrical Conductivity of Transition Metals, Proc. Roy. Soc. Lond. A: Math. Phys. Engg. Sci. **153**(880), 699–717 (1936).

[6] N. F. Mott, The Resistance and Thermoelectric Properties of the Transition Metals, Proc. Roy. Soc. Lond. A: Math. Phys. Engg. Sci. **156**(888), 368–382 (1936).

[7] M. Jullière, Tunneling between ferromagnetic films, Phys. Lett. A **54**(3), 225–226 (1975).

[8] I. Žutić, J. Fabian, and S. D. Sarma, Proposal for a spin-polarized solar battery, Appl. Phys. Lett. **79**(10), 1558 (2001).

[9] M. N. Baibich, J. M. Broto, A. Fert, F. N. Van Dau, F. Petroff, P. Etienne, G. Creuzet, A. Friederich, and J. Chazelas, Giant Magnetoresistance of (001)Fe/(001)Cr Magnetic Superlattices, Phys. Rev. Lett. **61**, 2472–2475 (1988).

[10] G. Binasch, P. Grünberg, F. Saurenbach, and W. Zinn, Enhanced magnetoresistance in layered magnetic structures with antiferromagnetic interlayer exchange, Phys. Rev. B **39**, 4828–4830 (1989).

[11] S. Datta and B. Das, Electronic analog of the electro-optic modulator, Appl. Phys. Lett. **56**(1990), 665–667 (1990).

[12] H. Ohno, A. Shen, F. Matsukura, A. Oiwa, A. Endo, S. Katsumoto, and Y. Iye, (Ga,Mn)As: A new diluted magnetic semiconductor based on GaAs, Appl. Phys. Lett. **69**(3) (1996).

[13] D. D. Awschalom and J. M. Kikkawa, Nature **397**(6715), 139–141 (1999).

[14] I. Žutić, J. Fabian, and S. D. Sarma, Spintronics: Fundamentals and applications, Rev. Mod. Phys. **76**(April), 323–410 (2004).

[15] J. kerman, Toward a Universal Memory, Science **308**(5721), 508–510 (2005).

[16] D. J. Griffiths, *Introduction to Quantum Mechanics*, Pearson Education, 2009, p. 190.

[17] S. Bandyopadhyay and M. Cahay, *Introduction to Spintronics*, CRC Press, 2008, p. 280.

[18] W. E. Pickett and J. S. Moodera, Half metallic magnets, Phys. Today **54**(5) (2001).

[19] J. D. Jackson, *Classical Electrodynamics Third Edition*, Wiley, 1998.

[20] J. Fabian and S. D. Sarma, Spin relaxation of conduction electrons, J. Vac. Sci. Technol. B: Microelectron. Nanom. Struct. **17**(4), 1708 (1999).

[21] P. R. Hammar, B. R. Bennett, M. J. Yang, and M. Johnson, Observation of Spin Injection at a Ferromagnet-Semiconductor Interface, Phys. Rev. Lett. **83**, 203–206 (1999).

[22] F. Monzon and M. Roukes, Spin injection and the local Hall effect in InAs quantum wells, J. Magn. Mag. Mater. **198 - 199**, 632 – 635 (1999).

[23] H. J. Zhu, M. Ramsteiner, H. Kostial, M. Wassermeier, H.-P. Schönherr, and K. H. Ploog, Room-Temperature Spin Injection from Fe into GaAs, Phys. Rev. Lett. **87**, 016601 (2001).

[24] G. Schmidt, D. Ferrand, L. W. Molenkamp, A. T. Filip, and B. J. van Wees, Fundamental obstacle for electrical spin injection from a ferromagnetic metal into a diffusive semiconductor, Phys. Rev. B **62**, R4790–R4793 (2000).

[25] E. I. Rashba, Theory of electrical spin injection: Tunnel contacts as a solution of the conductivity mismatch problem, Phys. Rev. B **62**, R16267–R16270 (2000).

[26] S. Bandyopadhyay and M. Cahay, *Introduction to Spintronics*, CRC Press, 2008, p. 362.

[27] A. T. Hanbicki, B. T. Jonker, G. Itskos, G. Kioseoglou, and A. Petrou, Efficient electrical spin injection from a magnetic metal/tunnel barrier contact into a semiconductor, Appl. Phys. Lett. **80**, 1240 (2002).

[28] J. Strand, B. D. Schultz, A. F. Isakovic, C. J. Palmstrøm, and P. A. Crowell, Dynamic Nuclear Polarization by Electrical Spin Injection in Ferromagnet-Semiconductor Heterostructures, Phys. Rev. Lett. **91**, 036602 (2003).

[29] D. D. Awschalom, Y. Ohno, D. K. Young, B. Beschoten, F. Matsukura, and H. Ohno, Nature **402**(6763), 790–792 (1999).

[30] G. Salis, R. Wang, X. Jiang, R. M. Shelby, S. S. P. Parkin, S. R. Bank, and J. S. Harris, Temperature independence of the spin-injection efficiency of a MgO-based tunnel spin injector, Appl. Phys. Lett. **87**(26), – (2005).

[31] X. Y. Dong, C. Adelmann, J. Q. Xie, C. J. Palmstrøm, X. Lou, J. Strand, P. A. Crowell, J.-P. Barnes, and A. K. Petford-Long, Spin injection from the Heusler alloy Co[sub 2]MnGe into Al[sub 0.1]Ga[sub 0.9]AsGaAs heterostructures, Appl. Phys. Lett. **86**(10), 102107 (2005).

[32] M. Ramsteiner, O. Brandt, T. Flissikowski, H. T. Grahn, M. Hashimoto, J. Herfort, and H. Kostial, Co_2FeSi/GaAs/(Al, Ga)As spin light-emitting diodes: Competition between spin injection and ultrafast spin alignment, Phys. Rev. B **78**, 121303 (2008).

[33] C. D. Damsgaard, M. C. Hickey, S. N. Holmes, R. Feidenhans'l, S. O. Mariager, C. S. Jacobsen, and J. B. Hansen, Interfacial, electrical, and spin-injection properties of epitaxial Co2MnGa grown on GaAs(100), J. Appl. Phys. **105**(12) (2009).

[34] K. Kasahara, Y. Baba, K. Yamane, Y. Ando, S. Yamada, Y. Hoshi, K. Sawano, M. Miyao, and K. Hamaya, Spin accumulation created electrically in an n-type germanium channel using Schottky tunnel contacts, J. Appl. Phys. **111**(7) (2012).

[35] M. Pénicaud, B. Siberchicot, C. Sommers, and J. Kübler, Calculated electronic band structure and magnetic moments of ferrites, J. Magn. Mag. Mater. **103**(12), 212 – 220 (1992).

[36] S. M. Watts, S. Wirth, S. von Molnár, A. Barry, and J. M. D. Coey, Evidence for two-band magnetotransport in half-metallic chromium dioxide, Phys. Rev. B **61**, 9621–9628 (2000).

[37] H. Akinaga and et. al., J. Mag. Soc. Jpn. **22** (2000).

[38] H. Akinaga, T. Manago, and M. Shirai, Jpn. J. Appl. Phys. **Part 2-Letters 39**, L1118 (2000).

[39] C. P. Bean and D. S. Rodbell, Magnetic Disorder as a First-Order Phase Transformation, Phys. Rev. **126**, 104–115 (1962).

[40] J. Zhao, F. Matsukara, K. Takamura, E. Abe, D. Chiba, and H. Ohno, Room-temperature ferromagnetism in zincblende CrSb grown by molecular-beam epitaxy, Appl. Phys. Lett. **79**, 2776 (2001).

[41] R. A. de Groot, F. M. Mueller, P. G. v. Engen, and K. H. J. Buschow, New Class of Materials: Half-Metallic Ferromagnets, Phys. Rev. Lett. **50**, 2024–2027 (1983).

[42] S. Ishida, T. Masaki, S. Fujii, and S. Asano, Theoretical search for half-metalliic films of Co2MnZ (Z = Si, Ge), Physica B: Cond. Matt. **245**(1), 1 – 8 (1998).

[43] I. Galanakis and P. Dederichs, editors, *Half-metallic Alloys*, Springer Berlin Heidelberg, 2005.

[44] J. Romero, K. Munira, L. Wilson, C. Lample, J. Ma, T. Lovorn, S. Keshavarz, A. Ghosh, and W. H. Butler, Heusler Database. Online: http://heusleralloys.mint.ua.edu/.

[45] I. Galanakis, P. Mavropoulos, and P. H. Dederichs, Electronic structure and Slater-Pauling behaviour in half-metallic Heusler alloys calculated from first principles, J. Phys. D: Appl. Phys. **39**(5), 765 (2006).

[46] K. Munira, J. Romero, and W. H. Butler, Achieving perpendicular anisotropy in half-metallic Heusler alloys for spin device applications, J. Appl. Phys. **115**, 17B731 (2014).

[47] J. Kübler, First principle theory of metallic magnetism, Physica B+C **127**(13), 257 – 263 (1984), Proceedings of the 4th General Conference of the Condensed Matter Division of the {EPS}.

[48] S. Wurmehl, G. H. Fecher, H. C. Kandpal, V. Ksenofontov, C. Felser, H.-J. Lin, and J. Morais, Geometric, electronic, and magnetic structure of Co_2FeSi: Curie temperature and magnetic moment measurements and calculations, Phys. Rev. B **72**, 184434 (2005).

[49] M. Belmeguenai, H. Tuzcuoglu, M. S. Gabor, T. Petrisor, C. Tiusan, F. Zighem, S. M. Chrif, and P. Moch, Co2FeAl Heusler thin films grown on Si and MgO substrates: Annealing temperature effect, J. Appl. Phys. **115**(4) (2014).

[50] P. J. Webster and K. R. A. Ziebeck, *Magnetic Properties of Metals: Alloys and Compounds of d-Elements with Main Group Elements. Part 2*, Springer-Verlag, 1988.

[51] R. Y. Umetsu, K. Kobayashi, A. Fujita, R. Kainuma, and K. Ishida, Magnetic properties and stability of L21 and B2 phases in the Co2MnAl Heusler alloy, J. Appl. Phys. **103**(7) (2008).

[52] Y. Sakuraba, M. Hattori, M. Oogane, H. Kubota, Y. Ando, H. Kato, A. Sakuma, and T. Miyazaki, Giant tunneling magnetoresistance in Co2MnSi/Al-O/Co2MnSi magnetic tunnel junctions, Appl. Phys. Lett. **88**, 192508 (2006).

[53] I. Galanakis, Orbital magnetism in the half-metallic Heusler alloys, Phys. Rev. B **71**, 012413 (2005).

[54] S. Picozzi, A. Continenza, and A. J. Freeman, Co_2MnX (X = Si, Ge, Sn) Heusler compounds: An *ab initio* study of their structural, electronic, and magnetic properties at zero and elevated pressure, Phys. Rev. B **66**, 094421 (2002).

[55] C. Weisbuch and B. Vinter, *Quantum Semiconductor Structures*, Academic Press, Inc., Boston, 1991.

[56] E. Şaşioglu, I. Galanakis, L. M. Sandratskii, and P. Bruno, Stability of ferromagnetism in the half-metallic pnictides and similar compounds: a first-principles study, J. Phys.: Cond. Matt. **17**(25), 3915 (2005).

[57] J. S. Sandhu, A. P. Heberle, J. J. Baumberg, and J. R. A. Cleaver, Gateable Suppression of Spin Relaxation in Semiconductors, Phys. Rev. Lett. **86**, 2150–2153 (2001).

[58] P. Crowell and S. Crooker, Spin Transport in Ferromagnet/III–V Semiconductor Heterostructures, in *Handbook of Spin Transport and Magnetism*, pages 463–485, Informa UK Limited, 2011.

[59] M. D'yakonov and V. Perel', Spin relaxation of conduction electrons in noncentrosymmetric semiconductors, Soviet Physics Solid State, Ussr **13**(12), 3023–3026 (1972).

[60] A. G. Mal'shukov and K. A. Chao, Waveguide diffusion modes and slowdown of D'yakonov-Perel' spin relaxation in narrow two-dimensional semiconductor channels, Phys. Rev. B **61**, R2413–R2416 (2000).

[61] S. Pramanik, S. Bandyopadhyay, and M. Cahay, Decay of spin-polarized hot carrier current in a quasi-one-dimensional spin-valve structure, Appl. Phys. Lett. **84**(2) (2004).

[62] A. W. Holleitner, V. Sih, R. C. Myers, A. C. Gossard, and D. D. Awschalom, Suppression of Spin Relaxation in Submicron InGaAs Wires, Phys. Rev. Lett. **97**, 036805 (2006).

[63] Y. Ohno, R. Terauchi, T. Adachi, F. Matsukura, and H. Ohno, Spin Relaxation in GaAs(110) Quantum Wells, Phys. Rev. Lett. **83**, 4196–4199 (1999).

[64] G. Kresse, Efficient iterative schemes for ab initio total-energy calculations using a plane-wave basis set, Phys. Rev. B **54**(16), 11169–11186 (1996).

[65] G. Kresse, From ultrasoft pseudopotentials to the projector augmented-wave method, Phys. Rev. B **59**(3), 1758–1775 (1999).

[66] W. Kohn and L. J. Sham, Self-Consistent Equations Including Exchange and Correlation Effects, Phys. Rev. **140**, A1133–A1138 (1965).

[67] P. Hohenberg and W. Kohn, Inhomogeneous Electron Gas, Phys. Rev. **136**, B864–B871 (1964).

[68] F. Bloch, Bemerkung zur Elektronentheorie des Ferromagnetismus und der elektrischen Leitfähigkeit, Zeitschrift für Physik **57**(7), 545–555.

[69] P. A. M. Dirac, Note on Exchange Phenomena in the Thomas Atom, Math. Proc. Camb. Phil. Soc. **26**(03), 376 (1930).

[70] P. E. Blöchl, Projector augmented-wave method, Phys. Rev. B **50**(24), 17953–17979 (1994).

[71] J. P. Perdew, K. Burke, and M. Ernzerhof, Generalized Gradient Approximation Made Simple- ERRATA, Phys. Rev. Lett. **77**(1992), 3865–3868 (1996).

[72] J. E. Saal, S. Kirklin, M. Aykol, B. Meredig, and C. Wolverton, Materials Design and Discovery with High-Throughput Density Functional Theory: The Open Quantum Materials Database (OQMD), JOM **65**(11), 1501–1509 (2013).

[73] J. Schmalhorst, S. Kämmerer, M. Sacher, G. Reiss, A. Hütten, and A. Scholl, Interface structure and magnetism of magnetic tunnel junctions with a Co_2MnSi electrode, Phys. Rev. B **70**, 024426 (2004).

[74] S. Picozzi, A. Continenza, and A. J. Freeman, Role of structural defects on the half-metallic character of Co_2MnGe and Co_2MnSi Heusler alloys, Phys. Rev. B **69**, 094423 (2004).

[75] I. Galanakis, P. H. Dederichs, and N. Papanikolaou, Slater-Pauling behavior and origin of the half-metallicity of the full-Heusler alloys, Phys. Rev. B **66**, 174429 (2002).

[76] N. Ghaderi, S. J. Hashemifar, H. Akbarzadeh, and M. Peressi, First principle study of Co2MnSi/GaAs(001) heterostructures, J. Appl. Phys. **102**(2007), 074306 (2007).

[77] S. Hashemifar, P. Kratzer, and M. Scheffler, Preserving the Half-Metallicity at the Heusler Alloy Co2MnSi(001) Surface: A Density Functional Theory Study, Phys. Rev. Lett. **94**(March), 1–4 (2005).

[78] B. Jenichen, J. Herfort, T. Hentschel, A. Nikulin, X. Kong, A. Trampert, and I. Žižak, Residual disorder and diffusion in thin Heusler alloy films, Phys. Rev. B **86**, 075319 (2012).

[79] W. Wang, M. Przybylski, W. Kuch, L. Chelaru, J. Wang, Y. Lu, J. Barthel, H. Meyerheim, and J. Kirschner, Magnetic properties and spin polarization of Co2MnSi Heusler alloy thin films epitaxially grown on GaAs(001), Phys. Rev. B **71**(14), 144416 (2005).

[80] K. Özdoğan and I. Galanakis, Effect of order on the half-metallic gap in Heusler compounds, J. Appl. Phys. **110**(7) (2011).

[81] Y. Miura, K. Nagao, and M. Shirai, Atomic disorder effects on half-metallicity of the full-Heusler alloys $Co_2(Cr_{1-x}Fe_x)Al$: A first-principles study, Phys. Rev. B **69**, 144413 (2004).

[82] S. Picozzi and A. J. Freeman, Polarization reduction in half-metallic Heusler alloys: the effect of point defects and interfaces with semiconductors., J. Phys.: Cond. Matt. **19**(31), 315215 (2007).

[83] J. M. LeBeau, Q. O. Hu, C. J. Palmstrø m, and S. Stemmer, Atomic structure of postgrowth annealed epitaxial Fe/(001)GaAs interfaces, Appl. Phys. Lett. **93**(001), 12–15 (2008).

[84] K. Ludge, B. D. Schultz, P. Vogt, M. M. R. Evans, W. Braun, C. J. Palmstrøm, W. Richter, and N. Esser, Structure and interface composition of Co layers grown on As-rich GaAs(001) c(4×4) surfaces, J. Vac. Sci. Technol. B: Microelectron. Nanom. Struct. **20**(4), 1591 (2002).

[85] H. H. Farrell, J. L. Hilton, B. D. Schultz, and C. J. Palmstrom, Nonequilibrium phases in epitaxial MnGaAs interfacial reactions, J. Vac. Sci. Technol. B: Microelectron. Nanom. Struct. **24**(4), 2018 (2006).

[86] P. Mahadevan and A. Zunger, Ferromagnetism in Mn-doped GaAs due to substitutional-interstitial complexes, Phys. Rev. B **68**(7), 075202 (2003).

[87] A. Z. Alzahrani, G. P. Srivastava, R. Garg, and M. A. Migliorato, An ab initio study of electronic and structural properties of Mn in a GaAs environment., J. Phys.: Cond. Matt. **21**(48), 485504 (2009).

[88] D. Kitchen, A. Richardella, J.-M. Tang, M. E. Flatté, and A. Yazdani, Atom-by-atom substitution of Mn in GaAs and visualization of their hole-mediated interactions., Nature **442**(7101), 436–9 (2006).

[89] Y. L. Soo, G. Kioseoglou, S. Kim, X. Chen, H. Luo, Y. H. Kao, H.-J. Lin, H. H. Hsieh, T. Y. Hou, C. T. Chen, Y. Sasaki, X. Liu, and J. K. Furdyna, Local environment surrounding ferromagnetically ordered Mn in Mn/GaAs digital alloys and (Mn, Ga)As random alloys, Phys. Rev. B **67**, 214401 (2003).

[90] A. Ohtake, A. Hagiwara, and J. Nakamura, Controlled incorporation of Mn in GaAs: Role of surface reconstructions, Phys. Rev. B **87**(16), 165301 (2013).

[91] S. Zhang, L. Zhang, L. Xu, E. Wang, X. Liu, J.-F. Jia, and Q.-K. Xue, Spin driving reconstructions on the GaAs(001):Mn surface, Phys. Rev. B **69**(12), 121308 (2004).

[92] A. Ohtake, J. Nakamura, S. Tsukamoto, N. Koguchi, and A. Natori, New Structure Model for the GaAs(001)-c(44) Surface, Phys. Rev. Lett. **89**(20), 206102 (2002).

[93] A. Ohtake, J. Nakamura, N. Koguchi, and A. Natori, GaAs dimer structure for the GaAs(0 0 1)-c(44) surface, Surface Science **566568, Part 1**, 58 – 62 (2004), Proceedings of the 22nd European Conference on Surface Science.

[94] A. Ohtake, Surface reconstructions on GaAs(001), Surface Science Reports **63**(7), 295–327 (2008).

[95] E. J. Kirkland, *Advanced Computing in Electron Microscopy*, Springer, 2010.

[96] H. J. Monkhorst and J. D. Pack, Special points for Brillouin-zone integrations, Phys. Rev. B **13**, 5188–5192 (1976).

[97] S. Sugahara and J. Nitta, Spin-transistor electronics: An overview and outlook, Proc. IEEE **98**(12), 2124–2154 (2010).

[98] D. D. Awschalom and M. E. Flatté, Challenges for semiconductor spintronics, Nature Physics **3**, 153–159 (2007).

[99] R. Farshchi and M. Ramsteiner, Spin injection from Heusler alloys into semiconductors: A materials perspective, J. Appl. Phys. **113**(19), – (2013).

[100] S. Picozzi, A. Continenza, and A. J. Freeman, Spin injection at heusler/semiconductor interfaces: First-principles determination of potential discontinuity and half-metallicity, J. Appl. Phys. **94**(2003), 4723–4725 (2003).

[101] S. Picozzi, A. Continenza, and A. J. Freeman, The Co2MnGe Heusler compound: a first principles study of the bulk phase and of the interface with GaAs, IEEE Transactions on Magnetics **38**(5), 2895–2897 (2002).

[102] I. Galanakis, Towards half-metallic interfaces: Co 2 CrAl/InP contacts, J. Phys.: Cond. Matt. **16**(45), 8007 (2004).

[103] I. Galanakis, M. Ležaić, G. Bihlmayer, and S. Blügel, Interface properties of NiMnSbInP and NiMnSbGaAs contacts, Phys. Rev. B **71**, 214431 (2005).

[104] G. A. de Wijs and R. A. de Groot, Towards 100% spin-polarized charge-injection: The half-metallic NiMnSb/CdS interface, Phys. Rev. B **64**, 020402 (2001).

[105] P. Mavropoulos, I. Galanakis, and P. H. Dederichs, Multilayers of zinc-blende half-metals with semiconductors, J. Phys.: Cond. Matt. **16**(24), 4261 (2004).

[106] K. Nagao, Y. Miura, and M. Shirai, Half-metallicity at the (110) interface between a full Heusler alloy and GaAs, Phys. Rev. B **73**(10), 104447 (2006).

[107] C. Kittel, *Introduction to Solid State Physics*, John Wiley & Sons, Inc., New York, 7th edition, 1995, p. 446.

[108] B. Xu and M. Zhang, Effects of structural change on half-metallicity of CoMnZ (Z=P, As, Sb): A first-principle study, Journal of Magnetism and Magnetic Materials **323**(7), 939 – 944 (2011).

[109] V. A. Dinh, K. Sato, and H. Katayama-Yoshida, New High-Tc Half-Heusler Ferromagnets NiMnZ (Z=Si, P, Ge, As), Journal of the Physical Society of Japan **77**(1), 014705 (2008).

[110] T. Kanomata, T. Kawashima, H. Utsugi, T. Goto, H. Hasegawa, and T. Kaneko, Magnetic properties of the intermetallic compounds MMX(M=Cr,Mn, M=Ru,Rh,Pd, and X=P,As), J. Appl. Phys. **69**(8) (1991).

[111] H. C. Koo, J. H. Kwon, J. Eom, J. Chang, S. H. Han, and M. Johnson, Control of Spin Precession in a Spin-Injected Field Effect Transistor, Science **325**(5947), 1515–1518 (2009).

[112] S. Bandyopadhyay and M. Cahay, Electron spin for classical information processing: a brief survey of spin-based logic devices, gates and circuits, Nanotechnology **20**(41), 412001 (2009).

[113] D. Monsma, R. Vlutters, and J. Lodder, Room temperature-operating Spin-Valve Transistor formed by vacuum bonding, Science **281**, 407–409 (1998), Imported from SMI Reference manager.

[114] J. L. Hilton, B. D. Schultz, and C. J. Palmstrom, Growth temperature dependence of MnGaAs surfaces and interfaces, J. Appl. Phys. **102**(6), 063513 (2007).

[115] B. Schultz, N. Marom, D. Naveh, X. Lou, C. Adelmann, J. Strand, P. Crowell, L. Kronik, and C. Palmstrø m, Spin injection across the Fe/GaAs interface: Role of interfacial ordering, Phys. Rev. B **80**(20), 201309 (2009).

[116] D. Orgassa, H. Fujiwara, T. C. Schulthess, and W. H. Butler, First-principles calculation of the effect of atomic disorder on the electronic structure of the half-metallic ferromagnet NiMnSb, Phys. Rev. B **60**, 13237–13240 (1999).

[117] Y. Sakuraba, M. Hattori, M. Oogane, H. Kubota, Y. Ando, A. Sakuma, and T. Miyazaki, Half-metallic band structure observed in Co 2 MnSi-based magnetic tunnel junctions, J. Phys. D: Appl. Phys. **40**(5), 1221 (2007).

[118] S. Kämmerer, A. Thomas, A. Hütten, and G. Reiss, Co2MnSi Heusler alloy as magnetic electrodes in magnetic tunnel junctions, Appl. Phys. Lett. **85**(1), 79–81 (2004).

[119] J. G. Azadani, K. Munira, J. Romero, J. Ma, C. Sivakumar, A. W. Ghosh, and W. H. Butler, Anisotropy in layered half-metallic Heusler alloy superlattices, J. Appl. Phys. **119**(4) (2016).

APPENDIX A

DFT MODELS FOR 0.5ML CMS/GAAS(001)

A.1 Case91 DFT model

In this section, the properties of *ab initio* DFT-based metastable structures for 0.5ML CMS/GaAs(001) (with MnSi-initial flux) that are in relatively good agreement with the experimentally observed interfacial structure are discussed. A DFT model named Case90 was predicted as the best-fit model of the observed interfacial structure, based on its agreement with the observed STEM, the relatively low formation energy (lowest among the number of models that were tried), and a high spin polarization value. I will discuss the results of a few other DFT model structures that agree well with the physical structure of the observed sample. Case91 is a model which is similar to Case90 DFT-model, except the atom composition in Int1 (Mn in Int1 instead of Si). The physical properties of the metastable structure is identical to Case90, but Case91 model has a slightly higher formation energy, E_{form}, compared to Case90. The half-metallic character of bulk-CMS is destroyed completely at the interface in this model (P = 0.05). Figure A.1 shows the ball-and-stick representation of the interface structure in Case91.

The interface in Case91 model has a Mn atom at Int1, which is at the same layer as the 'surface As' (the last layer of the bulk GaAs). The Mn atom fills every vacancy site of the 'surface As' (unlike LeBeau et. al. [83], where Fe fills alternative sites above 'surface As'). Mn atom at Int1 has 'surface As' as its nearest neighbor with a separation of 2 Å. Interface 2 (Int2) is modeled with 0% occupancy in this model. Int3 is occupied by Mn, since Si or Co in this position distorts the structure of the interface very differently from the experimental STEM. Mn atom at interface 3 (Int3) has 'surface As' as its nearest neighbor, separated by a distance of 2.51 Å, and Co (first layer of CMS above

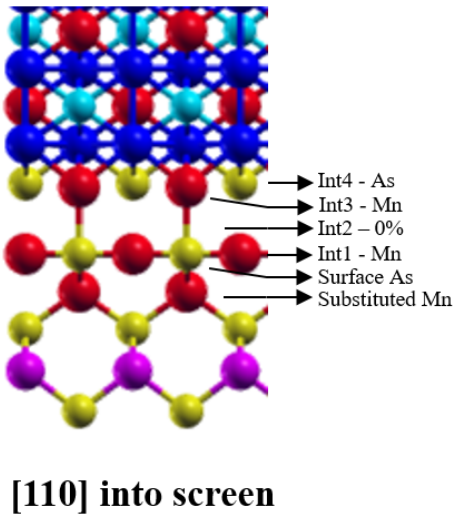

Figure A.1: Ball-and-stick representation of the interface structure in Case91 DFT model as viewed from [110] plane.

the interface) as next nearest neighbor at a distance of 2.58 Å. In the above DFT model, Int4 is completely covered with As, as described in Fig. 3.7(f), and is separated from Co, its nearest neighbor above it, by 2.48 Å. The subsurface Ga is substituted with a Mn atom as labeled in Fig. 3.11. The formation energy per atom calculated for Case91 is -0.100 eV, which is relatively low and has

The spin-resolved total density of states (DOS) of the periodic supercell of Case91 DFT model is shown in Fig. A.2. For comparison, the total DOS of CMS/GaAs(001) with an ideal abrupt SiMn/As termination (shadowed portion of the plot) is added to the DOS plot in Fig. A.2. Unlike in the best-fit DFT model, there a large number of electronic states at the Fermi level for minority spin bands in Case91, thus completely destroying the spin polarization at the interface. The spin polarization value calculated at the Fermi level is $P = 0.05$, which is close to zero.

A.2 Case97 DFT model

Another DFT model that closely resembels the physical structure as observed in the STEM and also has a low formation energy per atom (reported in Table 3.3) is Case97. The physical structure is aidentical to the beft-fit DFT model (Case90) and Case91. The formation energy per atom for this model is -0.055 eV. The differenc in atomic

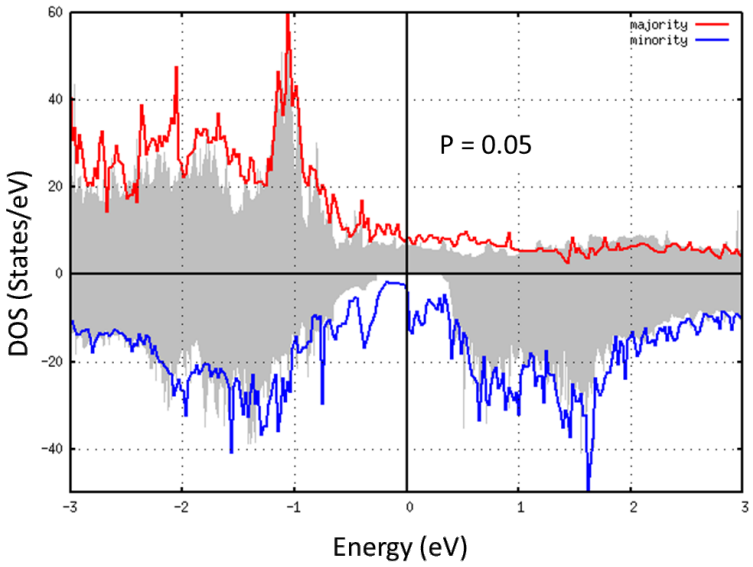

Figure A.2: Total DOS of Case91 DFT model for 0.5ML CMS/GaAs(001) with MnSi-initial flux. The total DOS of a theoretical CMS/GaAs(001) with an ideal abrupt SiMn/As termination is shown by the background grey portion.

composition at the interface for Case97 with Case91 is that there is no Mn substitution for a subsurface Ga (first layer of Ga below the interface). The bond-length of the last layer of As–Ga ('surface As' and 'subsurface Ga') is increased by 4% to 2.57 Åfrom the bond-length value for bulk-like As–Ga. The presence of Mn in Int1 influences this change in bond-length.

The spin-resolved total density of states (DOS) of the periodic supercell of Case97 DFT model is shown in Fig. A.3. For comparison, the total DOS of CMS/GaAs(001) with an ideal abrupt SiMn/As termination (shadowed portion of the plot) is added to the DOS plot in Fig. A.3. There are more number of electronic states at the Fermi level for minority spin bands in Case97, compared to that of the majority spin bands, thus with a high spin polarization value at the interface of P = -0.52.

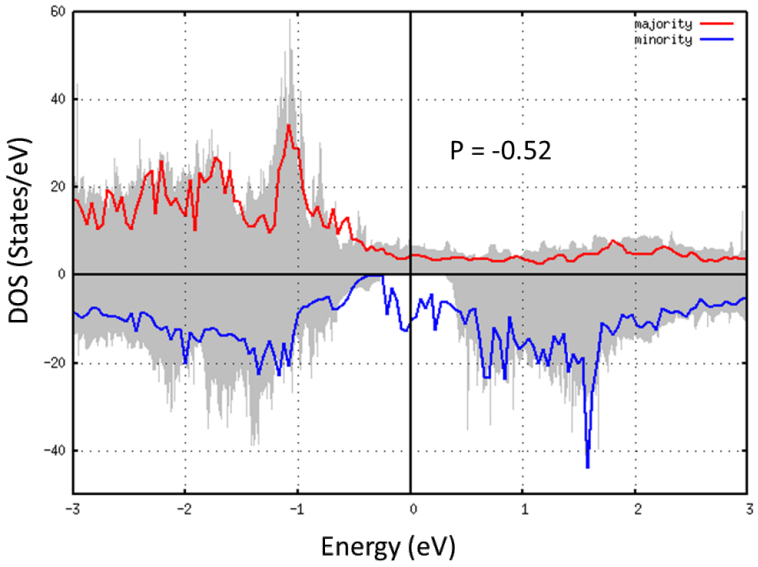

Figure A.3: Total DOS of Case97 DFT model for 0.5ML CMS/GaAs(001) with MnSi-initial flux. The total DOS of a theoretical CMS/GaAs(001) with an ideal abrupt SiMn/As termination is shown by the background grey portion.